

EVALUATING REFERENCE EVAPOTRANSPIRATION AND THE
EFFECTS OF CLIMATE CHANGE AND SOIL PARAMETERIZATION
WITHIN DISTRIBUTED HYDROLOGIC MODELS

Nicoleta Cristea

A dissertation
submitted in partial fulfillment of the
requirements for the degree of

Doctor of Philosophy
University of Washington
2012

Reading Committee:
Stephen J. Burges, Co-Chair
Jessica D. Lundquist, Co-Chair
Alan F. Hamlet

Program Authorized to Offer Degree:
Civil and Environmental Engineering

University of Washington

Abstract

EVALUATING REFERENCE EVAPOTRANSPIRATION AND THE
EFFECTS OF CLIMATE CHANGE AND SOIL PARAMETERIZATION
WITHIN DISTRIBUTED HYDROLOGIC MODELS

Nicoleta Cristea

Chairs of the Supervisory Committee:

Professor Emeritus Stephen J. Burges

Associate Professor Jessica Lundquist

Department of Civil and Environmental Engineering

Parsimonious methods to estimate potential evapotranspiration (ET) based on temperature and solar radiation data are attractive alternatives to more data intensive methods in areas with limited data availability or when developing algorithms for estimating ET from remotely sensed data. In the first part of this dissertation, the performances of the most commonly used ET models have been investigated and methods to improve their performance in a variety of climates have been proposed. In addition, linear models to evaluate potential ET at annual and seasonal time scales have also been developed. These models have a simple structure and are useful for evaluating spatial distribution of ET, assessing historical annual and growing season ET, performing baseline checks, or evaluating ET trends based on output from global climate models.

In the second part of this work, a complex Richards equation based hydrologic model has been used in which soil parameterization was varied. Model simulation results showed that both the soil moisture retention curve and the saturated hydraulic conductivity control the level and spatial variability of soil moisture and affect the shape, timing, and magnitude of the hydrograph. Results from these virtual experiments provide insights for model calibration and for the site locations useful for field data collection to best inform the distributed hydrologic model.

Finally, the last topic investigates hydrologic modeling at a larger scale and in the context of climate change. A fine-scale, distributed hydrologic model, DHSVM, has been used to investigate the role of the vegetation cover density and extent on streamflow timing and magnitude for a high elevation basin located in the Sierra Nevada Mountains, California. Model simulations have indicated that in this area, when temperatures are rising, snow melts faster in the presence of forests mostly due to increases in net longwave radiation. The findings from this study are important to identify forest management actions in the Sierra Nevada that have the potential to increase snow retention at high elevations and increase summer flows.

DEDICATION

To Mom and George for their continuous and enthusiastic support.

ACKNOWLEDGEMENTS

I would like to thank my academic advisor Dr. Stephen Burges for his guidance, thoughtful insights and patience that have helped me navigate through my research endeavors in the field of Hydrology at the University of Washington. Special thanks to my co-chair Dr. Jessica Lundquist who guided me during my final years and helped me build confidence and truly appreciate the power of collaboration and communication. Thank you to Stephanie Kampf for her contributions and friendship and to all my committee members (Dr. Stephen Burges, Dr. Jessica Lundquist, Dr. Stephanie Kampf, Dr. Alan Hamlet, Dr. David Montgomery, and Dr. James Hughes) for providing timely and thoughtful feed-back. Thank you to Drs. Benjamin Mirus and Keith Loague who have contributed to the work on the hypothetical catchment. Thank you to my friends and colleagues in Wilcox 159, to Se-Yeun Lee, Julie Vano, Liz Clark, and Ronda Strauch and to the entire Mountain Hydrology Group. I have learned much through our weekly meetings and conversations. Thank you to Meade Krosby for collaboration and for opening a different perspective for me on research in a complementary field. Finally, thank you to my family, and especially to my mom, Jeny, and my husband, George, for understanding and supporting my academic research interests. The research was funded by U.S. National Science Foundation grants: NSF – EAR-0537410, CBET-0729830, and Grant No. CBET-0729838.

TABLE OF CONTENTS

Chapter 1. Introduction	1
Chapter 2. Revised coefficients for Priestley-Taylor and Makkink-Hansen equations for estimating daily reference evapotranspiration	4
Abstract	4
2.1. Introduction and background	5
2.2. Daily evapotranspiration models	7
2.2.1. FAO 56 Penman-Monteith	7
2.2.2. Priestley-Taylor	8
2.2.3. Makkink-Hansen	8
2.3. Methods	8
2.4. Meteorological datasets	9
2.5. Results	11
2.5.1. Daily ET_0 estimates before and after local calibration	11
2.5.2. Daily evaporative coefficients relationships.....	14
2.6. Maps of evaporative model coefficients	16
2.7. Model tests	17
2.8. Discussion	20
2.9. Summary and Conclusions	22
2.10. References	23
Chapter 3. Linear models for estimating annual and growing season reference evapotranspiration using averages of weather variables	29
3.1. Introduction	30
3.2. Data and methods	31
3.3. Results	34
3.3.1. Multiple regression relationships	34
3.3.2. Test results.....	38
3.3.3. Example application.....	40
3.4. Discussion	42
3.5. Summary and Conclusions	43
3.6. References	44
Chapter 4. Evaluating a distributed hydrologic model at the catchment scale against a hypothetical reality dataset – tests of soil parameterization	52
4.1. Introduction: why use hypothetical reality datasets to evaluate distributed hydrologic models?	53
4.1.1. Challenges related to applying physically-based distributed hydrologic models.....	53
4.1.2. Motivation for introducing a hypothetical reality dataset to support distributed hydrologic model testing at the catchment scale.....	55
4.1.3. Objectives of this study.....	55
4.2. Tarrawarra-like Hypothetical Reality	56
4.3. Distributed model testing and evaluation methods	57

4.3.1. Test model, MODHMS	57
4.3.2. Evaluation objectives and model scenarios.....	58
4.4. Simulation results.....	63
4.4.1. MODHMS Reference case scenario	63
4.4.2. MODHMS A, B, and C scenarios, wet period A.....	64
4.4.3. MODHMS A, B and C scenarios, dry period B.....	67
4.4.4. MODHMS A1, A2, B1, B2, C1, and C2 scenarios, wet period A	70
4.4.5. MODHMS A1, A2, B1, B2, C1, and C2 scenarios, dry period B	73
4.5. Discussion	75
4.5.1. Influence of the soil moisture retention curve and saturated hydraulic conductivity on the near surface hydrologic response	75
4.5.2. Implications for model calibration.....	77
4.6. Summary and conclusions.....	78
4.7. References	79
Chapter 5. Modeling how vegetation cover affects climate change impacts on streamflow timing and magnitude in the upper Tuolumne Basin, Sierra Nevada	88
5.1. Introduction	89
5.2. Study site and data sources	91
5.3. Hydrologic modeling, climate data, and methods for streamflow analysis	93
5.3.1. Hydrologic model description and model set-up	93
5.3.2. Climate data and model scenarios.....	95
5.3.3. Methods to analyze changes in streamflow patterns	98
5.4. Results	99
5.4.1. Model evaluation for the historic period, 2003-2009	99
5.4.2. Simulated changes in streamflow timing and magnitude as a function of vegetation cover in a warming climate	101
5.5. Discussion	110
5.6. Summary and Conclusions	114
5.7. References	116

LIST OF FIGURES

Figure 2.1 Locations and UNEP aridity index of study and test sites displayed on the annual average air temperature US map.	10
Figure 2.2 Ratios r_{PT} of the growing season PT ET_o to FAO-56 PM ET_o (a), and MK-Ha ET_o to FAO-56 PM ET_o (b), as function of annual RH and U . Dots represent station-based calculations of r_{PT} and r_{MK-Ha} , and filled areas are developed from a projected triangle based linear interpolation grid.	12
Figure 2.3 Examples of local calibration of the PT and MK-Ha models for April to October 2006 daily evaporation at Buckeye, AZ (a-d), and Whishek, ND (e-h).	13
Figure 2.4 (a) Ratios of the growing season PT ET_o to FAO-56 PM ET_o and MK-Ha ET_o to FAO-56 PM ET_o before and after local calibration; (b) ranges of the calibrated α and C	14
Figure 2.5 Multiple linear regressions based on mean annual RH and U (a), or VPD and U (b), for the PT, and MK-Ha, ET_o models' evaporative coefficients, α and C	15
Figure 2.6 Linear relationship between the calibrated PT α and MK-Ha C coefficients... 16	16
Figure 2.7 Spatial distributions of annual average RH (a), annual average U_{10} (b), α (c), 17	17
Figure 2.8 Box plots of $RMSE$ (a), d (b), and r (c) at the test stations for the original, station specific, and map derived, α and C coefficients. Dotted lines in (c) identify the 0.95 and 1.05 values.	18
Figure 2.9 Scatterplots of the FAO-56 PM ET_o and PT and MK-Ha ET_o in $mm\ d^{-1}$, estimated with the original coefficients ((a) – (d) and (i) – (l)) and with coefficients estimated based on the RH and U (grey color), and VPD and U (red color) relationships, respectively ((e) – (h), and (m) – (p)) at four test stations. Dotted line is the one-to-one relationship.	20
Figure 3.1. Study and test station locations shown on a map of ET calculated with the Hamon (1961) equation (USGS, 2003).	32
Figure 3.2 Histograms and fitted theoretical normal distributions of residuals in mm (a-l) for models i – xii, which are defined in Table 3.1.	36
Figure 3.3 Correlations of the annual (a-d) and growing season ET_o (e-l) with each individual predictor.	38
Figure 3.4 Box and whisker plots of the ratio r for models i-vi (a), models v – vii (b), and models ix – xii (c) at the test stations. Dotted lines correspond to $r = 0.95$ and $r = 1.05$	39
Figure 3.5 Scatterplots of the calculated FAO-56 PM ET_o and predicted ET_o with models i-vi (a-d), models v – viii (e-h) and models ix – xii (i-l) at the test stations. Dashed line shows the one-to-one relationship.	40
Figure 3.6. Spatial patterns of R_s (a), T (b), RH (c), U (d), annual ET_o from model iii (e), annual ET_o from model iv (f), growing season ET_o from model vii (g), growing season ET_o from model viii (h) and relative differences between ET_o from models iii and iv and the ET_o map of Figure 3.1 (i-j).	41

Figure 4.1 a) Tarrawarra location, Australia and b) example of snapshot of degree of saturation from the HR hydrologic response in the top 2 cm, 12 May 1996, 0:00AM.	56
Figure 4.2 a) Clay loam water retention curves and the approximate curve at Tarrawarra predicted by ROSETTA; b), c), d) soil water retention curves of the three layers used in the MODHMS reference scenario and the clay loam, loamy sand, and silty clay curves used in the MODHMS A, B, and C scenarios.	61
Figure 4.3 a) HR and MODHMS reference case scenario (RCS) hydrographs, b) - i) HR and MODHMS RCS saturation at node 4 and node 11, depths 0.02, 0.1, 0.5 and 1 m during the evaluation period.	64
Figure 4.4 a) HR and A, B, and C MODHMS hydrographs during the wet period A; b) - e) HR and A, B, and C MODHMS saturation at node 4 and node 11, depths 0.02 and 0.1 m; f) spatial distribution of HR and A, B, and C MODHMS saturation in the top 2 cm at 24 h intervals, 8 August 1999, 0:00 AM to 15 August 1999, 0:00 AM.....	66
Figure 4.5 a) HR and A, B, and C MODHMS hydrographs during the dry period; B b) - e) HR and A, B, and C MODHMS saturation at node 4 and node 11, depths 0.02 and 0.1 m; f) spatial distribution of HR and A, B, and C MODHMS saturation in the top 2 cm at 24 h interval, January 21 2000, 0:00 AM to January 29 2000, 0:00 AM.....	69
Figure 4.6 a), f), k) HR and A1, A2, B1, B2, C1, and C2 MODHMS hydrographs during the wet period A; b) - e), g) - j) and l) - o) HR and A1, A2, B1, B2, C1, and C2 MODHMS saturation at node 4 and node 11, depths 0.02 and 0.1 m.	71
Figure 4.7 Spatial distribution of HR and A1, A2, B1, B2, C1 and C2 MODHMS saturation in the top 2 cm at 24 h interval, 8 August 1999, 0:00 AM to 15 August 1999, 0:00 AM during the wet period A.	72
Figure 4.8 a), f), k) HR and A1, A2, B1, B2, C1, and C2 MODHMS hydrographs during the dry period B; b) - e), g) - j) and l) - o) HR and A1, A2, B1, B2, C1, and C2 MODHMS saturation at node 4 and node 11, depths 0.02 and 0.1 m.	74
Figure 4.9 Spatial distribution of HR and A1, A2, B1, B2, C1, and C2 MODHMS saturation in the top 2 cm at 24 h interval, January 21 2000, 0:00 AM to January 29 2000, 0:00 AM during the dry period B.	75
Figure 5.1 Upper Tuolumne basin, Sierra Nevada, California.	92
Figure 5.2 a) Mean annual temperatures and b) total precipitation for the climate simulation period 2001-2100.....	97
Figure 5.3 DHSVM calibration: a) simulated and observed daily hydrographs, b) hydrograph residuals, c) and d) simulated and observed SWE at Dana Meadows and Tuolumne Meadows sites, respectively.	100
Figure 5.4 a) Simulated hydrographs assuming historic and increased air temperatures for uniform forest scenario and for b) barren scenario; c) and d) SWE levels for the same scenarios at Dana Meadows, respectively; e) forest cumulative actual evapotranspiration; f) historic and increased air temperature daily timeseries. Vertical lines identify COM for each hydrograph. All plots are shown for water year 2004. Horizontal (a, c) and vertical (b, d) continuous lines are reference thresholds.	102

Figure 5.5 Monthly simulated energy balance components for the snowpack at Dana Meadows using historic temperatures for a) forested, and for b) barren; monthly energy balance components using a 3°C increase in temperature for c) forest, and for d) barren; monthly differences in energy balance components between the two temperature scenarios for e) forest, and for f) barren..... 103

Figure 5.6 a) Monthly melt rates at Dana Meadows using historic and increased temperature for forest and for barren scenarios, b) difference in monthly melt rates using historic and increased temperature for forest, c) difference in monthly melt rates using historic and increased temperature for barren surface. 105

Figure 5.7 a) Center of mass, COM, for the four vegetation scenarios, b) Sen’s slope of COM change, c) boxplots of the COM series, and d) diagram showing results from the Wilcoxon rank-sum test for the medians between combinations of any two COM series of the four vegetation scenarios: 0 indicates that the null hypothesis that the two COM series are drawn from the same distribution cannot be rejected at the 95% confidence level, and 1 indicates a rejection of the null hypothesis. .. 106

Figure 5.8 a) Twenty-year average monthly hydrographs at the beginning (dotted line) and end (continuous line) of the simulation period for current forest, b) all forest, c) barren and d) thinned forest scenarios, respectively; e) Sen’s slope for monthly fractional flows for the entire 2001-2100 simulation period. 108

Figure 5.9 a) Lowest 7-day average low flow during July-August each year for the four vegetation scenarios, b) duration curves for the July-August 7-day average lowest flows, and c) relative frequencies, as the number of years in each the lowest 7-day average was below a threshold value ($2 \text{ m}^3 \text{ s}^{-1}$) divided by the total number of years. 110

LIST OF FIGURES IN THE APPENDICES

Figure 5.A1. a), c), e), g) Simulated daily hydrographs assuming historic and increased air temperatures for barren scenario and for uniform forest scenario with variable radiation attenuation parameter k ; b), d), f), h) SWE levels for the same scenarios at Dana Meadows and Tuolumne Meadows locations. Vertical lines identify COM for each hydrograph. All plots are shown for water year 2004....131

Figure 5.A2. Google Earth 6.2.image (June 14, 2011) approximately 124.2 km from the Tuolumne Meadows in the Sierra Nevada centered at 38°48’56’’N Lat and 120°06’35’’W Long and 2158 m elevation, showing snow lasting longer in the barren areas than under the forest. Available at <http://www.google.com/earth/index.html> [Accessed June 2012].....132

LIST OF TABLES

Table 2.1 Estimated values of the PT evaporative coefficient α for a range of climates and terrain covers.	5
Table 2.2 Multiple linear regression coefficients $b_{1,2,3}$, 95% CI and r^2	14
Table 3.1 Regression relationships, regression coefficients, 95% confidence intervals, the coefficient of determination (R^2) and SEE at study and test sites. Models i-iv are for annual ET_o , and models v-xii are for the growing season ET_o	35
Table 3.2 Correlation matrices between predictors: I) annual averages of R_s , T , RH and U and II) growing season averages of R_s , T , RH and U	37
Table 4.1 Excerpt from ROSETTA textural class look-up table.	60
Table 4.2 Summary of soil parameterization in all scenarios addressing testing objectives I and II.....	61
Table 4.3 MODHMS efficiency criterion NSE for the 10 MODHMS scenarios during the 1 June 1999-11 November 2000 evaluation period and wet and dry periods A and B.	67
Table 5.1 DHSVM scenarios for ΔT sensitivity tests.....	96
Table 5.2 DHSVM vegetation scenarios for the A2 GFDL climate data.	97

LIST OF TABLES IN THE APPENDICES

Table 2.B1. Test stations and their latitude and longitude, annual average temperature, T , relative humidity, RH , 2-m wind speed, U , solar radiation, R_s , and α and C values estimated with either station mean annual RH and U or with the coefficient maps in Figure 2.7c-d.....	28
Table 3.C1. Regression relationships, regression coefficients, 95% confidence intervals, the coefficient of determination (R^2) and standard error of the estimate (SEE) at study and test sites for the June-July-August (JJA) period.....	51
Table 5.A1. DHSVM parameters used for the upper Tuolumne area, Sierra Nevada.....	128
Table 5.A2. DHSVM scenarios for radiation attenuation sensitivity tests.....	130

Chapter 1. Introduction

This dissertation is concerned with three separate topics: i) reliable means for estimating evapotranspiration when measurements needed to solve the full land surface energy budget are not available (Chapter 2 and 3), ii). The detailed soil-water dynamic behavior of a fine-scale hydrologic model implemented over the 10.5 ha Tarrawarra catchment in Victoria, Australia (Chapter 4), and iii) an assessment of the influence of vegetation cover on the timing and amount of runoff from a high mountain snow dominated catchment in the context of a warming climate (Chapter 5).

Chapters 2-5 are self-contained papers, each with its own abstract, conclusions, and references. Chapter 2 has been published as Cristea et al (2012a). Chapter 3, Cristea et al (2012b) is in press. Chapter 5 has been submitted for publication in *Hydrological Processes*.

Evapotranspiration, the amount of water evaporating from soil and transpired through plants, is a key component of the water budget. Its quantitative evaluation is important for estimating agricultural water needs, quantifying the water balance in the natural environment, assessing climate change effects on water resources, etc. Physically based estimates of actual and potential evapotranspiration (e.g. using the Penman Monteith approach) require observations of solar radiation, temperature, relative humidity and wind speed (Allen et al., 1998). While the extent and quality of observing networks have been greatly improved during the past decade, in many hydrologic applications the observed meteorological variables are unavailable at the desired spatial resolution, or are completely unavailable in remote areas (Dent, 2012). In these cases, as well as in others, such as in remote sensing applications methods to compute evapotranspiration based on fewer variables, typically solar radiation and temperature, are used (e.g. Jiang and Islam 2001; Wang et al. 2006a; Bois et al. 2008). These methods however were developed under specific, local, conditions and their use outside these conditions may be inappropriate.

In Chapter 2 a comparison of two simple radiation based methods to calculate potential evapotranspiration against a more comprehensive approach for a range of climates is presented. This comparison was made to identify the conditions in which the simpler methods diverge from the performance of the more comprehensive method. Equations were developed to correct the empirical coefficients of the simple models. This correction allowed the simpler models to perform much better over a relatively large range of climate conditions.

Chapter 3 covers the evaluation of potential evapotranspiration at large spatial and temporal scales. For this application, linear models based on averages of weather variables at annual and seasonal scales were developed. The linear models constitute an improvement over the other approaches such as those based on temperature and latitude alone. The proposed new models can be used to evaluate spatial distributions of potential evapotranspiration, as well as climate change effects on evapotranspiration, due to projected changes in temperature and relative humidity.

Hydrologic modeling is used to account for the water and energy fluxes and states in hydrologic systems. Hydrologic models often serve as tools to address science or engineering questions. The most sophisticated hydrologic models (e.g. fine-scale spatially distributed, physically based models, integrating surface and subsurface processes), require detailed and accurate observations. However, detailed observations about system states are rarely available, even at the scale of a small catchment. In Chapter 4 an alternative scheme to gain understanding about the hydrology of a small, gently sloping, 10.5 ha catchment is used. This method involves the use of synthetic hydrologic datasets to analyze the hydrologic behavior of the catchment as a function of the soil type. The assemblage of potential evapotranspiration timeseries as part of the input datasets to the models was one of the first steps taken in this analysis. This step prompted the investigation of potentially useful methods to calculate evapotranspiration, which finally led to the results detailed in the first two chapters of this work.

Chapter 5 presents a second hydrologic modeling analysis. In this case, the role of the vegetation cover in the catchment hydrologic behavior is evaluated for a case study of a high-elevation system. Previous work indicated that canopy cover manipulation can serve as a means to alter streamflow patterns. Here, the role of vegetation in the system response is analyzed for both the historic meteorology and a for a future climate scenario. The changes in water and energy balance components when air temperature is increasing and the differences between the vegetated and open sites are discussed.

References:

Allen, R.G., Pereira, L.S., Raes, D., and Smith, M. (1998). "Crop evapotranspiration, guidelines for computing crop water requirements." *FAO Irrig. and Drain. Paper 56, Food and Agric. Orgn. of the United Nations, Rome, Italy.* 300 pp.

Bois, B., Pieri, P., Van Leeuwen, C., Wald, L., Huard, F., Gaudillere, J.-P., and Saur E. (2008). "Using remotely sensed solar radiation data for reference evapotranspiration estimation at a daily time step." *Agric. For. Meteorol.* 148 (4), 619-630.

Cristea, N. C., S. K. Kampf, and S.J. Burges (2012a). Linear models for estimating annual and growing season reference evapotranspiration using averages of weather variables, *Int. J. Climatol.* 32: 000–000, DOI: 10.1002/joc.3430.
<http://onlinelibrary.wiley.com/doi/10.1002/joc.3430/pdf>

Cristea, N.C., S. K. Kampf, and S.J. Burges (2012b). Revised coefficients for Priestley-Taylor and Makkink-Hansen equations for estimating daily reference evapotranspiration, in press, *Journal of Hydrologic Engineering*.
<http://ascelibrary.org/doi/pdf/10.1061/%28ASCE%29HE.1943-5584.0000679>

Dent, J.E. (2012). Climate and meteorological information requirements for water management. World Meteorological Organization, Technical Report Series No. 1, WMO-No. 1094.
http://www.wmo.int/pages/prog/hwrrp/publications/Technical_report_series/Climate_and_meteorological_info_requirement_for_WM_en.pdf

Jiang, L., Islam, S. (2001). Estimation of surface evaporation map over southern Great Plains using remote sensing data. *Water Resour. Res.*, 37, 329-340.

Wang, K., Li, Z., and Cribb, M. (2006). "Estimation of evaporative fraction from a combination of day and night land surface temperatures and NDVI: A new method to determine the Priestley-Taylor parameter." *Remote Sens. Environ.*, 102, 293-305.

Chapter 2. Revised coefficients for Priestley-Taylor and Makkink-Hansen equations for estimating daily reference evapotranspiration

Abstract

Many applications require estimation of reference evapotranspiration in areas where meteorological measurements are limited. Previous studies have shown that the data parsimonious radiation-based reference evapotranspiration (ET_0) model, Priestley-Taylor (PT), performs relatively well in humid climates, but it under-predicts ET_0 in drier and windier climates. In this paper, we compiled meteorological measurements at 106 locations in the contiguous US and calculated ET_0 using the PT and the Makkink with Hansen correction (MK-Ha) models. We compared these models to the more comprehensive Penman-Monteith equation (FAO-56 PM) estimates of ET_0 . Results showed that the simpler models were closest to the FAO-56 PM at sites where the annual mean relative humidity (RH) was about 70% and annual 2-m wind speed (U) was less than $2 \text{ m}\cdot\text{s}^{-1}$. We then developed equations for adjusting the PT and MK-Ha model coefficients using annual averages of RH (or vapor pressure deficit, VPD) and U to improve the performance of these models for drier and windier sites. Publicly available datasets of spatial distributions of annual RH and U were used to estimate local coefficients for the contiguous United States. The new coefficients were tested with additional data from 22 sites, not used for coefficient development. At the test sites, the performance of both PT and MK-Ha ET_0 models improved with the revised coefficients. Depending on the model, 63-90% of the stations had ET_0 within 10% of the FAO-56 PM ET_0 for the growing season. The revised coefficients can be used to improve estimation of reference ET_0 in data-limited applications such as remote sensing and distributed hydrologic modeling.

2.1. Introduction and background

Radiation based evapotranspiration models such as Priestley and Taylor, 1972 (PT) are widely used in hydrologic modeling (e.g. Bandaragoda et al. 2004; Wang et al. 2006b; Schramm et al. 2007; Soylu et al. 2011) and many other ecological applications. The PT model was derived for saturated conditions and open water sites where wind effects were negligible. The wind function multiplied by the vapor pressure deficit term in the Penman (1948) equation was eliminated, and the evaporative coefficient α was introduced, with an estimated average value of 1.26. This coefficient was later found to vary, depending on land cover and site conditions, and a relatively wide range of α (0.6 - 2.47) has been reported (Table 2.1). High values of α were found at dry and windy sites, and low values of α were found at humid sites, mostly in Canada, but also in other parts of the world (e.g. Kustas et al. 1996; Eaton et al. 2001). Compared with lysimeter data, the Priestley-Taylor model with $\alpha = 1.26$ was found to under-predict significantly in windy and arid conditions (Berengena and Gavilàn 2005; Benli et al. 2010), and to over-predict slightly in humid conditions (Yoder et al. 2005).

Table 2.1 Estimated values of the PT evaporative coefficient α for a range of climates and terrain covers.

Reference	α	Local conditions and study site
Pereira, 2004	1.26	perennial ryegrass, semiarid, Davis, CA, USA
	1.27	grass, humid tropical, Piracicaba, SP, Brazil
Zhang et al, 2004	1.17, 1.26	winter wheat, semiarid monsoon climate. North China Plain
	1.06, 1.09	maize, semiarid monsoon climate North China Plain
Castellvi et al., 2001	1.2-1.9	reference grass, semiarid, north-east Spain, monthly α
Kustas et al., 1996	0.6-1.0	mixture of rangeland, pasture and cropland, continental climate, Chickasha, OK, USA, half-hourly time step
Flint and Childs, 1991	0.9	partially vegetated clearcut forest site in southwest Oregon, USA water limited, α was related to soil moisture
Fisher et al, 2005	0.73, 0.94	ponderosa pine forest ecosystem at an AmeriFlux site in Northern California
Daneshkar Arasteh and Tajrishy, 2008	1.20-2.47	open water, arid conditions, Chahnimeh Reservoir, southeast Iran
Gavin and Agnew, 2004	0.8 - 1.25	wet grassland, Southeast England
Eaton et al., 2001	1.51-2.32	deep lake (Great Slave Lake), Northwest Territories, Canada
	1.17-1.45	shallow lake (Golf Lake), Churchill, Manitoba, Canada
	1.07-1.10	wetland tundra, Trail Valley Creek basin, Northwest Territories, Canada
	0.83-1.46	sedge wetland, Churchill, Manitoba, Canada
	1.00-1.08	shrub tundra, Trail Valley Creek basin, Northwest Territories, Canada
	0.95-1.20	shrub tundra, Churchill, Manitoba, Canada
	0.81-1.00	upland tundra, Churchill, Manitoba, Canada
	0.77	forest, Havikpak Creek, Northwest Territories, Canada
	0.94-0.95	Churchill spruce-tamarack forest Manitoba, Canada

Souch et al, 1996	1.035	wetlands in the Indiana Dunes National Lakeshore near Lake Michigan, Indiana, USA, hourly time step
*Stewart and Rouse,1976	1.26	shallow lake, Hudson Bay Coast, Ontario, Canada
*Bello and Smith, 1990	1.35	shallow lake, Northern Manitoba, Canada
*Rouse et al., 1977	1.26	wetland, Hudson Bay Coast, Ontario, Canada
*Price et al., 1991	1.20	wetland, Lake Melville, Newfoundland, Canada
*Rouse et al., 1977	0.95	upland tundra, Hudson Bay Coast, Ontario, Canada
*Rouse et al., 1977	1.13	coniferous forest, Lake Athabasca, Northwest Territories, Canada
**Jury and Tanner, 1975	1.57	strongly advective conditions
**Mukammal and Neumann, 1977	1.29	grass, soil at field capacity
**Davies and Allen, 1973	1.27	irrigated ryegrass
**McNaughton and Black, 1973	1.18	wet Douglas-fir forest
**De Bruin and Holtslag, 1982	1.12	short grass
**McNaughton and Black, 1973	1.05	Douglas-fir forest
**Barton, 1979	1.04	bare soil surface
**Black, 1979	0.84	Douglas-fir unthinned
	0.8	Douglas-fir thinned
**Giles et al., 1984	0.73	Douglas-fir forest (daytime)
**Shuttleworth and Calder, 1979	0.72	spruce forest (daytime)

* cited in Eaton et al., 2001

** originally cited in Flints and Childs (1991) and relisted in Fisher et al., 2005

Another radiation based model for calculating evapotranspiration, Makkink (1957), was also derived from Penman's 1948 model and was validated with lysimeter measurements collected in the Netherlands for short grass. De Bruin (1981, 1987) proposed modifications of the original Makkink model. Based on further research in the Netherlands and Denmark, the Makkink evaporative coefficient C was established equal to 0.7 (Hansen, 1984). The Makkink method with the Hansen correction, henceforth referred to as the Makkink-Hansen (MK-Ha) method, compared well with lysimeter data at a humid location in Germany (Xu and Chen 2005). Descriptions of both Priestley-Taylor and Makkink-Hansen models are given in the model description section of this paper.

A more comprehensive physically based model used to compute evapotranspiration is the Penman-Monteith model. The Food and Agriculture Organization of the United Nations (FAO) Irrigation and Drainage Paper 56 version of the Penman-Monteith model (FAO-56 PM) established the computational steps needed to calculate reference evapotranspiration ET_0 from a well watered surface of green grass of specified height, albedo, and surface resistance (Allen et al. 1998). The FAO-56 PM model has been shown consistently to perform well against measured data in a variety of climates (Garcia et al. 2004; Yoder et al. 2005; Lòpez-Urrea et al. 2006; Gavilàn et al. 2007; Benli et al. 2010). Compared with the radiation based models, PT and MK-Ha, that use as inputs net radiation (R_n), or solar radiation (R_s), and temperature (T), the FAO-56 PM

model is more data intensive, requiring, in addition to R_s and T , relative humidity (RH), and wind speed at 2 m height (U). Even though the PT and MK-Ha models have shown varying effectiveness in prior studies, the parsimonious structure and limited data requirements make these models attractive alternatives to the Penman-Monteith model in applications with limited data or in remote sensing applications (e.g. Jiang and Islam 2001; Wang et al. 2006a; Bois et al. 2008).

To improve the PT and MK-Ha performance, we have developed relationships to adjust the PT and MK-Ha evaporative coefficients using mean annual values of RH (or vapor pressure deficit, VPD) and U . The coefficients are estimated for grass but can be modified for other land cover types via crop factors. Because of the limited availability of observed ET_o datasets, we used the FAO-56 PM ET_o estimates as surrogate for measured data. Due to its broad acceptance, the FAO-56 PM is now routinely used as a base for comparison for simpler ET_o calculation methods (Irmak et al. 2003a), to adjust or calibrate other ET_o methods (Tabari and Hosseinzadeh Talaei 2011), or to develop new methods (e.g. Irmak et al. 2003b). The coefficients developed in this paper can be estimated from publicly available GIS datasets and can provide reliable ET_o estimates in situations with limited meteorological data.

The objectives of this paper are to: i) characterize the annual RH and U conditions for which the PT and MK-Ha ET_o predictions differ from FAO-56 PM ET_o and quantify the magnitude of these discrepancies, ii) develop and test coefficient adjustment relationships for the PT and MK-Ha models based on annual average RH (or VPD) and U , and provide maps of the adjusted coefficients, and iii) show which of the two methods performs best in comparison with FAO-56 PM at a daily time scale when using the original and newly developed coefficients. All findings are for the daily time step PT and MK-Ha models with applicability for the contiguous US.

2.2. Daily evapotranspiration models

2.2.1. FAO 56 Penman-Monteith

The daily time step FAO-56 PM model (1) estimates ET_o for the reference surface, defined as the “hypothetical reference crop with an assumed crop height of 0.12 m, a fixed surface resistance of 70 s m^{-1} and an albedo of 0.23, resembling “an extensive surface of green, well-watered grass of uniform height actively growing and shading the ground” (Allen et al. 1998):

$$ET_o = \frac{0.408\Delta(R_n) + \gamma \frac{900}{T + 273} U(e_s - e_a)}{\Delta + \gamma(1 + 0.34U)} \quad (2.1)$$

where: ET_o = FAO-56 PM reference evapotranspiration [mm d^{-1}]; R_n = calculated mean daily net radiation at the grass surface [$\text{MJ m}^{-2} \text{d}^{-1}$]; T = mean daily air temperature at 2-m height [$^{\circ}\text{C}$]; U = mean daily wind speed at 2-m height [m s^{-1}]; e_s = saturation vapor pressure [kPa], calculated as the average of saturation vapor pressures at the maximum and the minimum air temperatures; e_a = daily mean actual 2-m height vapor pressure [kPa]; Δ = slope of the saturation vapor pressure-temperature curve [$\text{kPa } ^{\circ}\text{C}^{-1}$]; γ = psychrometric constant [$\text{kPa } ^{\circ}\text{C}^{-1}$]. Details for calculating the daily values of Δ , γ , R_n , e_s , and e_a are provided in Allen et al. (1998). The vapor pressure deficit, VPD, was estimated as $VPD = e_s - e_a$ [kPa].

2.2.2. Priestley-Taylor

The equation used to compute daily ET_o rates with the PT model is:

$$ET_{oPT} = \alpha \frac{\Delta}{\Delta + \gamma} \frac{R_n}{\lambda} \quad (2.2)$$

where: ET_{oPT} = PT reference evapotranspiration [mm d^{-1}]; $\alpha = 1.26$, the PT evaporative coefficient [-]; λ = latent heat of vaporization at 20°C [2.45 MJ kg^{-1}]. Values of Δ , γ and R_n are calculated using the same procedure as for the FAO-56 PM model.

2.2.3. Makkink-Hansen

We used the Makkink method with the Hansen (1984) correction (MK-Ha) to compute daily ET_o rates as:

$$ET_{oMK-Ha} = C \frac{\Delta}{\Delta + \gamma} \frac{R_s}{\lambda}, \quad (2.3)$$

where: ET_{oMK-Ha} = reference evapotranspiration [mm d^{-1}]; $C = 0.7$ the evaporative coefficient proposed by Hansen (1984); R_s is the mean daily solar radiation [$\text{MJ m}^{-2} \text{d}^{-1}$], and the remaining variables are defined using the same procedure as in the FAO-56 PM model.

2.3. Methods

To develop and test the ET_o equations, we retrieved weather datasets from 106 locations that represent a range of climates across the contiguous US (see Appendix 2A-I for data sources). We checked these data for integrity and quality. We then compared the PT and MK-Ha daily ET_o estimates using the original coefficients at the 106 study sites with the FAO-56 ET_o for the growing season period. This period may vary between the study sites as a function of climate, but for consistency, we used the period April 1 to September 30 for all stations and refer to this time range henceforth as the growing season period.

In the second step for each station we calibrated the PT and MK-Ha evaporative coefficients, α and C , by minimizing the sum of the squared residuals between the benchmark FAO-56 PM ET_o , and the PT and MK-Ha models. We then re-evaluated the calibrated PT and MK-Ha model predictions. Next we applied multiple linear regression techniques and the results from the previous step to develop coefficient adjustment relationships for the PT and MK-Ha models based on annual averages of RH and U . Once the equations were established, spatial distributions of annual RH (New et al., 1999) and U (National Renewable Energy Laboratory, NREL, 1996) were used to generate PT and MK-Ha coefficient maps for the contiguous US. In the fourth step we tested the performance of the conditional coefficients with weather data from 22 stations, not included in the original dataset. For these test stations, we used both coefficient values estimated with the annual RH and U from the station records and the map values calculated in the third step.

The effectiveness of the adjusted coefficients was evaluated using the root mean square error $RMSE$, the index of agreement d (Willmott 1982), and the ratio between the PT and MK-Ha ET_o and FAO-56 PM ET_o , for the growing season, r . Equations used for these measures are:

$$RMSE = \left[N^{-1} \sum_i^N (ET_{o,pi} - ET_{o,i})^2 \right]^{0.5} \quad (2.4)$$

$$d = 1 - \left[\frac{\sum_{i=1}^N (ET_{o,pi} - ET_{o,i})^2}{\sum_{i=1}^N (|ET_{o,pi}'| - |ET_{o,i}'|)^2} \right], \quad 0 \leq d \leq 1, \quad (2.5)$$

$$\text{with } ET_{o,pi}' = ET_{o,pi} - \overline{ET_o}; \quad ET_{o,i}' = ET_{o,i} - \overline{ET_o}, \text{ and}$$

$$r = \frac{\sum_i^N ET_{o,pi}}{\sum_i^N ET_{o,i}} \quad (2.6)$$

where i is the index for the day, $ET_{o,pi}$ refers to daily ET_o rates from either PT or MK-Ha, and $ET_{o,i}$ is the FAO-56 PM daily ET_o rate. The PT and MK-Ha methods approximate best the FAO-56 PM when the $RMSE$ is small and when d and r approach unity.

2.4. Meteorological datasets

The meteorological datasets were retrieved primarily from agricultural weather network sites that recorded hourly values of T , R_s , RH and U . Selected stations are from 106 locations shown in Figure 2.1 as open circles, where circle size represents the estimated United Nations Environment Programme (UNEP, 1992) aridity index class AI_u , defined as the ratio between the annual precipitation and annual potential evapotranspiration. Larger circles are shown for humid climates, smaller circles for dry climates. Twenty-two additional stations in Figure 2.1, shown as solid triangles, were

used as test sites. The map was produced from USGS (2003) Geographic Information System (GIS) datasets.

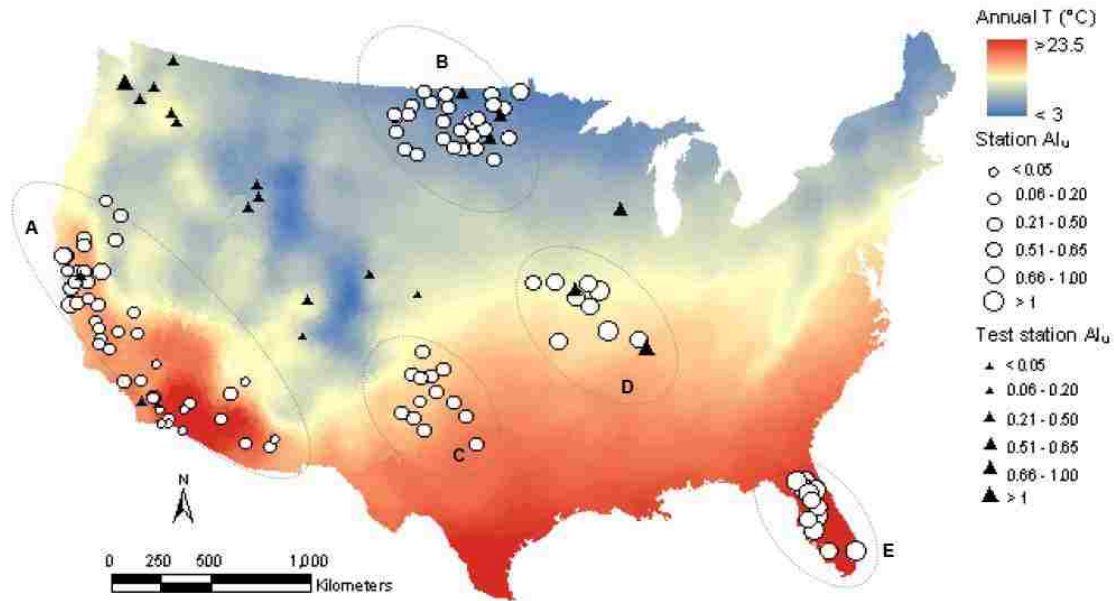


Figure 2.1 Locations and UNEP aridity index of study and test sites displayed on the annual average air temperature US map.

The criteria for selecting the locations shown in Figure 2.1 were: (i) availability of continuous and consistent hourly meteorological data (T , RH, U and R_s) for 3 to 5 years; and (ii) representativeness for a range of climates and latitudes. The weather data time series from all stations were checked for continuity and quality. Linear interpolation was used for records with missing periods of less than 3 hours. For longer periods, we used the filling guidelines provided in Allen et al. (1998). Less than 5% of the data required any fill-in procedures. For 100 of the 106 stations, 5 years of data were used from each station, while for the remaining 6 stations, 4 years (5 locations) and 3 years (1 location), respectively, were considered. Daily average values of input weather variables were derived from the hourly data series.

Based on the Köppen-Geiger classification, the climate conditions vary significantly between the 106 sites (open circles) shown in Figure 2.1. In Region A, California and Arizona, they range from Mediterranean in the southern part to more continental towards the inland, and to semi-arid and arid in the southeastern areas. Most arid stations are located in Arizona, where annual averages of RH are low, and mean annual T can reach 20-21 °C. Region B has a continental climate, with the eastern part characterized by humid continental conditions with warm summers and cold winters and the western part by drier conditions, with less precipitation. Generally, region B has relatively low mean annual T , 3.8-7.2 °C, and high mean annual U , 3.2 -5.4 m·s⁻¹. The stations in region C are mostly located in the Texas High Plains area characterized by a semi-arid climate, with hot summers and significant temperature changes from day to

night, and mild winters. Stations in region D have a humid continental climate with about 12-14°C mean annual T , with cold winters and hot summers and, at times, significant swings in air temperatures during the summer months. The climate of region E (Florida) is humid subtropical in the north and tropical in the south, with long, humid, warm summers and mild winters with positive temperatures. Region E generally has high mean annual T , 20-24°C, high mean annual RH, 74 – 79% and low mean U , typically less than 2 m·s⁻¹.

Regions A - E span a range of different climate types across the contiguous US, as shown in the updated Köppen-Geiger map of Peel et al. (2007). (See Appendix 2A-III for details for accessing the Köppen-Geiger maps). Of the 22 test stations, shown as solid triangles in Figure 2.1, 8 were selected from regions A, B, and D and 14 from locations outside regions A-E. These additional locations include the mountainous areas in Idaho, maritime and humid Western Washington, semi-arid Eastern Washington and Colorado, and continental Wisconsin. The annual average T at the test stations ranges from 4.8 to 22.7 °C; the annual average RH and annual average U range from 46.7 to 79.1%, and 1.1 to 4.4 m·s⁻¹, respectively. Site characteristics are summarized in Appendix 2B.

2.5. Results

2.5.1. Daily ET_o estimates before and after local calibration

To compare PT and MK-Ha models to the FAO-56 PM equation, we calculated the ratios between the total growing season ET_o from the simpler models to the FAO-56 PM ET_o, referred to as r_{PT} and r_{MK-Ha} . At humid and lower wind speed sites, the two methods estimated relatively well the FAO-56 PM ET_o. Figure 2.2a shows that the PT model was within about 5% of the FAO-56 PM ET_o at sites where the annual RH ranged between 68% and 75%, and annual U was less than about 2 m·s⁻¹. For annual RH larger than 75% and annual U less than 1.5 m·s⁻¹, the daily PT model overestimated the FAO-56 PM ET_o. Figure 2.2b shows that the MK-Ha ET_o approximated best the FAO-56 PM ET_o at sites where the annual RH was generally higher than 70% and annual U was lower than 2 m·s⁻¹.

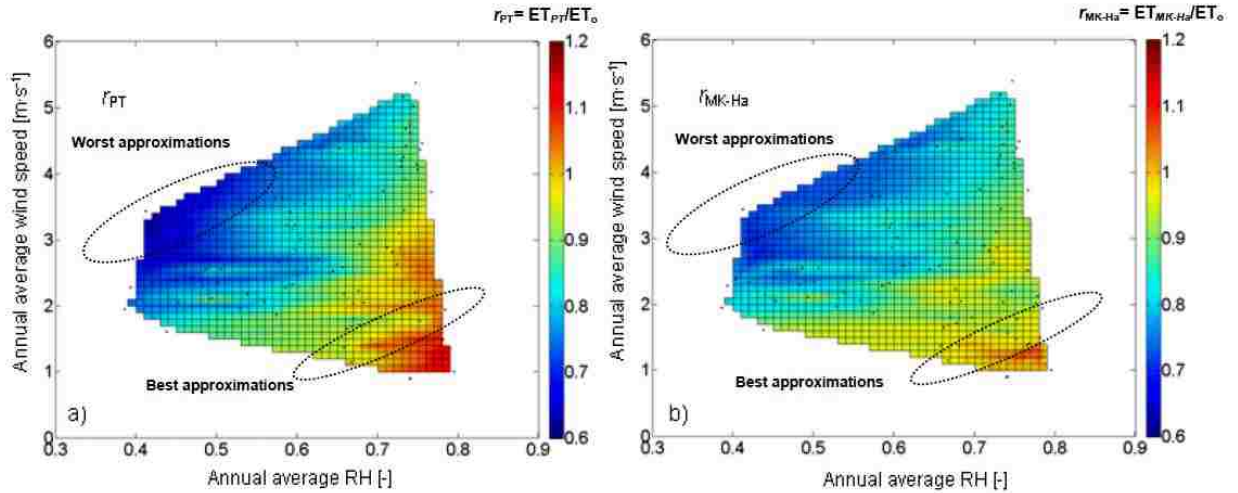


Figure 2.2 Ratios r_{PT} of the growing season PT ET_0 to FAO-56 PM ET_0 (a), and MK-Ha ET_0 to FAO-56 PM ET_0 (b), as function of annual RH and U . Dots represent station-based calculations of r_{PT} and r_{MK-Ha} , and filled areas are developed from a projected triangle based linear interpolation grid.

Figure 2.3 shows examples of local calibration of the PT and MK-Ha daily ET_0 models at two different stations: Buckeye, Arizona, and Wishek, North Dakota. The first station is located in an arid region characterized by high annual average T (21-22 °C), low annual average RH (38-40%), high annual average R_s (235 $W \cdot m^{-2}$) and moderate annual average U (2 $m \cdot s^{-1}$). In contrast, the second station has low annual average T (5-6 °C), high RH (73-75%), low R_s (160 $W \cdot m^{-2}$) and high U (5.6 $m \cdot s^{-1}$). Figure 2.3a and b show that for the Arizona station at low RH conditions and relatively low U , the discrepancies between the simpler models and the FAO-56 PM ET_0 were reduced through calibrating the evaporative coefficients, with the resulting residuals having a more uniform spread around zero. For the windy North Dakota site, the calibrated coefficients, α and C , corrected the general trend of the PT and MK-Ha ET_0 daily variations, but the highest FAO-56 PM ET_0 rates remained under-predicted by the simpler models, even with the calibrated coefficients (Figure 2.3c and d). Plots are shown for the 2006 growing season.

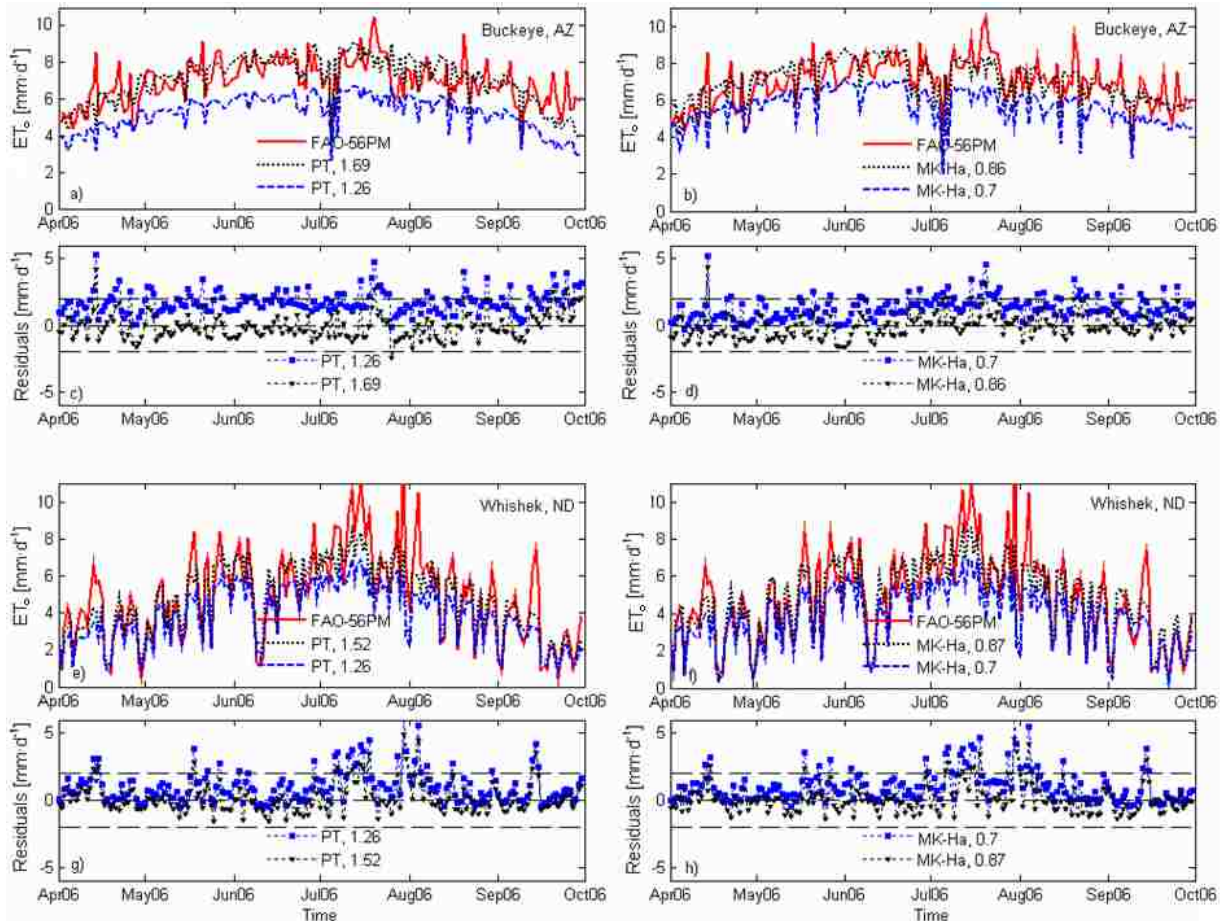


Figure 2.3 Examples of local calibration of the PT and MK-Ha models for April to October 2006 daily evaporation at Buckeye, AZ (a-d), and Whishek, ND (e-h).

The variability of the estimated r_{PT} and r_{MK-Ha} at all stations is also shown in Figure 2.4a as box-and-whisker plots before calibration (r_{PT} and r_{MK-Ha}) and after local calibration (r_{PT-c} and $r_{MK-Ha-c}$). Outliers are defined to be outside of the $Q_1 - 1.5 * (Q_3 - Q_1)$ to $Q_3 + 1.5 * (Q_3 - Q_1)$ interval, where Q_1 is the 25th percentile and Q_3 is the 75th percentile in each of the four datasets. The values of r_{PT} and r_{MK-Ha} range over intervals from 0.62 to 1.14 and 0.70 to 1.10, respectively, with the lowest values at arid and windy sites and the highest values for the humid sites, as illustrated also in Figure 2.2. Median values are 0.86 for both methods. Both r_{PT} and r_{MK-Ha} intervals were substantially reduced after calibration to 0.97 to 1.01, and 0.96 to 1.01, respectively (Figure 2.4a, last two boxplots), with a median of 0.99 in both cases. The values of the calibrated PT α_c and MK-Ha C_c coefficients ranged between 1.11 to 2.00 and 0.63 to 1.01, with higher values at low RH and windy sites and lower values at humid sites (Figure 2.4b).

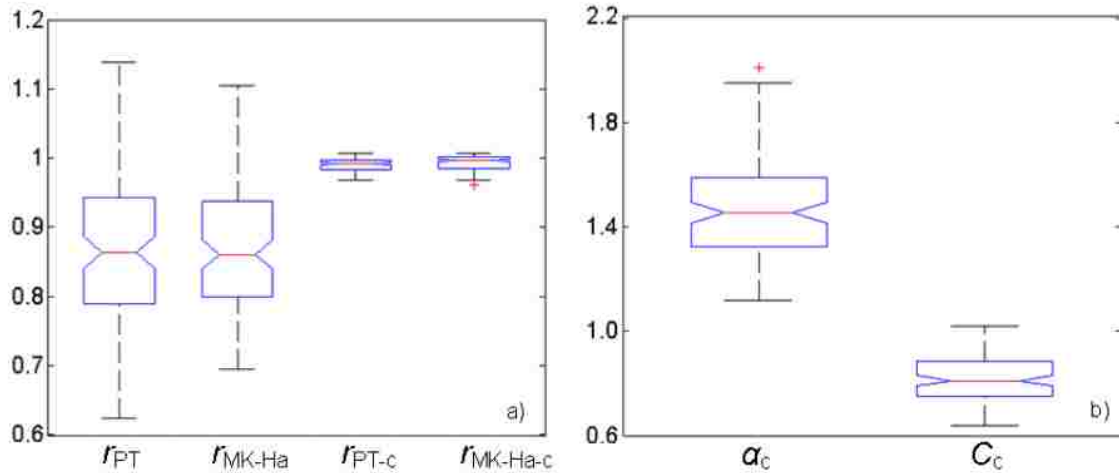


Figure 2.4 (a) Ratios of the growing season PT ET_o to FAO-56 PM ET_o and MK-Ha ET_o to FAO-56 PM ET_o before and after local calibration; (b) ranges of the calibrated α and C .

2.5.2. Daily evaporative coefficients relationships

Figure 2.3 and Figure 2.4a show that the site-calibrated evaporative coefficients improved the performance of the PT and MK-Ha ET_o models, especially at dry and windy sites. To develop prediction equations for local α and C we used multiple linear regressions with mean annual RH (or mean annual VPD) and mean annual U as independent variables. The equations have the following generic form, for which coefficients b_1 , b_2 and b_3 were determined:

$$\alpha, C = b_1 + b_2 \cdot \text{RH (or VPD)} + b_3 \cdot U, \quad (2.7)$$

where RH varies between 0 and 1, VPD is in [kPa], and U is in [$\text{m}\cdot\text{s}^{-1}$] (Figure 2.5). Table 2.2 lists the $b_{1,2,3}$ coefficients, the 95% confidence intervals (CI) for each b , and the explained variance, r^2 .

Table 2.2 Multiple linear regression coefficients $b_{1,2,3}$, 95% CI and r^2

	b_1	95% CI b_1	b_2	95% CI b_2	b_3	95% CI b_3	r^2
$(\alpha)_{\text{RH}, U}$	2.214	2.116 - 2.311	-1.526	-1.668 -1.384	0.079	0.065 0.092	0.84
$(C)_{\text{RH}, U}$	1.036	0.984 - 1.089	-0.527	-0.604 -0.450	0.041	0.033 0.048	0.72
$(\alpha)_{\text{VPD}, U}$	0.717	0.647 0.786	0.387	0.349 0.426	0.122	0.107 0.138	0.85
$(C)_{\text{VPD}, U}$	0.493	0.467 0.519	0.152	0.137 0.166	0.058	0.052 0.064	0.82

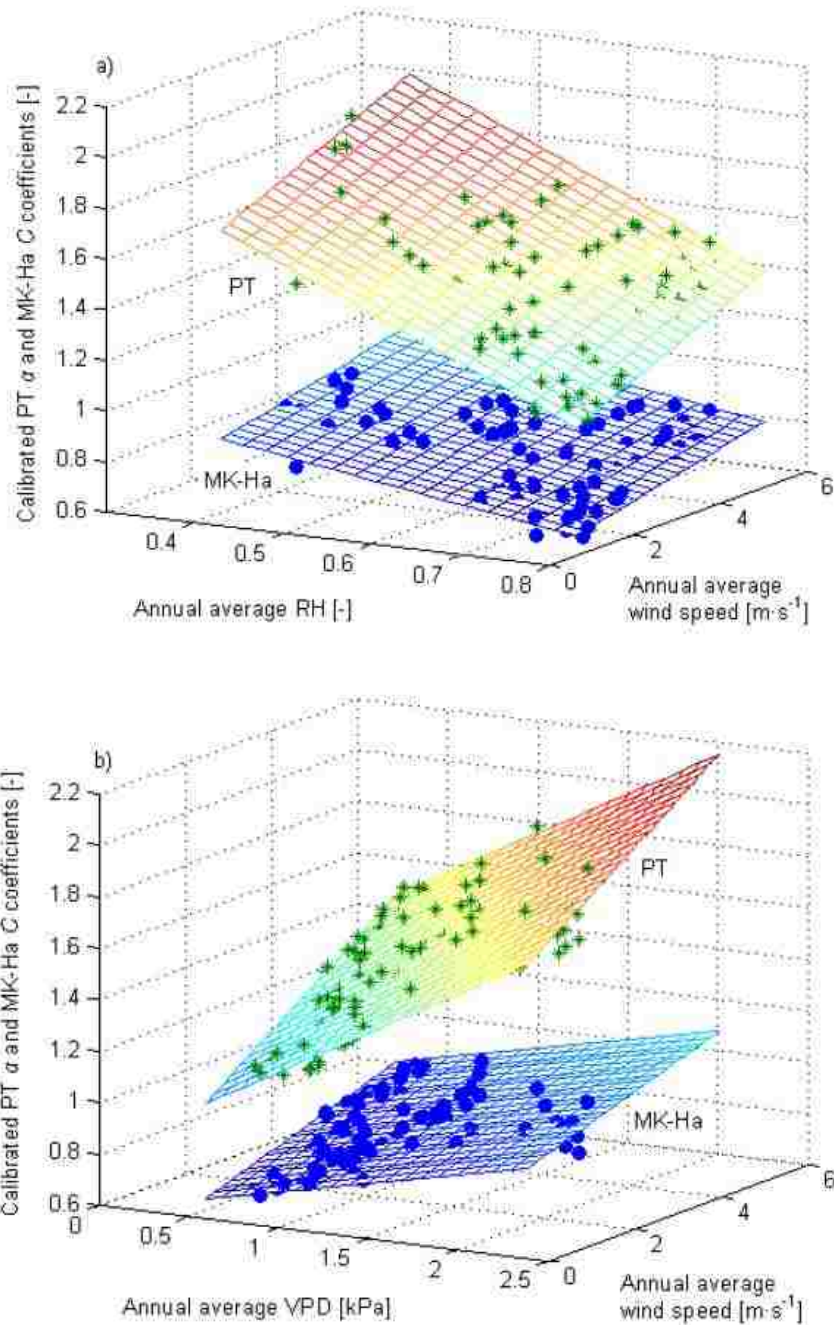


Figure 2.5 Multiple linear regressions based on mean annual RH and U (a), or VPD and U (b), for the PT, and MK-Ha, ET_o models' evaporative coefficients, α and C .

The variables, RH, and U , (or VPD and U) used in Eq. 2.7 were tested for linear dependence ($r^2 = 0.01$ and 0.14 , respectively) and can be treated as independent. Coefficients α and C had the strongest correlation (as a second order polynomial) with annual RH (VPD), with the PT α having the highest correlation ($r^2 = 0.65$ with RH and $r^2 =$

0.40 with VPD). The correlation was weaker with U and R_s and zero with annual T . The calibrated values of α and C followed a linear relationship (Figure 2.6).

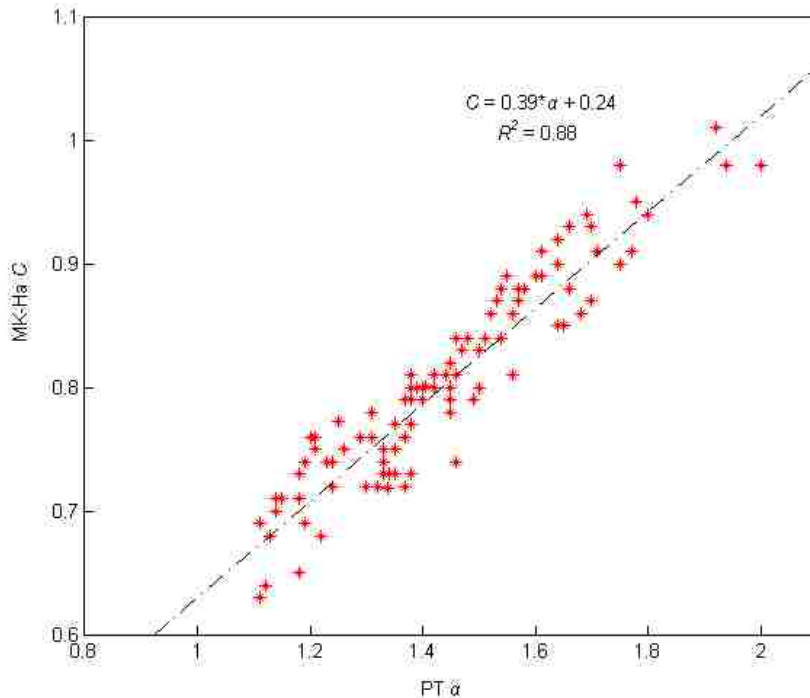


Figure 2.6 Linear relationship between the calibrated PT α and MK-Ha C coefficients.

2.6. Maps of evaporative model coefficients

Maps of the PT and MK evaporative coefficients were generated for the contiguous US based on Eq. 2.7 and the spatial distributions of annual average RH (New et al., 1999; Figure 2.7a) and U derived from the NREL, 1986 dataset (see Appendix 2A-II for online resources). The NREL dataset provides wind speed at 10m height, U_{10} , shown in Figure 2.7b. This was further converted into U at 2-m height using the following correction formula (Allen et al. 1994):

$$U = U_z \left[\frac{4.87}{\ln(67.8 \cdot z - 5.42)} \right], \text{ where } U_z = U_{10} \text{ and } z = 10\text{m.} \quad (2.8)$$

The maps in Figure 2.7c-d show that larger values of α and C were estimated for windy locations (e.g. mountainous areas) and low annual average RH areas (e.g. Arizona and eastern California), while smaller values were estimated for the humid and less windy areas such as the warm and humid southeastern region of the US (Figure 2.7c-d). Details for obtaining ArcGIS coefficient maps are given in Appendix 2A-IV.

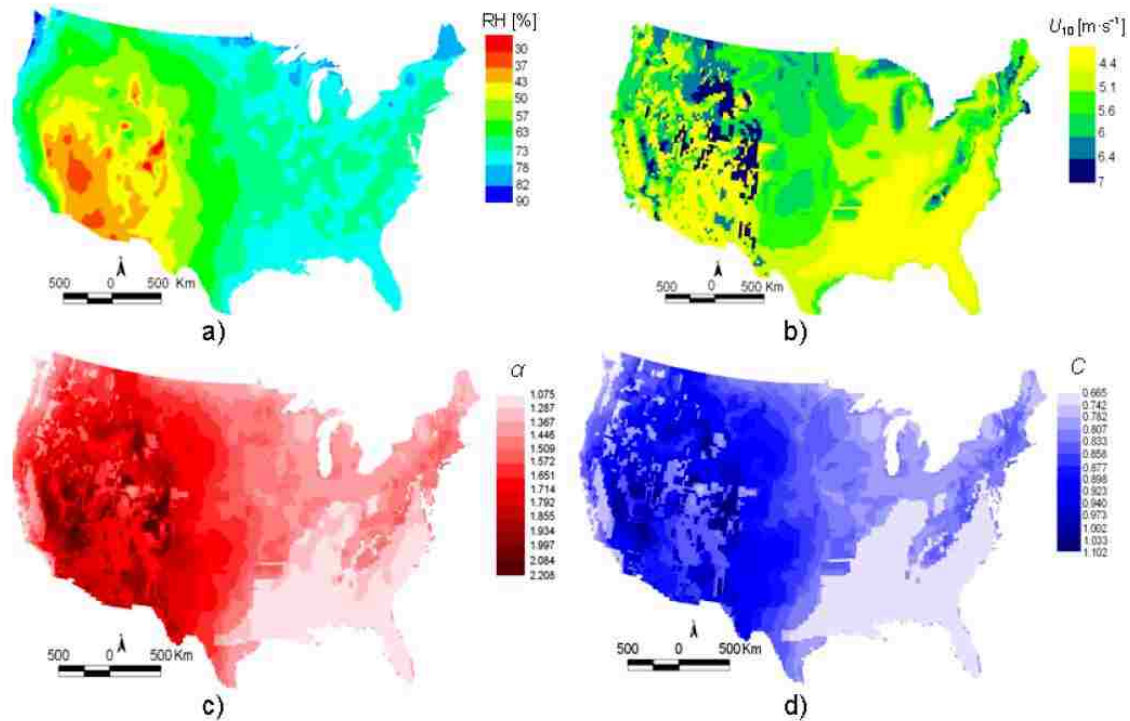


Figure 2.7 Spatial distributions of annual average RH (a), annual average U_{10} (b), α (c), and C (d) for the contiguous US.

2.7. Model tests

We estimated the PT and MK-Ha evaporative coefficients α and C at the test stations in two ways: i) using the annual average RH (or VPD) and U data from the station records in Eq. 2.7, and ii) extracting the coefficients from the generated coefficient maps showed in Figure 2.7c-d. The two sets of α and C estimates are listed in Appendix 2B, which shows that generally there was good agreement between the station and map estimates of α and C . All performance measures (Eq 2.4-2.6) showed improvements in the PT and MK-Ha ET_o predictions when using either the station or the map coefficients, compared with the original coefficient values. All models with revised coefficients show reduced ranges of $RMSE$, d , and r values relative to the values with the original coefficients (Figure 2.8). The r performance statistic shows the greatest improvement, with median values increasing from <0.9 for the original coefficients to between 5% of unity for all models with the revised coefficients (Figure 2.8c). Changes in $RMSE$ and d were more variable between models. With the original coefficients, median $RMSE$ values were close to 1 for both models and were reduced to 0.78-0.85 for the revised coefficients using either the RH and U equation or the map coefficients (Figure 2.8a). Median $RMSE$ values did not change between the original coefficients and the coefficients from the VPD and U equation. Median values of d were around 0.9 for the original coefficients and did not significantly improve for the RH and U equation and the map coefficients, but the spread was greatly reduced (Figure 2.8b). Median values of d did not improve for the VPD and U equation.

The best performing method based on the r criterion is the MK-Ha model with the coefficients adjusted based on the RH and U equation and station data, for which all values in the inter-quartile range fell within $\pm 5\%$ of the FAO-56 PM ET_0 . The map derived coefficients improved the PT and MK-Ha model predictions and provided results comparable with those obtained by using the station coefficients.

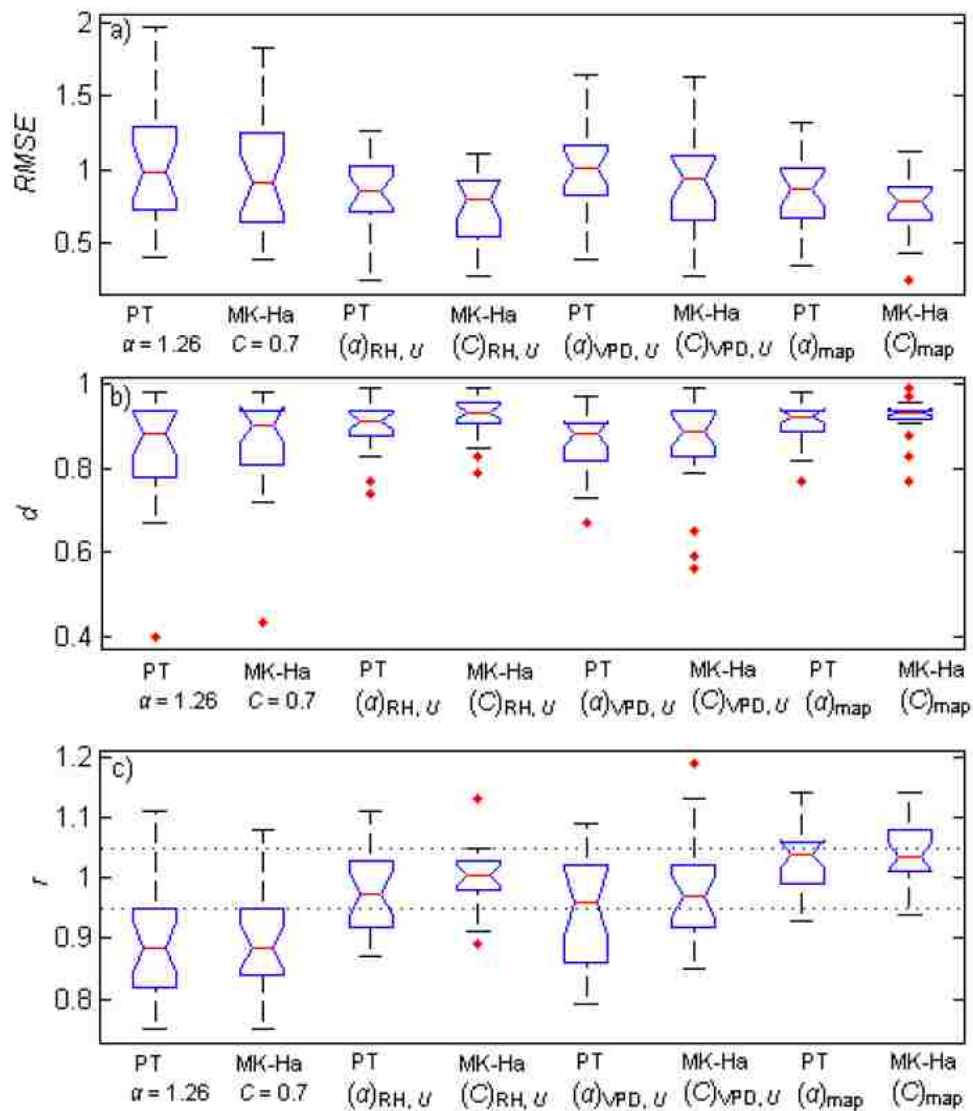


Figure 2.8 Box plots of $RMSE$ (a), d (b), and r (c) at the test stations for the original, station specific, and map derived, α and C coefficients. Dotted lines in (c) identify the 0.95 and 1.05 values.

In addition to numerical measures, scatterplots are useful to highlight discrepancies between the FAO-56 PM ET_0 estimates and those of the simpler models (Willmott 1982). Scatterplots are shown for four example test stations (Puyallup, WA; Spring Green, WI; Kettle Butte, ID, and Oasis, CA), with site characteristics summarized in

Appendix 2B. The PT and MK-Ha daily ET_o were plotted against the FAO-56 PM ET_o using the original coefficients (Figure 2.9a-d and i-l) and the station specific coefficients for both sets of independent variables RH and U , and VPD and U , respectively (Figure 2.9e-h and m-p). At the humid station (Puyallup, WA) the PT and MK-Ha models approximated best the FAO-56 PM ET_o , at both low and high rates. As the annual average RH decreased and annual average U increased (Spring Green, WI, and Kettle Butte, ID), the scatter increased around the one-to-one line, especially at the more windy location (Kettle Butte, ID), where the highest FAO-56 PM ET_o rates remained under-predicted by both the PT and MK-Ha models. At the low RH station (Oasis, CA), the adjusted coefficients corrected the general magnitude of the PT and MK-Ha ET_o , but considerable scatter around the one-to-one line remained. The $RMSE$, d , and r measures indicate that in general, performances of the PT and MK-Ha models, with RH and U as independent variables for the evaporative coefficients α and C , were better than when using VPD and U as independent variables for a range of climates (Figure 2.8). Among the sites shown in Figure 2.9, the PT and MK-Ha models with the coefficients estimated using VPD and U approximated better FAO-56 PM at the Spring Green station only. The predicted PT and MK-Ha ET_o rates with RH and U as independent variables for the evaporative coefficient in Eq 2.7 were slightly higher (less than 5%) than those estimated with VPD and U at all stations in Figure 2.9, with the exception of the arid Oasis, CA location, where they were 5% lower.

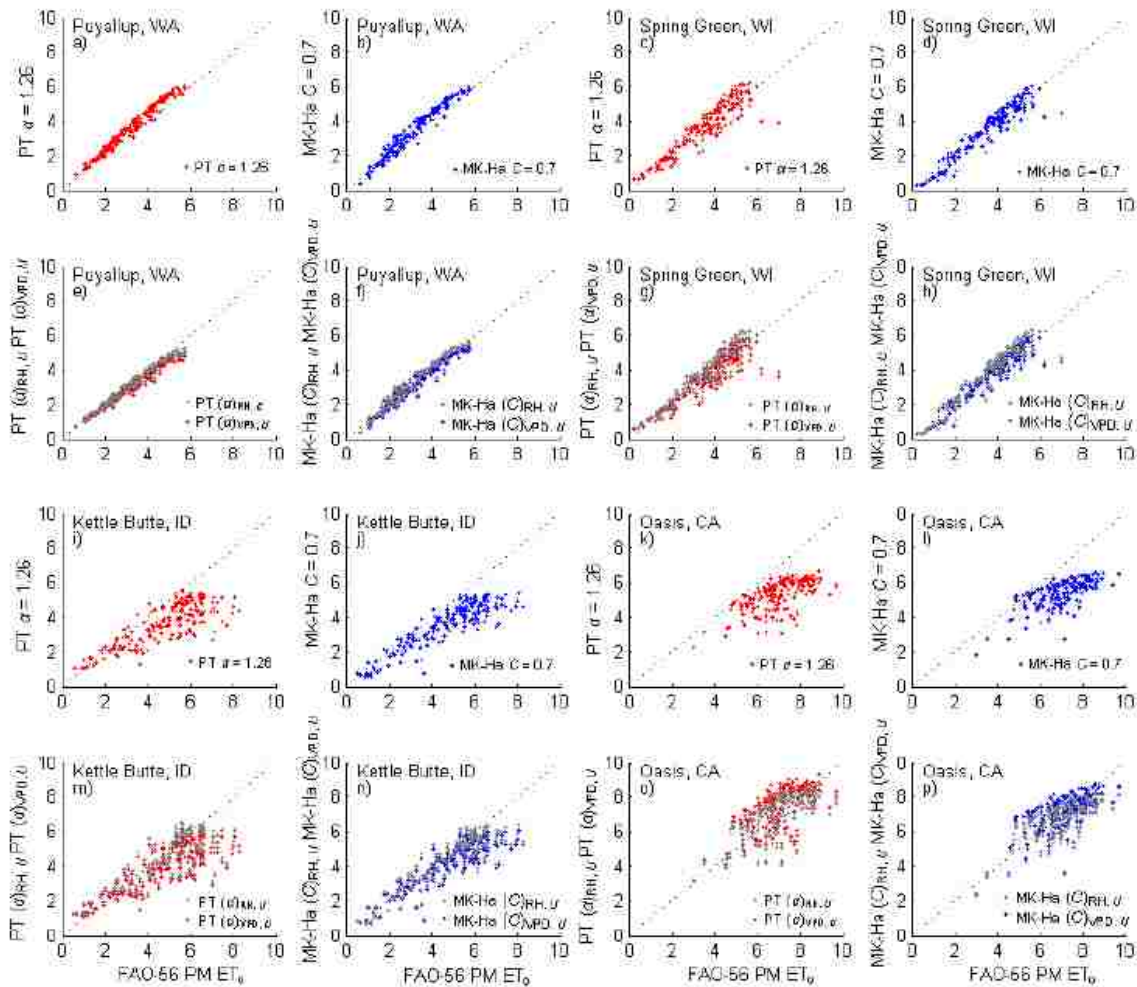


Figure 2.9 Scatterplots of the FAO-56 PM ET_0 and PT and MK-Ha ET_0 in $mm\ d^{-1}$, estimated with the original coefficients ((a) – (d) and (i) – (l)) and with coefficients estimated based on the RH and U (grey color), and VPD and U (red color) relationships, respectively ((e) – (h), and (m) – (p)) at four test stations. Dotted line is the one-to-one relationship.

2.8. Discussion

The PT model with the original coefficient $\alpha = 1.26$ underestimated the FAO-56 PM growing season ET_0 at dry and windy sites. This behavior, also noted in studies that compared the PT ET_0 estimates with lysimeter data (e.g. Berengena and Gavilán 2005, Benli et al. 2010), is expected because the original PT model was derived for low wind conditions (Priestley and Taylor 1972). The largest discrepancies were found at arid and semi-arid sites, where the estimated growing season ET_0 was as low as 62 to 70% of the FAO-56 PM ET_0 (Figure 2.2). We found that the original PT model approximated the growing season FAO-56 PM ET_0 within about 5% at humid sites where the annual average RH ranged from 68 to 75%, and U was less than $2\ m\ s^{-1}$.

At sites where annual average RH was higher than 75%, and annual average U was less than $1.5 \text{ m}\cdot\text{s}^{-1}$, the PT model overestimated the FAO-56 PM growing season ET_o (Figure 2.2a). For this dataset, r_{PT} exceeded unity at 16 stations where annual RH varied between 68 and 79%. These stations were mostly located in Florida, Missouri, and coastal areas of California. Overestimations of the FAO-56 PM ET_o or lysimeter data by the original PT model were also reported for other humid sites. Suleiman and Hoogenboom (2007) found that the daily PT model overestimated the FAO-56 PM in the humid climate of Georgia, and Yoder et al. (2005) showed that the PT model overestimated lysimeter measurements in the humid climate of Eastern Tennessee during the summer months, when the monthly averages of RH and U varied between 76.4 and 83.5% and 0.9 and $1.2 \text{ m}\cdot\text{s}^{-1}$, respectively.

The MK-Ha model with the original coefficient, $C = 0.7$, compared well against lysimeter data at a humid site in Germany (Xu and Chen 2005), but we found no studies where this model was applied for drier conditions and compared with the FAO-56 PM or measured data. At our study locations, the MK-Ha model with $C = 0.7$ shows the same tendency as the PT model to underestimate the FAO-56 PM growing season ET_o , albeit to a slightly smaller degree (Figure 2.2b). The method approximated the FAO-56 PM best at sites where annual average RH was larger than 70%, and U was less than $2 \text{ m}\cdot\text{s}^{-1}$ (Figure 2.2b).

Use of equation 2.7 to estimate the PT and MK-Ha coefficients improved the performance of the simpler models when compared with FAO-56 PM. Jensen (1990) recommended a value of α between 1.7 and 1.75 to improve the PT ET_o predictions at arid sites. The equations we developed offer greater flexibility for a range of RH (or VPD) and U conditions. Spatial distributions (maps) of the PT and MK-Ha coefficients for the contiguous US were also provided. Despite uncertainties associated with using the map coefficients (Figure 2.7c-d), the PT and MK-Ha model predictions at 22 test stations improved over the original estimates and were of comparable accuracy with the corresponding predictions using the coefficients estimated from Eq. 2.7 and the station annual average RH and U data (Figure 2.8). Uncertainties associated with the map coefficients are unquantifiable, but depend primarily on the quality of spatial datasets for RH and U , which in turn depend on the accuracy and robustness of point measured data, uneven spatial coverage, and map interpolation techniques. The wind speed spatial dataset includes additional uncertainty related to using the NREL dataset to represent U_{10} , and the conversion from U_{10} to U at 2-m height using Eq. 2.8.

Although the proposed relationships were developed using only weather station data from the contiguous US, they covered a relatively large range of climate conditions represented by the annual average RH and U intervals shown in Figure 2.2. Therefore, these relationships may be valid in other parts of the world within similar ranges. Extrapolation beyond these intervals will require additional testing.

The MK-Ha model is used much less frequently than the PT model, but our results show that, compared with the PT model, the MK-Ha model offers three advantages. First it uses air temperature, T , and solar radiation, R_s rather than the net radiation, R_n as input data. Net radiation R_n is not typically measured at standard weather stations, and its use in most R_n -based ET_o equations requires approximations and additional computational steps (e.g. Allen et al. 1998). Second, the MK-Ha model with the original C coefficient approximates the FAO-56 PM ET_o slightly better than the PT with the original coefficients (Figure 2.2, Figure 2.3a). Third, the variability of the calibrated C is smaller than the variability of calibrated α (Figure 2.3b), increasing the chance for better prediction of the FAO-56 PM ET_o .

We chose the FAO-56 PM model as a base for comparison in place of observations due to the lack of measured reference evapotranspiration data over a wide enough range of climates. Similar approaches have been used (e.g. Irmak et al. 2003b), based on the recommendation of the FAO Expert Consultation on Revision of FAO Methodologies for Crop Water Requirements (Smith et al. 1991) that empirical methods should be calibrated or validated for new regions using the FAO-56 PM equation. Limitations associated with datasets we used include any undetected measurement errors in the weather variables and uncertainties associated with the annual average RH and U spatial distributions shown in Figure 7a-b.

2.9. Summary and Conclusions

We compared the performance of the Priestley-Taylor (PT) and Makkink-Hansen (MK-Ha) reference evapotranspiration (ET_o) models with their original coefficients, $\alpha = 1.26$, and $C = 0.7$ respectively, to the FAO-56 PM ET_o model using meteorological data from 106 stations that represent a relatively large range of climates across the contiguous US. The original PT and MK-Ha models approximated best the FAO-56 PM ET_o at humid and less windy sites and under-predicted at drier sites and windier sites. The simpler models were closest to FAO-56 PM at sites where the annual mean relative humidity (RH) was about 70% and annual 2-m wind speed (U) was less than $2 \text{ m}\cdot\text{s}^{-1}$. Local calibration significantly improved the performance of the PT and MK-Ha models. At the study sites, locally calibrated PT and MK-Ha evaporative coefficients, α_c and C_c , ranged between 1.11 to 2.00, and 0.63 to 1.01, respectively.

We developed equations to estimate α and C (Eq. 2.7) for the PT and MK-Ha ET_o daily models using mean annual RH (or VPD) and 2-m elevation wind speed U as independent variables. The efficiency of these equations was tested at 22 stations not included in the original dataset in two scenarios: i) assuming that station annual average RH (or VPD) and U data are available, and ii) assuming that the RH and U data are not available, in which case site-specific model coefficients were taken from coefficient maps generated using existing spatial datasets of annual average RH and U . In both cases, the performance of the PT and MK-Ha models improved when compared with the estimates

that used the original model coefficients. At the test sites, the improved models predicted ET_o values for the growing season within 5% of the FAO-56 PM ET_o values at 45-72% of stations and within 10% of FAO PM at 63-90% of stations. The best performing model was MK-Ha with coefficients estimated from annual average RH and U . The new PT and MK-Ha models can be used to improve ET_o estimates when spatial distributions of ET_o may be needed, such as in distributed hydrologic modeling or remote sensing applications.

Our analysis shows that the MK-Ha model is preferable to the PT model because of its lower data requirements and smaller model coefficient variability over a range of climates. In cases where only air temperature T is recorded at a station, solar radiation R_s needed as input in the MK-Ha model can be estimated with available R_s models (see, e.g. Allen et al. 1998).

2.10. References

Allen, R.G., Pereira, L.S., Raes, D., and Smith, M. (1998). "Crop evapotranspiration, guidelines for computing crop water requirements." *FAO Irrig. and Drain. Paper 56, Food and Agric. Orgn. of the United Nations*, Rome, Italy. 300 pp.

Allen R.G., Smith, M., Perier, A., and Pereira L.S. (1994). "An update for the definition and calculation of reference evapotranspiration." *ICID Bull.* 43, 35–92.

Bandaragoda, C. , Tarboton, D. G., and Woods, R. (2004). "Application of TOPNET in the distributed model intercomparison project." *J. Hydrol.*, 298, 178– 201, doi:10.1016/j.jhydrol.2004.03.038.

Benli, B., Bruggeman, A., Oweis, T., and Ustun, H. (2010). "Performance of Penman-Monteith FAO56 in a semiarid highland environment". *J. Irrig. Drain. Eng.* 136 (11) 757-765.

Berengena, J. and Gavilàn, P. (2005). "Reference evapotranspiration estimation in a highly advective semiarid environment." *J. Irrig. Drain. Eng.* 131 (2) 147-163.

Bois, B., Pieri, P., Van Leeuwen, C., Wald, L., Huard, F., Gaudillere, J.-P., and Saur E. (2008). "Using remotely sensed solar radiation data for reference evapotranspiration estimation at a daily time step." *Agric. For. Meteorol.* 148 (4), 619-630.

Castellvi, F., Stockle, C.O., Perez, P.J., and Ibanez M. (2001). "Comparison of methods for applying the Priestley-Taylor equation at a regional scale." *Hydrol. Processes* 15, 1609-1620.

- Fisher, J. B., DeBiase, T. A., Qi, Y., Xu, M., and Goldstein, A. H. (2005). "Evapotranspiration models compared on a Sierra Nevada forest ecosystem." *Environ. Modell. Softw.* 20 (6) 783-796.
- Daneshkar Arasteh, P. and Tajrishy M. (2008). "Calibrating Priestley-Taylor model to estimate open water evaporation under regional advection using volume balance method – case study: Chahnimeh Reservoir, Iran." *Journal of Applied Sciences* 8 (22) 4097-4104.
- De Bruin, H. A. R. 1981. "The determination of (reference crop) evapotranspiration from routine weather data, in Evaporation in relation to hydrology (Technical Meeting of the Committee for Hydrological Research, February, 1981)." *Comm. Hydrol. Res. TNO, Den Haag, Proc. and Inform.* 28, 25-37.
- De Bruin, H. A. R. (1987). "From Penman to Makkink", in J. C. Hooghart (Ed.), *Evaporation and Weather*, (Technical Meeting of the Committee for Hydrological Research, February, 1981), *Comm. Hydrol. Res. TNO, Den Haag, Proc. and Inform.* 39, 5-30.
- Eaton, A.K., Rouse, W.R., Lafleur, P.M., Marsh P., and Blanken, P.D. (2001). "Surface energy balance of the Western and Central Canadian Sub arctic: Variations in the energy balance among five major terrain types." *J. Climate* 14, 3692-3703.
- Flint, A.L. and Childs, S.W. (1991). "Use of the Priestley–Taylor evaporation equation for soil water limited conditions in a small forest clearcut." *Agric. For. Meteorol.* 56, 247–260.
- Garcia, M., Raes D., Allen R. and Herbas C. (2004). "Dynamics of reference evapotranspiration in the Bolivian highlands (Altiplano)." *Agric. Forest Meteorol.* 125, 67–82.
- Gavilàn, P., Berengena, J. and Allen R.G. (2007). "Measuring versus estimating net radiation and soil heat flux: Impact on Penman-Monteith reference ET estimates in semiarid regions." *Agric. Water Manage.* 89 (3), 275-286.
- Gavin, H. and Agnew, C.A. (2004). "Modelling actual, reference and equilibrium evaporation from a temperate wet grassland." *Hydrol. Processes* 18, 229–246.
- Hansen, S. (1984). Estimation of potential and actual evapotranspiration. *Nordic Hydrology* 15, 205–212.
- Irmak, S., Allen, R.G. and Whitty, E.B. (2003a). "Daily grass and alfalfa-reference evapotranspiration estimates and alfalfa-to-grass evapotranspiration ratios in Florida." *J. Irrig. Drain. Eng.* 129 (5), 360-370.

Irmak, S., Irmak, A., Allen, R. G. and Jones, J.W. (2003b). "Solar and net radiation-based equations to estimate reference evapotranspiration in humid climates." *J. Irrig. Drain. Eng.* 129 (5), 336–347.

Jensen, M. E., Burman, R. D. and Allen, R. G. (ed). (1990). "Evapotranspiration and Irrigation Water Requirements. ASCE Manuals and Reports on Engineering Practices No. 70." *Am. Soc. Civil Engrs.*, New York, NY, 360 pp.

Jiang, L., Islam, S. (2001). Estimation of surface evaporation map over southern Great Plains using remote sensing data. *Water Resour. Res.*, 37, 329-340.

Kustas, W.P., Stannard, D.I. and Allwine, K.J. (1996). "Variability in surface energy flux partitioning during Washita '92: resulting effects on Penman–Monteith and Priestley–Taylor parameters." *Agric. Forest Meteorol.* 82, 171–193.

López-Urrea, R., Martín de Santa Olalla, F., Fabeiro, C. and Moratalla, A. (2006). "An evaluation of two hourly reference evapotranspiration equations for semiarid conditions." *Agric. Water Manage.*, 86, 277-282.

Makkink, G.F. (1957). "Testing the Penman formula by means of lysimeters." *Journal of the Institution of Water Engineers* 11, 277–288.

New, M.G., Hulme M. and Jones P.D. (1999). "Representing 20th century space-time climate variability. I: Development of a 1961-1990 mean monthly terrestrial climatology." 12, 829-856.

NREL (1986). National Renewable Energy Laboratory. "Wind Energy Resource Atlas of the United States." Golden, Colorado
<http://rredc.nrel.gov/wind/pubs/atlas/atlas_index.html> (March 3, 2011).

UNEP (1992). United Nations Environment Programme, World Atlas of Desertification, Edward Arnold, London, UK.

USGS (2003). "United States Geological Survey, Hydrologic landscape regions of the United States." USGS Reston, Virginia,
<<http://water.usgs.gov/GIS/metadata/usgswrd/XML/hlrus.xml>> (March 3, 2011).

Peel, M.C., Finlayson, B.L. and McMahon T.A. (2007). "Updated world map of the Köppen-Geiger climate classification." *Hydrol. Earth Syst. Sci.*, 11, 1633-1644.

Penman, H.L. (1948). "Natural evaporation from open water, bare soil, and grass." *Proc. Roy. Soc. London* A193, 120-146.

- Pereira A.R. (2004). "The Priestley–Taylor parameter and the decoupling factor for estimating reference evapotranspiration." *Agric. Forest Meteorol.* 125, 305–313.
- Priestley, C.H.B. and Taylor, R.J. (1972). "On the assessment of surface heat flux and evaporation using large-scale parameters." *Mon. Weather Rev.* 100 (2), 81–92.
- Schramm, I., Boike J., Bolton W.R., and Hinzman L. (2007). "Application of TopoFlow, a spatially distributed hydrologic model to the Innvait Creek Watershed, Alaska." *Journal of Geophysical Research* 112:G04S46 doi:10.1029/2006JG000326.
- Smith, M., Allen, R. G., Monteith, J. L., Perrier, A., Pereira, L. and Segeren, A. (1991). "Report of the expert consultation on procedures for revision of FAO guidelines for prediction of crop water requirements." Rep., UN-FAO, Rome.
- Souch, C., Wolfe, C.P. and Grimmon, S.B. (1996). "Wetland evaporation and energy partitioning: Indian Dunes National Lakeshore." *J. Hydrol.* 184, 189–208.
- Soylu M.E., Istanbuluoglu E., Lenters, J.D. and Wang, T. (2011). "Quantifying the impact of groundwater depth on evapotranspiration in a semi-arid grassland region." *Hydrology and Earth System Sciences*, Vol. 15, No. 3, 787-806.
- Suleiman, A.A. and Hoogenboom, G. (2007). "Comparison of Priestley-Taylor and Penman-Monteith for daily reference evapotranspiration estimation in Georgia." *J. Irrig. Drain. Eng.* 133, 175-182.
- Tabari H and Hosseinzadeh Talae P. (2011). "Local calibration of the Hargreaves and Priestley–Taylor equations for estimating reference evapotranspiration in arid and cold climates of Iran based on the Penman-Monteith model." *Journal of Hydrologic Engineering*. DOI: 10.1061/(ASCE)HE.1943–5584.0000366.
- Wang, K., Li, Z., and Cribb, M. (2006). "Estimation of evaporative fraction from a combination of day and night land surface temperatures and NDVI: A new method to determine the Priestley-Taylor parameter." *Remote Sens. Environ.*, 102, 293-305.
- Wang X., Melesse A.M. and Yang W. (2006). "Influences of potential evapotranspiration estimation methods on SWAT's hydrologic simulation in a northwestern Minnesota watershed." *Trans. ASABE* 49 (6), 1755-1771.
- Willmott, C.J. (1982). "Some comments on the evaluation of model performance." *Bull. Am. Meteorol. Soc.*, 1309-1313.
- Yoder, R. E., Odhiambo, L. O. and Wright, W. C. (2005). "Evaluation of methods for estimating daily reference crop evapotranspiration at a site in the humid Southeast United States." *Appl. Eng. Agric.*, 21, 197–202.

Xiaoying, L. and Erda L. (2005). "Performance of the Priestley-Taylor equation in the semiarid climate of North China." *Agric. Water Manage.*, 71, 1-17.

Xing, Z., Chow, L., Meng, F., Rees, H.W., Monteith, J. and Lionel S. (2008). "Testing reference evapotranspiration estimation methods using evaporation pan and modeling in maritime region of Canada." *J. Irrig. Drain. Eng.*, 134, 417-424.

Xu, C.-Y. and Chen, D. (2005). "Comparison of seven models for estimation of evapotranspiration and groundwater recharge using lysimeter measurement data in Germany." *Hydrol. Processes* 19, 3717–3734.

Zhang, Y.Q., Liu, C.M., Yu Q., Shen, Y.J., Kendy, E., Kondoh, A., Tang, C.Y. and Sun, H.Y., (2004). "Energy fluxes and the Priestley-Taylor parameter over winter wheat and maize in the North China Plain." *Hydrol. Processes* 18, 2235–2246.

Appendix 2A

I) Online resources for hourly weather data:

1. Arizona Meteorological Network, AzMet (<http://ag.arizona.edu/AZMET/>)
2. California Irrigation Management Information System, CIMIS (<http://wwwcimis.water.ca.gov/cimis/welcome.jsp>),
3. Colorado Agricultural Meteorological Network, CoAgMet (<http://ccc.atmos.colostate.edu/~coagmet/>)
4. Florida Automated Weather Network (<http://fawn.ifas.ufl.edu/>)
5. Missouri Historical Agricultural Weather Database (<http://agebb.missouri.edu/weather/history/>)
6. North Dakota Agricultural Weather Network (<http://ndawn.ndsu.nodak.edu/>)
7. Pacific Northwest Cooperative Agricultural Weather Network, AgriMet (<http://www.usbr.gov/pn/agrimet/>).
8. Texas High Plains evapotranspiration network (<http://txhighplainset.tamu.edu/index.jsp>)
9. Washington State University Weather Network (<http://weather.wsu.edu/>)
10. Wisconsin and Minnesota Cooperative Extension Agricultural Weather network (<http://www.soils.wisc.edu/wimnext/index.html>),

II) Online resources for the spatial datasets of relative humidity and wind data:

1. Relative humidity dataset: <http://www.sage.wisc.edu/atlas/index.php>
2. Wind power density class dataset: <http://www.nrel.gov/gis/wind.html>

All links were last accessed on March 3, 2011.

III) Updated Köppen-Geiger climate classification maps (Peel et al., 2007):

<http://people.eng.unimelb.edu.au/mpeel/koppen.html>
http://people.eng.unimelb.edu.au/mpeel/Koppen/North_America.jpg

IV) ArcGIS Priestley-Taylor and Makkink-Hansen revised coefficients for the continental US:

<https://catalyst.uw.edu/workspace/cristn/26054/166779>.

Appendix 2B

Table 2.B1. Test stations and their latitude and longitude, annual average temperature, T , relative humidity, RH, 2-m wind speed, U , solar radiation, R_s , and α and C values estimated with either station mean annual RH and U or with the coefficient maps in Figure 2.7c-d

Station	year	Lat	Long	Elevation [m]	T [°C]	RH [%]	U [$m \cdot s^{-1}$]	R_s [$W \cdot m^{-2}$]	$(\alpha)_{RH,U}^1$ [-]	$(C)_{RH,U}^2$ [-]	$(\alpha)_{VPD,U}^3$ [-]	$(C)_{VPD,U}^4$ [-]	α_{map}^5 [-]	C_{map}^6 [-]
Aberdeen, ID	2002	42.9	112.8	1341	6.5	64.7	2.9	164	1.45	0.81	1.35	0.77	1.6	0.87
Spring Green, WI	2003	43.2	89.9	220	7.9	73.4	2.2	159.6	1.27	0.74	1.18	0.70	1.39	0.80
Kettle Butte, ID	2006	43.5	112.3	1565	6.8	63.9	3.2	154	1.49	0.83	1.40	0.79	1.60	0.87
Montevieu, ID	2005	44.0	112.5	1480	5	69.4	2.0	153.8	1.31	0.75	1.20	0.70	1.65	0.89
Rolla, ND	2006	48.8	99.6	552	4.8	74.4	3.9	157.2	1.39	0.8	1.37	0.79	1.36	0.80
Grand Forks, ND	2002	47.8	97.1	257	5.3	75.4	3.5	145.7	1.34	0.78	1.31	0.76	1.40	0.81
Fingal, ND	2002	46.8	97.8	438	5.2	76.5	4.4	149.7	1.39	0.81	1.42	0.82	1.42	0.82
Linneus, MO	2003	39.8	93.1	246	11.5	70.3	3.1	175.1	1.38	0.79	1.36	0.78	1.41	0.80
Oasis, CA	2002	33.5	116.2	4	22.7	46.7	2.2	233.6	1.67	0.88	1.76	0.92	1.64	0.86
Charleston, MO	2004	36.9	89.3	98	14.5	74.8	2.7	173.2	1.29	0.75	1.28	0.74	1.28	0.74
Temecula East II, CA	2003	33.5	117.0	468	16.1	65.1	1.8	212.6	1.36	0.77	1.37	0.77	1.39	0.77
Dixon, CA	2004	38.4	121.8	37	14.5	74.0	3.3	207.7	1.34	0.78	1.45	0.82	1.50	0.84
Puyallup, WA	2003	47.2	122.3	60	11.3	79.1	1.1	138.7	1.09	0.66	1.03	0.63	1.24	0.72
Wenatchee, WA	2008	47.4	120.3	237	9.96	64.3	1.3	168.5	1.33	0.75	1.20	0.70	1.51	0.84
Grand Junction, CO	2005	39.2	108.6	1484	11.3	50.9	1.9	194.8	1.59	0.85	1.41	0.78	1.60	0.85
Dove Creek, CO	2006	37.7	108.9	2010	9.1	50.3	3.0	220.9	1.68	0.89	1.43	0.80	1.68	0.87
Wapato, WA	2009	46.4	120.5	252	10.3	68.3	1.4	181.3	1.28	0.73	1.20	0.70	1.45	0.79
PK McClenny, WA	2009	46.4	118.8	168	10.5	66.2	2.4	177.5	1.39	0.79	1.33	0.76	1.60	0.87
South Tonasket, WA	2009	48.7	119.5	351	9.42	61.1	1.2	160.8	1.37	0.76	1.23	0.71	1.30	0.74
Walla Walla, WA	2009	46.1	118.3	353	11.1	64.4	1.7	162.2	1.37	0.77	1.26	0.72	1.45	0.79
Idalia, CO	2006	39.7	102.1	1212	10.8	60.73	3.5	191.3	1.561	0.86	1.51	0.84	1.66	0.90
Fort Collins, CO	2003	40.6	105.13	1561	9.6	61.96	1.9	158.4	1.422	0.79	1.27	0.73	1.51	0.81

¹ $(\alpha)_{RH,U}$ is the PT coefficient predicted using Eq. 7 and station RH and U as independent variables.

² $(C)_{RH,U}$ is the MK-Ha coefficient predicted using Eq. 7 and station RH and U as independent variables.

³ $(\alpha)_{VPD,U}$ is the PT coefficient predicted using Eq. 7 and station VPD and U as independent variables.

⁴ $(C)_{VPD,U}$ is the MK-Ha coefficient predicted using Eq. 7 and station VPD and U as independent variables.

⁵ α_{map} is the PT coefficient read at the site location from Figure 7c.

⁶ C_{map} is the MK-Ha coefficient read at the site location from Figure 7d.

Chapter 3. Linear models for estimating annual and growing season reference evapotranspiration using averages of weather variables

Abstract

We develop linear regression equations to estimate location specific average annual reference evapotranspiration (ET_o) using one or more of annual averages of: incoming solar radiation (R_s), air temperature (T), relative humidity (RH), and wind speed (U). We also provide two sets of equations to estimate growing season ET_o , either using one or more of annual averages of R_s , T, RH and U, or using growing season averages of the same variables. The equations are developed using the FAO-56 Penman Monteith model ET_o estimates as a reference. Supporting weather data to develop the regression equations were from 102 locations (494 station-years) across the contiguous United States (US). The models were tested with additional data from 32 stations (114 station-years). To illustrate potential applications of the regression models, we estimate spatial patterns of annual ET_o and growing season ET_o across the contiguous US using existing spatial datasets of annual averages of R_s , T, RH, and U. Other applications of the models provided may include rapid assessments of historical annual and growing season ET_o , evaluation of past ET_o trends, or evaluation of ET_o projected trends based on output from global climate models.

3.1. Introduction

Evaluation of evapotranspiration, broadly defined as the amount of water evaporating from soil and transpired through plants, is important for hydrologic modeling, agricultural water planning, and water budget and climate assessments. The Food and Agriculture Organization of the United Nations Irrigation and Drainage Paper 56 (Allen *et al.*, 1998) defines reference evapotranspiration, ET_o , as the evapotranspiration from a reference surface, termed as a “hypothetical grass reference crop with an assumed crop height of 0.12 m, a fixed surface resistance of 70 s m^{-1} and an albedo of 0.23”, which “closely resembles an extensive surface of green, well-watered grass of uniform height, actively growing and completely shading the ground”. The computed reference evapotranspiration can be used to calculate actual evapotranspiration for particular vegetation types and soil conditions and facilitates the selection and transferability of crop coefficients (Irmak and Haman, 2003).

The FAO-56 paper provides guidance to estimate ET_o from standard meteorological measurements of air temperature (T), relative humidity (RH), wind speed at 2-m height (U), and incoming solar radiation (R_s), based on the Penman-Monteith model (Allen *et al.*, 1998). This version of the Penman-Monteith method, referred to as FAO-56 PM, was shown to perform well against ET_o measurements across a range of climates (e. g. Garcia *et al.*, 2004; Yoder *et al.*, 2005a, Lòpez-Urrea *et al.*, 2006; Gavilà *et al.*, 2007; Benli *et al.*, 2010). Due to limitations in availability of observed ET_o datasets, the FAO-56 PM model has been used extensively to calculate ET_o in model inter-comparison studies (Irmak, 2003a, Suleiman and Hoogenboom, 2007, Trajkovic and Kolakovic, 2009) or as the basis for developing ET_o models that require fewer variables than FAO-56 PM (e.g. Irmak *et al.*, 2003b).

A sensitivity analysis study designed to evaluate the relative influences of weather variables on ET_o in the Southeast region of China showed that ET_o was most sensitive to changes in RH, followed by R_s , T, and U (Gong *et al.*, 2006). Similar results were obtained by Irmak *et al.* (2006) for a range of climate conditions in the United States (US). They showed that ET_o was most sensitive to vapor pressure deficit at all stations, followed by U in semiarid areas. Solar radiation, R_s , was the main driver at humid locations. Using factor analysis, Nanadagiri and Koor (2006) also indicated that U is important in arid climates, while sunshine hours are important for humid and sub-humid climates.

Predictions of ET_o rates are central to many planning applications in water resources and agriculture. Large changes in irrigation water demand are expected for many parts of the world, yet relatively little work has been done on estimating past or future evapotranspiration trends (Bates *et al.*, 2008). For many applications, complex reconstructions of ET_o rates are infeasible, and it is common for planners to rely on temperature-based ET equations since these equations are relatively simple to apply, and temperature data are more widely available than other meteorological variables (Xu

and Singh, 2001). Because ET_o is sensitive to a range of different variables depending on the region of application, a temperature-based calculation method can introduce biased ET_o estimates. We therefore propose an alternate method of ET_o prediction using regression equations. This approach maintains the structural simplicity and minimal data requirements needed for many practical applications but also accounts for the key variables that affect ET_o in different climates. The linear models provided here to calculate annual and seasonal ET_o can be used for location-specific or for regional scale evaluations of annual and seasonal ET_o , for analyzing ET_o in the past and for projected future trends, and for estimations of ET_o in areas where no meteorological measurements are available. The models have the advantage of a simple structure enabling them to be used with existing weather datasets or with generated datasets from climate models.

While regression-based models to predict evapotranspiration from weather variables have been previously employed at the daily time scale (e.g. Irmak *et al.*, 2003b, Kooor and Nandagiri, 2007), they have not yet been developed for annual or seasonal time scales. Thus, in this paper we: i) investigate the relationships between the controlling weather variables R_s , T , RH , and U and annual and seasonal ET_o and, ii) provide linear functional forms to estimate annual ET_o from annual averages of R_s , T , RH , and U and to estimate growing season ET_o either from annual averages of R_s , T , RH , and U , or from growing season averages of R_s , T , RH , and U . We also provide similar equations for the three-month peak growing season (Appendix C). As an example of the applicability of the various models we generate maps of annual and growing season ET_o for the contiguous US using existing spatial datasets of average R_s and T (Thornton *et al.*, 1997, Thornton *et al.*, 1999, Thornton *et al.*, 2000), RH (New *et al.*, 1999), and U (NREL, 1986).

3.2. Data and methods

We use weather data from 102 stations across the contiguous United States that recorded hourly weather data at agricultural network sites for a range of climate conditions. Data resources are listed in Appendix A. Weather data were retrieved from agricultural weather stations; these sites were selected because the agricultural monitoring stations are placed in locations with land cover conditions suitable for calculating reference crop evapotranspiration. These types of site conditions, as well as high data quality, are important for the accuracy of ET_o estimations (Irmak *et al.*, 2003b, Irfisu *et al.*, 2003). Weather station locations are shown as circles in Figure 3.1, which is the evapotranspiration map estimated by the United States Geological Survey (USGS) using mean monthly temperature and latitude and the Hamon (Hamon, 1961) equation (USGS, 2003).

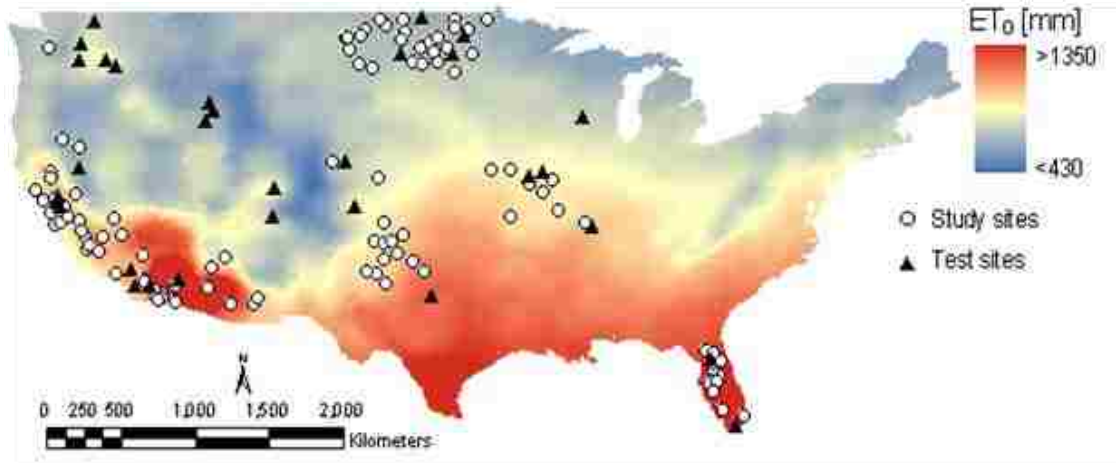


Figure 3.1. Study and test station locations shown on a map of ET calculated with the Hamon (1961) equation (USGS, 2003).

The selected weather stations have at least 3 years of consistent hourly records of R_s , T , RH , and U for a total of 494 station-years. Five years were used at 91 stations, 4 at 9 stations, and 3 at 1 station. We checked the datasets for quality and continuity using guidelines from Allen *et al.* (1998). Less than 5% of the total dataset had missing records, but for any missing periods, we followed the fill-in procedures detailed in Allen *et al.* (1998). In addition to our tests, most of the datasets used were checked for quality and integrity before they were made publicly available. For example, the data from the CIMIS network (32 stations in our dataset) were quality checked before being used to estimate ET_o in several studies (e. g. Irmak *et al.*, 2005).

Stations located in the western US experience the largest climate variability, with conditions ranging from arid desert and steppe to temperate and cold. The remaining stations cover four major climate types in the central and eastern US. The central region is characterized by arid steppe-cold, whereas the eastern half experiences a cold climate in the north and center, and the south experiences a temperate climate. Some stations located in the Southeastern region of the US (Florida) experience tropical influences. The 102 sites include locations in the most common climate types and sub-types of the contiguous US, according to the updated Köppen-Geiger climate classification map of Peel *et al.* (2007). Climate descriptions are based on Peel *et al.* (2007), where additional details are provided about climate classification, climate sub-types and variability across North America.

We calculate the average annual and growing season ET_o for the 494 station-years as sums of hourly ET_o rates estimated with the FAO-56 PM model equation given in Appendix B. The length of the growing season varies between climates, but for consistency we use the period of April 1 to September 30 at all locations. We use an

hourly time step to account for non-linearities associated with changes in T, RH, and U over the course of the day (Irmak *et al.*, 2005).

Based on the FAO-56 ET_o results, we then develop regression relationships to estimate the annual and growing season ET_o directly from annual averages of R_s , T, RH, and U. Additionally, for the growing season ET_o , we use growing season averages of R_s , T, RH, and U as predictors; details are provided in Section 3. In this procedure, the same weather variables that are used to calculate hourly ET_o with the FAO-56 PM equation are also used as predictor variables for regression models of annual and growing season ET_o . The FAO-56 PM equation was designed to work best for sub-daily to daily time scales, so we use the regression models to determine the time-integrated effect of these weather variables on ET_o predictions. The variables are employed in a different model structure (linear) and on much coarser timescales than those for PM calculations where data are averaged over hourly to daily, and at a maximum, one month, time steps.

We use multiple linear regressions to derive linear models to estimate average annual and growing season ET_o , with the generic equations:

$$ET_o = b_1 + b_2 \cdot R_s + b_3 \cdot T + b_4 \cdot RH + b_5 \cdot U \quad (3.1)$$

$$(ET_o)_{gs} = b_1 + b_2 \cdot R_s + b_3 \cdot T + b_4 \cdot RH + b_5 \cdot U \quad (3.2)$$

$$(ET_o)_{gs} = b_1 + b_2 \cdot (R_s)_{gs} + b_3 \cdot (T)_{gs} + b_4 \cdot (RH)_{gs} + b_5 \cdot (U)_{gs}, \quad (3.3)$$

where ET_o , and $(ET_o)_{gs}$, are the annual and growing season reference evapotranspiration [mm], respectively; R_s and $(R_s)_{gs}$ are the annual and growing season averages of direct solar radiation [$W \cdot m^{-2}$]; T and T_{gs} are the annual and growing season averages temperature [$^{\circ}C$]; RH and $(RH)_{gs}$ are the annual and growing season averages relative humidity [%], and U and $(U)_{gs}$ are the annual and growing season average wind speeds [$m \cdot s^{-1}$]. Additional equations are developed for the period June-July-August (JJA) and the results are provided in Appendix C in Table C1. The additional JJA ET_o equations are provided for estimating summer peak ET_o .

We start with one predictor, R_s , and sequentially add the rest of predictors with a prior test of significance in the regression. The order of adding variables to the regression is chosen based on both their correlation strength with ET_o and our estimated likelihood of either calculating or obtaining the necessary weather data, particularly in data scarce situations. Air temperature, T, is generally the most commonly measured weather variable. If not measured, solar radiation, R_s , can be calculated, and RH can be approximated using T but not reliably at all sites (Allen *et al.*, 1998). For wind speed, averages from regional climate are recommended, or a value of $2 m \cdot s^{-1}$ where no data are available (Allen *et al.*, 1998). Given these criteria, the variables are added in the following order: R_s , T, RH and U.

We test each regression model's prediction accuracy with weather data from 32 stations, shown as solid triangles in Figure 3.1, and multiple years, for a total of 114 station-years. Test stations are located both in and outside the study regions (Figure 3.1) and include climates varying from tropical in southern Florida, to cold (with high winds) in North Dakota, temperate in the center US, and arid in Southern California. Using the relationships found, we generate annual ET_o and growing season ET_o maps for the contiguous US using existing spatial datasets of annual averages of R_s and T (Thornton *et al.*, 1997, Thornton *et al.*, 1999, Thornton *et al.*, 2000), RH (New *et al.*, 1999), and U (NREL, 1986).

Spatial patterns of annual averages of R_s and T are from the Daymet US database (Thornton *et al.*, 1997, Thornton *et al.*, 1999, Thornton *et al.*, 2000). The RH dataset is from New *et al.* (1999) and the annual average U map was derived from the National Renewable Energy Laboratory (NREL) wind power density class dataset (NREL, 1986). In the NREL dataset each class is assigned a variation interval for wind speed at 10-m height, U_{10} . We estimate the spatial distribution of U (at 2-m height) assuming U_{10} as the mean value for the class and converting U_{10} to U using the wind conversion formula (equation 1.63) from Allen *et al.*, 1994. Data resources for the spatial datasets are listed in Appendix A.

3.3. Results

3.3.1. Multiple regression relationships

All variables, in all equations in Table 3.1, passed the test of significance in the regression at a p-value of 0.05. Table 3.1 lists the coefficient of determination R^2 , the regression coefficients found for each relationship and their corresponding 95% confidence intervals. Goodness of fit (Table 3.1) is quantified for both study and test sites using the standard error of the estimate:

$$SEE = \left[(N - 1)^{-1} \sum_i^N (ET_{o,pi} - ET_{o,i})^2 \right]^{0.5}, \quad (3.4)$$

where $ET_{o,pi}$ is the predicted annual (or growing season) ET_o with each regression equation, $ET_{o,i}$ is the annual (or growing season) ET_o calculated with the FAO-56 PM model, and i is the station index.

Table 3.1 Regression relationships, regression coefficients, 95% confidence intervals, the coefficient of determination (R^2) and *SEE* at study and test sites. Models i-iv are for annual ET_o , and models v-xii are for the growing season ET_o .

Model no.	Regression relationship	Regression coefficients	95% confidence intervals	R^2	<i>SEE</i> study sites, mm	<i>SEE</i> test sites, mm
i	$ET_o (R_s)$	$b_1 = -875.1$	-952.2 - 798.1	0.86	132.7	122.7
		$b_2 = 11.0$	10.6 11.4			
ii	$ET_o (R_s, T)$	$b_1 = -702.0$	-798.0 -642.6	0.88	122.0	98.9
		$b_2 = 9.4$	8.9 9.9			
		$b_3 = 12.2$	9.7 14.8			
iii	$ET_o (R_s, T, RH)$	$b_1 = 962.9$	814.2 1111.5	0.94	83.3	73.6
		$b_2 = 4.6$	4.1 5.2			
		$b_3 = 19.1$	19.1 17.3			
		$b_4 = -13.2$	-14.3 - 12.1			
iv	$ET_o (R_s, T, RH, U)$	$b_1 = 458.7$	369.3 548.2	0.98	47.1	47.7
		$b_2 = 4.5$	4.2 4.8			
		$b_3 = 32.5$	31.2 33.8			
		$b_4 = -11.5$	-12.1 -10.9			
		$b_5 = 84.6$	79.4 89.7			
v	$ET_{ogs} (R_s)$	$b_1 = -374.9$	-433.7 -316.7	0.79	101.3	85.8
		$b_2 = 6.6$	6.4 6.9			
vi	$ET_{ogs} (R_s, T)$	$b_1 = -405.4$	-469.5 -341.2	0.79	100.8	86.6
		$b_2 = 6.9$	6.6 7.4			
		$b_3 = -2.4$	-4.5 -0.3			
vii	$ET_{ogs} (R_s, T, RH)$	$b_1 = 892.7$	761.3 1024.2	0.89	73.7	67.6
		$b_2 = 3.2$	2.8 3.8			
		$b_3 = 2.9$	1.3 4.5			
		$b_4 = -10.2$	-11.1 -9.2			
viii	$ET_{ogs} (R_s, T, RH, U)$	$b_1 = 572.1$	459.4 684.7	0.92	59.3	59.4
		$b_2 = 3.2$	2.8 3.6			
		$b_3 = 11.4$	9.7 13.1			
		$b_4 = -9.1$	-9.9 -8.3			
		$b_5 = 53.8$	47.3 60.2			
ix	$ET_{ogs} (R_s)_{gs}$	$b_1 = -555.0$	-631.5 -478.5	0.74	112.4	102.9
		$b_2 = 5.7$	5.4 5.9			
x	$ET_{ogs} (R_s, T)_{gs}$	$b_1 = -633.6$	-693.3 -573.8	0.84	86.8	74.4
		$b_2 = 4.5$	4.3 4.8			
		$b_3 = 18.3$	16.3 20.2			
xi	$ET_{ogs} (R_s, T, RH)_{gs}$	$b_1 = 498.7$	398.7 598.8	0.93	58.6	57.7
		$b_2 = 2.2$	1.9 2.4			
		$b_3 = 17.2$	15.8 18.5			
		$b_4 = -8.1$	-8.8 -7.5			
xii	$ET_{ogs} (R_s, T, RH, U)_{gs}$	$b_1 = -5.2$	-74.9 64.4	0.97	35.6	29.0
		$b_2 = 2.7$	2.5 2.8			
		$b_3 = 22.9$	22.0 23.8			
		$b_4 = -6.1$	-6.5 -5.7			
		$b_5 = 48.2$	45.0 51.5			

In our dataset, the strongest inter-predictor correlations are between growing season R_s and RH, and annual R_s and RH, respectively (Table 3.2). Temperature T correlations with R_s and U are stronger at the annual scale and weaker at the growing season scale. The relationship between RH and T is relatively weak at both time scales, and the correlation between RH and U is negligible (Table 3.2). The distributions of the model residuals are approximately normal (Figure 3.2). Model accuracy increases with the increasing number of predictors. Thus, the percentages of predictions falling within 10 % accuracy are the smallest in models i and ii (74%, 77%), models v and vi (64%, 64%) and models ix and x (61% and 70%), but increase in models iii (82%), vii (85%) and xi (91%), and are the highest in the four-variable models iv (97%), viii (88%) and xii (97%). The most accurate models are iv, vii, and xii, in which 80%, 60% and 82% of the predictions, respectively are within 5% accuracy.

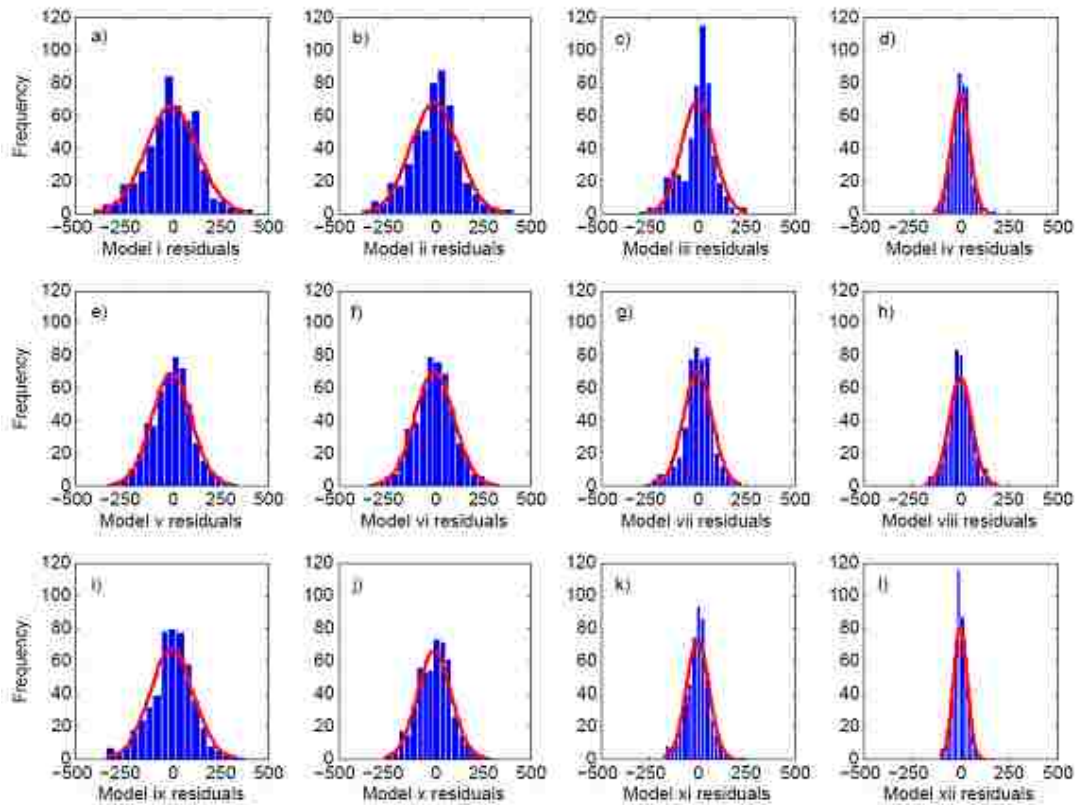


Figure 3.2 Histograms and fitted theoretical normal distributions of residuals in mm (a-l) for models i – xii, which are defined in Table 3.1.

Table 3.2 Correlation matrices between predictors: I) annual averages of R_s , T, RH and U and II) growing season averages of R_s , T, RH and U.

I	Annual				
		R_s	T	RH	U
	R_s	1.00	0.68	-0.77	-0.36
	T	0.68	1.00	-0.38	-0.69
	RH	-0.77	-0.38	1.00	0.08
U	-0.36	-0.69	0.08	1.00	
II	Growing season				
		$(R_s)_{gs}$	$(T)_{gs}$	$(RH)_{gs}$	$(U)_{gs}$
	$(R_s)_{gs}$	1.00	0.46	-0.79	-0.15
	$(T)_{gs}$	0.46	1.00	-0.40	-0.42
	$(RH)_{gs}$	-0.79	-0.40	1.00	-0.03
	$(U)_{gs}$	-0.15	-0.42	-0.03	1.00

Because we use weather variables, it is expected that collinearity between predictors exists. We evaluate the variance inflation factors (VIFs), as a measure to detect collinearity for all variables simultaneously, as the diagonal elements of the inverse of the sample correlation matrix. In our datasets, individual VIFs do not exceed 5 (the largest was 4.4) in any of the combinations shown in Table 1.

Figure 3.3 displays annual and growing season FAO-56 PM ET_o linear relationships with each predictor. Linear models appear to be suitable in columns one and three. Linear relationships are not valid in columns two and four, as evidenced by heteroscedasticity of the residuals about the fitted lines. While at the annual scale, R_s has the strongest correlation with ET_o , followed by RH and T (Figure 3.3, first row), at the growing season scale, the correlation between R_s and ET_o decreases compared with the annual scale, and the correlation between RH and ET_o increases (Figure 3.3, third row).

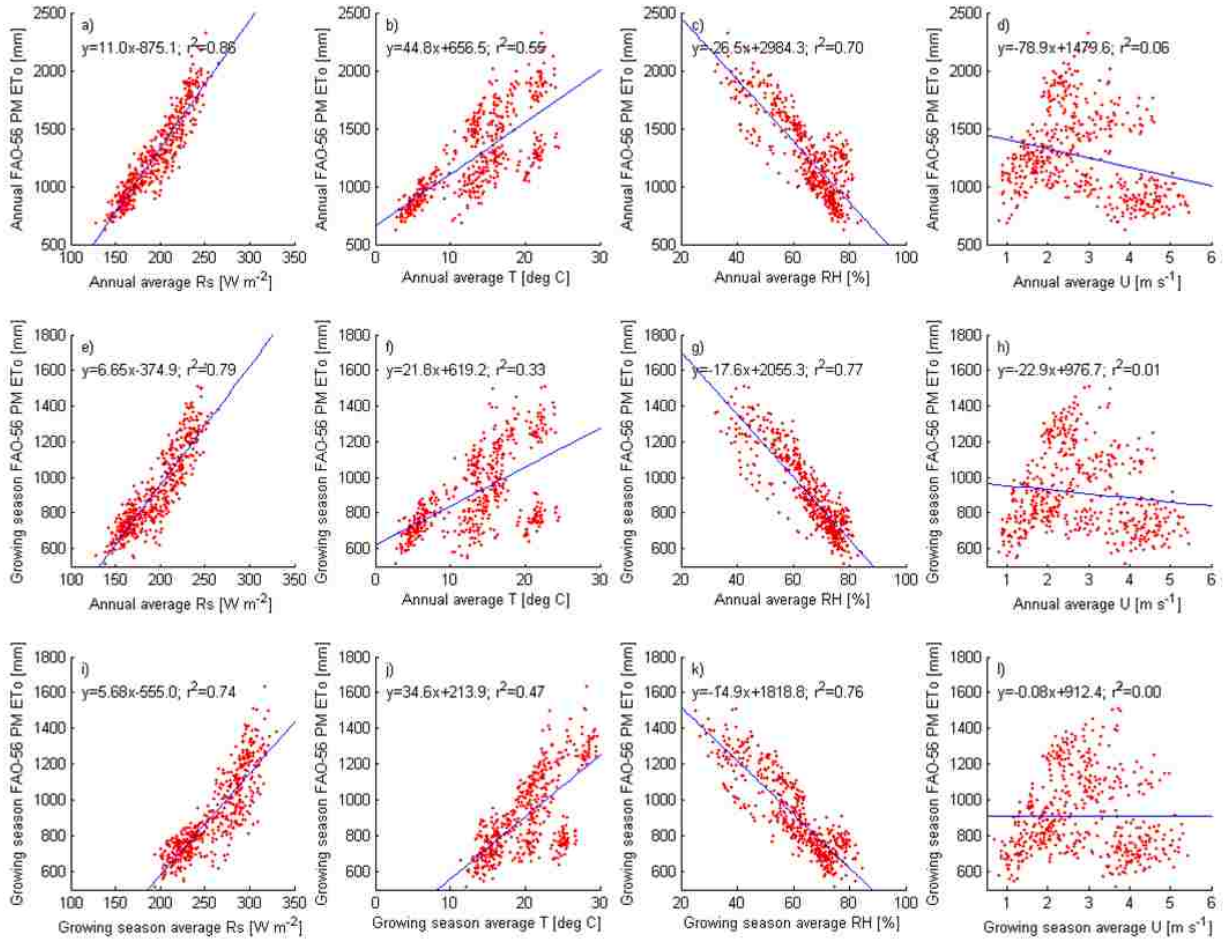


Figure 3.3 Correlations of the annual (a-d) and growing season ET_o (e-l) with each individual predictor.

3.3.2. Test results

We test the equations developed in Table 1 on independent weather datasets from 32 stations (shown as solid triangles in Figure 3.1) and 114 station-years of data. Table 1 indicates that the best performing models in terms of the smallest standard error of estimate (*SEE*) have four variables: equations iv; viii; and xii, for which the percentages of explained variance range between 92 and 98, and the *SEE* at the test stations are relatively small (Table 1). The ranges of *r*, defined as the ratios between the calculated FAO-56 PM ET_o and the predicted ET_o with the linear models i-xii from Table 1, are shown as box-and-whisker plots in Figure 3.4. For models iv and xii, most of the *r* values are within the 0.95-1.05 interval (Figure 3.4). Similar results were obtained for the JJA period (Figures not shown), where the JJA averages of R_s, T, RH and U are more effective predictors than the annual averages (Appendix C). For the JJA period, R_s and (R_s)_{JJA} are weaker single predictors compared with the corresponding models for the annual and growing season periods. However, the addition of the JJA average T first, and then RH

and U significantly increases R^2 and improves model performance for the JJA period (Appendix 3C).

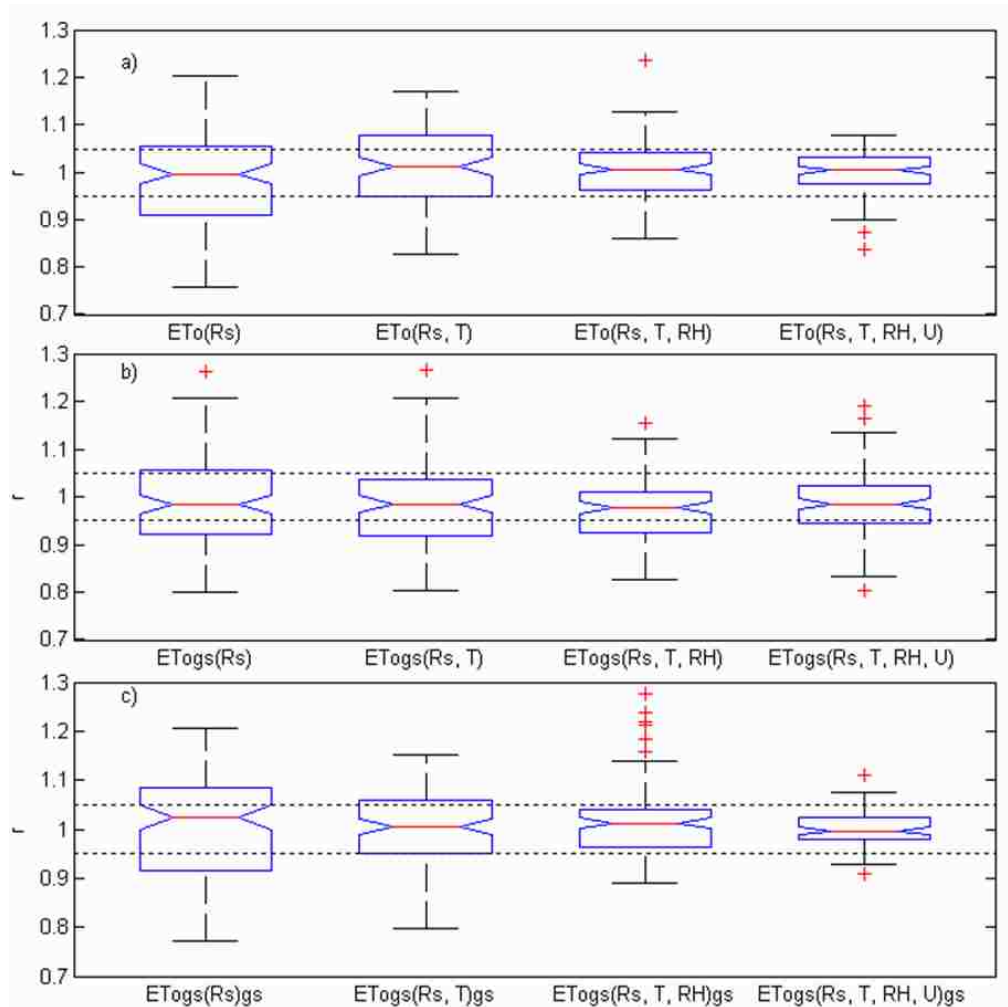


Figure 3.4 Box and whisker plots of the ratio r for models i-vi (a), models v – vii (b), and models ix – xii (c) at the test stations. Dotted lines correspond to $r = 0.95$ and $r = 1.05$.

Figure 3.5 shows scatterplots of the calculated ET_0 with the FAO-56 PM model and predicted ET_0 using the regression models. Measured incoming solar radiation R_s is a better predictor at the annual scale in the simplest, single variable models (Figure 3.5a), providing more accurate estimates at humid sites (lower evapotranspiration), than at drier and windier sites (higher evapotranspiration). The scatter around the one-to-one line decreases in all models with the sequential addition of predictor variables (Figure 3.5).

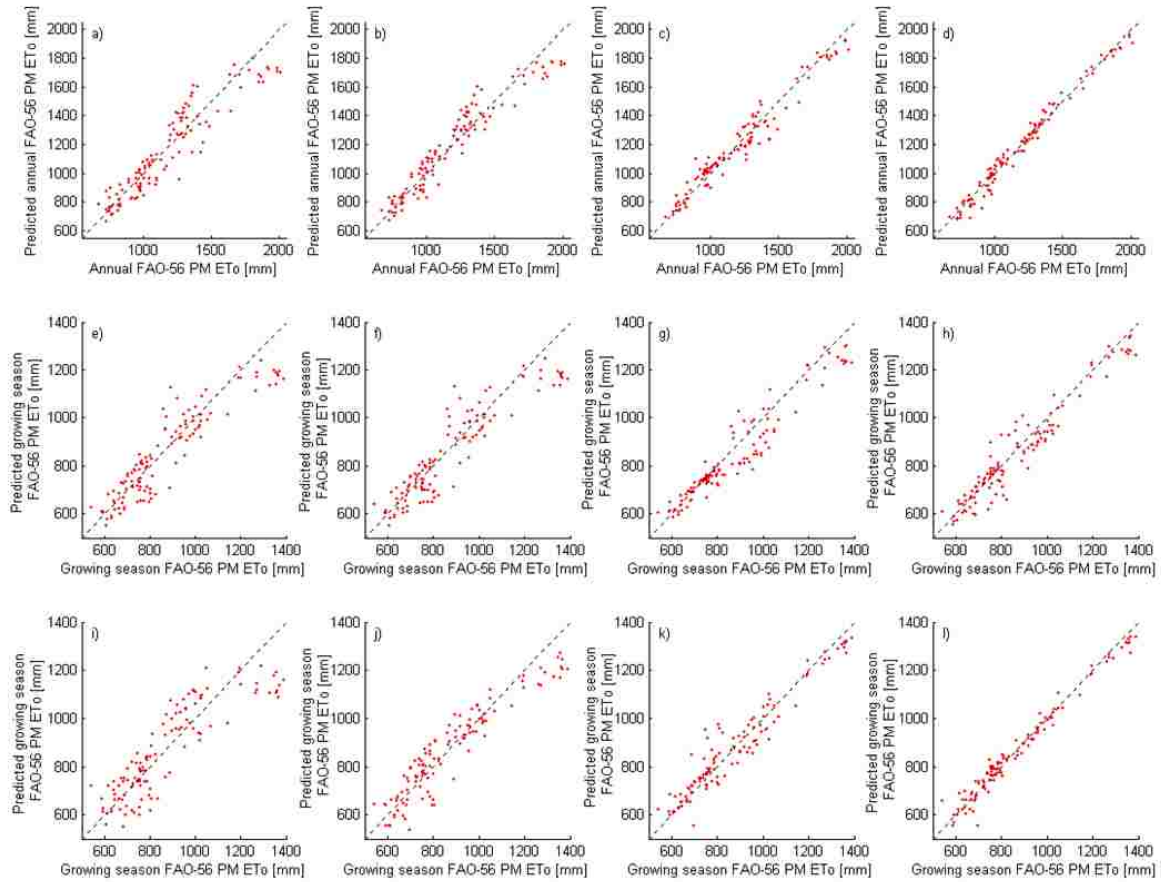


Figure 3.5 Scatterplots of the calculated FAO-56 PM ET_0 and predicted ET_0 with models i-vi (a-d), models v – viii (e-h) and models ix – xii (i-l) at the test stations. Dashed line shows the one-to-one relationship.

3.3.3. Example application

To generate spatial patterns of annual and growing season ET_0 for the contiguous US, we use models iii and iv for the annual ET_0 and models vii and viii for the growing season ET_0 (Table 1), with input variables taken from the spatial datasets previously described. The predictor variables in Figure 3.6a-d are: (a) Rs, (b) T, (c) RH, and (d) U. Figure 3.6e-f and g-h show the resulting spatial patterns of annual and growing season ET_0 estimated with models iii-iv and vii - viii, respectively. Figure 3.6i-j shows the relative differences between models iii and iv annual ET_0 (Figure 3.6g-h) and potential evapotranspiration estimated with the temperature-based Hamon (1961) model (USGS, 2003; Figure 3.1). The resolution in Figure 3.6 is 0.21 degree.

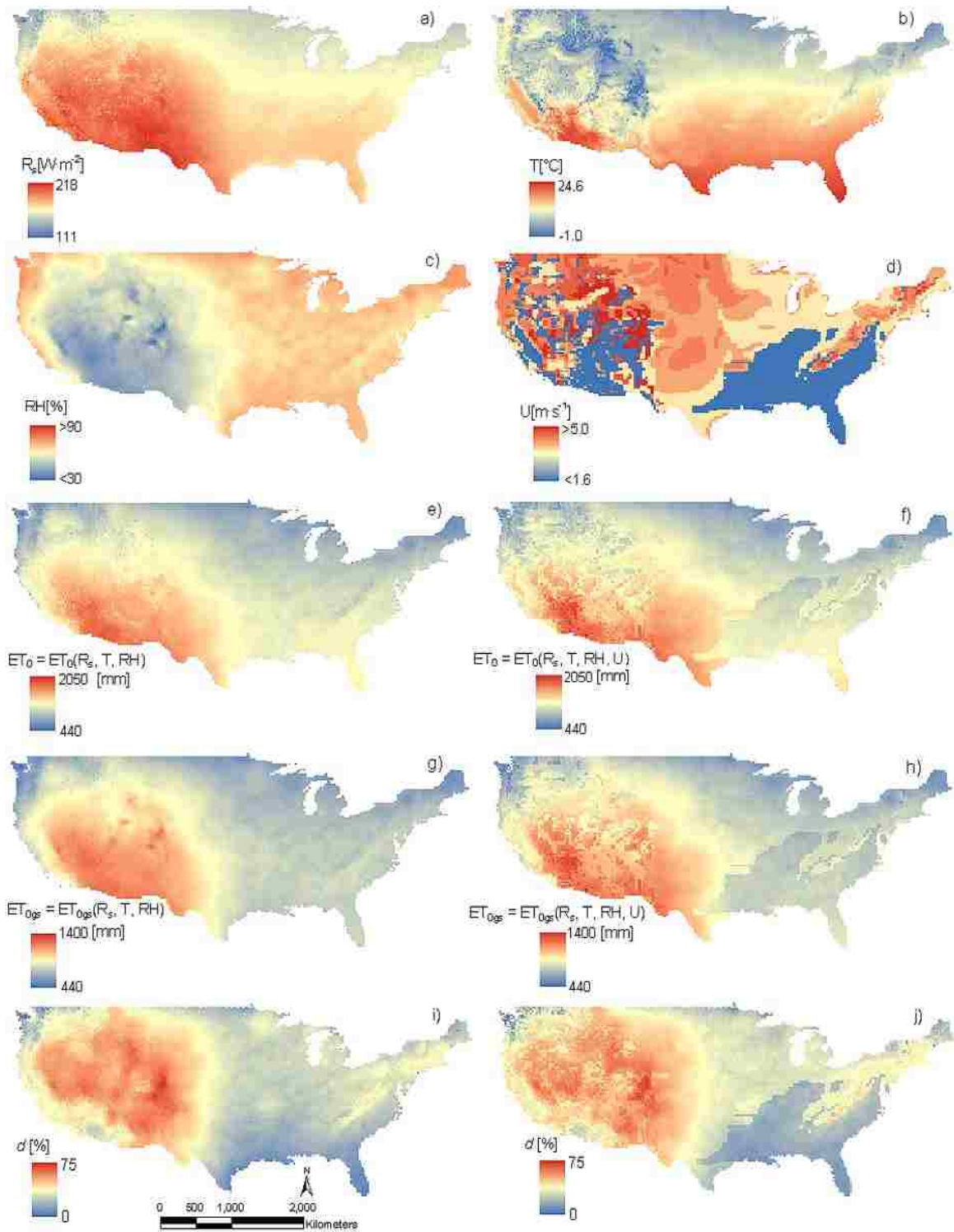


Figure 3.6. Spatial patterns of R_s (a), T (b), RH (c), U (d), annual ET_0 from model iii (e), annual ET_0 from model iv (f), growing season ET_0 from model vii (g), growing season ET_0 from model viii (h) and relative differences between ET_0 from models iii and iv and the ET_0 map of Figure 3.1 (i-j).

3.4. Discussion

Due to limited availability of lysimeter datasets to measure ET_o directly, we use the FAO-56 PM model with weather station measurements of hourly input data as a reference to develop the linear regression ET_o models listed in Table 1. Uncertainties in the FAO-56 PM ET_o estimates primarily relate to the model itself and to the accuracy of the input data. The FAO-56 PM is considered the most reliable and robust model to estimate ET_o at both dry and humid sites and has been recommended (Smith *et al.*, 1991) and used (e.g. Irmak *et al.*, 2003b) in prior research as a base to develop simpler ET_o models for data-limited locations. The FAO-56 PM ET_o equations require additional computational steps to estimate R_n (e.g. Allen *et al.*, 1998), which is not typically measured at the weather stations. The calculated ET_o may differ if measurements of R_n (Gavilàn *et al.*, 2007) or other R_n models are used (Yoder *et al.*, 2005b, Temesgen *et al.*, 2007), but Gavilàn *et al.* (2007) showed that the calculated R_n with the FAO-56 equations is accurate enough to be used as replacement for measured R_n in ET_o calculations. Additional uncertainty in the FAO-56 PM model is related to how the soil heat flux density G is represented (Irmak *et al.*, 2005), which may not be appropriate at all sites and is subject to measurement errors or undetected inconsistencies in the input data.

In the process of developing these regression-based ET_o models, we considered alternative regression techniques, based on principal components or partial least squares, but we ultimately opted for multiple linear regressions. The resulting models (Table 1) have a simple structure, do not require additional manipulations (transformations) of the input data, and rely on relatively few variables that do not lose interpretability. While regression-based models are most appropriate when applied using independent predictor variables, some degree of collinearity is inherent to our dataset, as, for example, incoming solar radiation influences air temperature and relative humidity.

If collinearity is significant, its effect increases the variances of the regression coefficients and reduces the stability of the model. Some studies have suggested a VIF threshold of 5 to indicate significant collinearity, whereas others suggest that VIFs larger than 10 indicate significant collinearity (Marquardt, 1970, Neter *et al.*, 1989, Hair *et al.*, 1995, Haan, 2002). O'Brien (2007) showed that a higher degree of collinearity (VIFs larger than 10 or 20, even higher than 40) is not necessarily harmful for model predictions. In our case, the largest VIFs were between 4 and 5, indicating that collinearity is present but not important. Tests on the independent dataset (Figure 3.5) show that the models are unbiased.

Figures 3.6e and 3.6g show that the predicted annual and growing season ET_o spatial patterns using 3-variable models iii and vii are similar to the spatial patterns of the dominant predictor, solar radiation R_s (Figure 3.6a). The addition of the fourth predictor, U , in models iv and viii improves the accuracy of predictions at the test sites compared with the 3-variable models (Figures 3.4 and 3.5) and increases the spatial variability in

the annual and growing season ET_o maps (Figures 3.6f and 3.6h). Uncertainties in all ET_o maps shown in Figures 3.6e-h are related to the accuracy of ET_o predictions by the linear models and to the R_s , T, RH, and U spatial datasets used, which are generally associated with the spatial coverage of the stations, periods of investigation and interpolation techniques.

The choice of the potential evapotranspiration model to represent annual average spatial variability at the global scale is important, as models available vary in underlying assumptions and input data requirements, resulting in differences in predictions for the non-growing season (Weiß and Menzel, 2008). In our case, all the annual and growing season ET_o maps shown in Figures 3.5e-h have spatial patterns similar to R_s (Figure 3.6a). This is different from how spatial variability of annual ET_o is represented in the USGS (2003) ET_o map (Figure 3.1), where ET_o , calculated based on the Hamon (1961) model has a spatial distribution similar to that of T (Figure 3.6b). Figure 3.6 i-j shows that the Hamon (1961) model produces ET_o estimations that are most similar to annual ET_o from models iii and iv in the humid, less windy (advective) region of the Southeastern United States, but it significantly underestimates ET_o in the drier, higher solar radiation and windier regions located in the western half of the contiguous US.

The magnitudes of the estimated annual ET_o also vary between the Hamon (1961) equation (Figure 3.1) and the regression models (Figure 3.6e and f). The models we used are likely to have improved accuracy over the Hamon (1961) temperature-based estimates because they were developed using the FAO-56 PM model hourly ET_o estimates, which capture time variations in weather data and the effects of wind speed and relative humidity. Our results show that temperature is not as important as R_s and RH in predicting spatial patterns of ET_o . Further verification of these models comes from comparison with the map of average annual evaporation from shallow lakes (contour map) from Kohler *et al.* (1959). Annual ET_o maps generated with models iii and iv have similar spatial patterns to the shallow lake evaporation map.

The maps shown in Figure 3.6e-h are developed assuming potential conditions and are suitable for estimating agricultural water needs. Actual evapotranspiration can be much lower as a function of vegetation cover and local water and energy limitations (see e.g. Zhang *et al.*, 2010). The relationships found (Table 1) are based on data from the contiguous US weather stations and cover a relatively large range of climate conditions. Extrapolation beyond these conditions will require testing against location specific data. Further work could apply these regression models using other spatial datasets of climate variables such as the North America Land Data Assimilation System (NLDAS) or output of GCMs. The regression models can also be used as a reference to compare with ET estimates derived from land surface models or reanalysis products.

3.5. Summary and Conclusions

We estimated the annual and growing season (April-September) reference evapotranspiration ET_o , as the sum of hourly rates calculated with the FAO-56 Penman-Monteith (PM) model with weather data from 102 locations that include a wide range of common climate types across the contiguous US. At the annual scale, the calculated ET_o has the strongest correlations with annual average solar radiation, R_s , followed by the annual averages of relative humidity (RH) and air temperature (T). The growing season ET_o has strongest correlations with annual and growing season averages of R_s and RH, followed by the growing season and annual averages of T.

We developed linear regression-based models to predict annual average reference evapotranspiration ET_o using annual averages of R_s , T, RH, and two-meter elevation wind speed (U) as predictors. Models to predict growing season ET_o using either annual averages of R_s , T, RH, and U or growing season averages of R_s , T, RH, and U are also provided. Dormant season ET_o can be estimated by subtracting the growing season ET_o from the annual ET_o . All regression models have been developed starting with one predictor R_s , and adding the remaining predictors sequentially: T, RH, and U, in order, resulting in 1-, 2-, 3-, and 4-predictor models, for a total of 12 models. We used the FAO-56 PM model as a reference for model development in place of direct ET_o measurements. The relationships found were tested on an independent weather dataset from 32 stations.

The best performing models ($R^2 = 0.92$ to 0.98) overall have the 4- variables: R_s , T, RH, and U, followed by the 3-variable models that use R_s , T, and RH ($R^2 = 0.89$ to 0.94). For these models, the percentages of values within 10% accuracy range between 82% (model iii) and 97% (model iv), and for models iv and xii, 80 and 82% of the values fall within 5% accuracy. The simplest models based on one variable, solar radiation, are more efficient at humid sites, but the inclusion of all predictors is important for prediction accuracy at dry and windy sites. As an application example, we generated maps of the spatial patterns of annual and growing season ET_o across the contiguous US. The equations provided are simple, yet effective for predicting average annual and growing season ET_o .

3.6. References

Allen RG, Pereira LS, Raes D, Smith M. 1998. Crop evapotranspiration, guidelines for computing crop water requirements. *FAO Irrig. and Drain. Paper 56, Food and Agric. Orgn. of the United Nations, Rome, Italy.* 300 pp.

Allen RG, Smith M, Perier A., Pereira LS. 1994. An update for the definition and calculation of reference evapotranspiration. *ICID Bull.* **43**: 35–92.

Bates BC, Kundzewicz ZW, Wu S, Palutikof JP, eds. 2008. Climate change and water. Technical Paper of the Intergovernmental Panel on Climate Change. Geneva: IPCC Secretariat.

Benli B, Bruggeman A, Oweis T, Ustun H. 2010. Performance of Penman-Monteith FAO56 in a semiarid highland environment. *J. Irrig. Drain. Eng.* **136** (11): 757-765.

Garcia M, Raes D, Allen R, Herbas C. 2004. Dynamics of reference evapotranspiration in the Bolivian highlands (Altiplano). *Agric. Forest Meteorol.* **125**: 67–82.

Gavilàn P, Berengena, J, Allen RG. 2007. Measuring versus estimating net radiation and soil heat flux: Impact on Penman-Monteith reference ET estimates in semiarid regions. *Agric. Water Manage.* **89** (3), 275-286.

Gong L., Xu C, Chen D, Halldin S, Chen YD. 2006: Sensitivity of the Penman-Monteith reference evapotranspiration to key climatic variables in the Changjiang (Yangtze River) basin. *J. Hydrol.*, **329**: 620–629.

Haan, C.T. 2002. Statistical methods in hydrology, second edition. Iowa State University Press, Ames, Iowa.

Hair JF Jr., Anderson RE, Tatham RL, Black WC. 1995. *Multivariate Data Analysis*, 3rd edn. New York: Macmillan.

Hamon, WR.1961. Estimating potential evapotranspiration: *Proceedings of the American Society of Civil Engineers, Journal of the Hydraulics Division* **87**, no. HY3, p.107-120.

Irmak S, Allen RG, Whitty EB. 2003a. Daily grass and alfalfa-reference evapotranspiration estimates and alfalfa-to-grass evapotranspiration ratios in Florida. *J. Irrig. Drain. Eng.* **129** (5), 360-370.

Irmak, S., Haman, D. Z. 2003. Evapotranspiration: potential or reference? ABE 343. IFAS, Fla. Coop. Ext. Serv., Univ. of Florida, Gainesville.

Irmak S, Irmak A, Allen RG, Jones, JW. 2003b. Solar and net radiation-based equations to estimate reference evapotranspiration in humid climates. *J. Irrig. Drain. Eng.* **129** (5), 336–347.

Irmak S, Howell TA, Allen RG, Payero JO, Martin DL. 2005. Standardized ASCE-Penman-Monteith: Impact of sum-of-hourly vs. 24-hr-timestep computations at reference weather station sites. *Transactions of the ASAE* **48**(3):1063-1077.

Irmak S, Payero JO, Martin DL, Irmak A, Howell TA. 2006. Sensitivity analyses and sensitivity coefficients of the standardized ASCE-Penman-Monteith equation to climate variables. *J. Irrig. Drain. Eng.* **132**(6):564-578.

Itenfisu D, Elliott RL, Allen RG, Walter IA. 2003. Comparison of reference evapotranspiration calculations as part of the ASCE standardization effort. *J. Irrig. Drain. Eng.* **129**(6), 440–448.

Kohler MA, Nordenson TJ, Baker DR. 1959. Evaporation maps for the United States. *National Weather Service Technical Paper 37*.

Kovoor G, Nandagiri L. 2007. Development of regression models for predicting pan evaporation from climatic data – a comparison of multiple least-squares, principal components and partial least squares approaches. *J. Irrig. Drain. Eng.* **133** (5): 444-454.

López-Urrea R, Martín de Santa Olalla F, Fabeiro C, Moratalla A. 2006. An evaluation of two hourly reference evapotranspiration equations for semiarid conditions. *Agric. Water Manage.*, **86**: 277-282.

Marquardt DW. 1970. Generalized inverses, ridge regression, biased linear estimation, and nonlinear estimation. *Technometrics* **12**: 591–256.

Nandagiri L, Kovoor G. 2006. Performance Evaluation of reference evapotranspiration equations across a range of Indian climates. *J. Irrig. Drain. Eng.*, **132**: 238-249.

Neter J, Wasserman W, Kutner MH. 1989. *Applied Linear Regression Models*. Homewood.

New MG, Hulme M, Jones PD. 1999. Representing 20th century space-time climate variability. I: Development of a 1961-1990 mean monthly terrestrial climatology. *J. Climate*. **12**: 829-856.

NREL, 1986. National Renewable Energy Laboratory, Wind Energy Resource Atlas of the United States. Golden, Colorado
http://rredc.nrel.gov/wind/pubs/atlas/atlas_index.html. Link last accessed on March 3, 2011.

O'Brien RM. 2007. A Caution Regarding Rules of Thumb for Variance Inflation Factors. *Quality and Quantity* **41** (5): 673-690.

Peel MC, Finlayson BL, McMahon TA. 2007. Updated world map of the Köppen-Geiger climate classification. *Hydrol. Earth Syst. Sci.*, **11**: 1633-1644.

Smith M, Allen RG, Monteith JL, Perrier A, Pereira L, Seegeren A. 1991. Report of the expert consultation on procedures for revision of FAO guidelines for prediction of crop water requirements. Rep., UN-FAO, Rome.

Suleiman AA, Hoogenboom, G. 2007. Comparison of Priestley-Taylor and Penman-Monteith for daily reference evapotranspiration estimation in Georgia. *J. Irrig. Drain. Eng.* **133**: 175-182.

Temesgen B, Eching S, Frame K. 2007. Comparing net radiation estimation methods: CIMIS versus Penman–Monteith. *J. Irrig. Drain. Eng.* **133**: 265-271.

Thornton PE, Running, SW, White MA. 1997. Generating surfaces of daily meteorological variables over large regions of complex terrain. *Journal of Hydrology*, **190**: 214-251.

Thornton PE Running SW. 1999. An improved algorithm for estimating incident daily solar radiation from measurements of temperature, humidity, and precipitation. *Agricultural and Forest Meteorology* **93**: 211-228.

Thornton PE, Hasenauer, H, White MA. 2000. Simultaneous estimation of daily solar radiation and humidity from observed temperature and precipitation: an application over complex terrain in Austria. *Agricultural and Forest Meteorology* **104**: 255-271.

Trajkovic S, Kolakovic S. 2009. Evaluation of reference evapotranspiration equations under humid conditions. *Water Resour. Manage.* **23**: 3057-3067.

USGS, 2003. United States Geological Survey, Hydrologic landscape regions of the United States, USGS, Reston, Virginia, <http://water.usgs.gov/GIS/metadata/usgswrd/XML/hlrus.xml>. Link last accessed on March 3, 2011.

Xu C-Y. and Singh VP. 2001. Evaluation and generalization of radiation-based methods for calculating evaporation, *Hydrol. Processes* **15**: 305–319.

Yoder RE, Odhiambo LO, Wright WC. 2005a. Evaluation of methods for estimating daily reference crop evapotranspiration at a site in the humid Southeast United states. *Appl. Eng. Agric.* **21**: 197–202.

Yoder RE, Odhiambo, LO, Wright WC. 2005b. Effects of Vapor Pressure Deficit and Net-Irradiance Calculation Methods on the Accuracy of the Standardized Penman-Monteith Equation in a Humid Climate. *J. Irrig. Drain. Eng.* **131**(3):228-237.

Zhang K, Kimball JS, Nemani RR, Running SW. 2010. A continuous satellite-derived global record of land surface evapotranspiration from 1983 to 2006. *Water Resour. Res.* **46**: W09522, doi:10.1029/2009WR008800.

Weiß M, Menzel L. 2008. A global comparison of four potential evapotranspiration equations and their relevance to stream flow modelling in semi-arid environments. *Adv. Geosci.*,**18**: 15-23.

Appendix 3A

I) Hourly weather data sources:

1. Arizona Meteorological Network, AzMet (<http://ag.arizona.edu/AZMET/>)
2. California Irrigation Management Information System, CIMIS (<http://www.cimis.water.ca.gov/cimis/welcome.jsp>),
3. Colorado Agricultural Meteorological Network, CoAgMet (<http://ccc.atmos.colostate.edu/~coagmet/>)
4. Florida Automated Weather Network (<http://fawn.ifas.ufl.edu/>)
5. Missouri Historical Agricultural Weather Database (<http://agebb.missouri.edu/weather/history/>)
6. North Dakota Agricultural Weather Network (<http://ndawn.ndsu.nodak.edu/>)
7. Pacific Northwest Cooperative Agricultural Weather Network, AgriMet (<http://www.usbr.gov/pn/agrimet/>).
8. Texas High Plains evapotranspiration network (<http://txhighplainset.tamu.edu/index.jsp>)
9. Washington State University Weather Network (<http://weather.wsu.edu/>)
10. Wisconsin and Minnesota Cooperative Extension Agricultural Weather network (<http://www.soils.wisc.edu/wimnext/index.html>),

II) Spatial data sources:

1. Solar radiation and air temperature (1980-1997): <http://www.daymet.org/>
2. Relative humidity (1961-1990) <http://www.sage.wisc.edu/atlas/index.php>
3. Wind power density class dataset: <http://www.nrel.gov/gis/wind.html>

All links were last accessed on March 3, 2011.

Appendix 3B

Hourly FAO 56 Penman-Monteith

The hourly FAO-56 PM model (Allen *et al.*, 1998) used for calculating reference evapotranspiration ET_o is:

$$ET_o = \frac{0.408\Delta(R_n - G) + \gamma \frac{37}{T + 273} U(e_s(T) - e_a)}{\Delta + \gamma(1 + 0.34U)} \quad (B1),$$

where: ET_o = FAO-56 PM reference evapotranspiration [$mm\ h^{-1}$], R_n = calculated net radiation at the grass surface [$MJ\ m^{-2}\ h^{-1}$], G = soil heat flux density at the soil surface [$MJ\ m^{-2}\ h^{-1}$]; T = mean hourly air temperature at 2-m height [$^{\circ}C$]; U = mean hourly wind speed at 2-m height [$m\ s^{-1}$]; e_s = saturation vapor pressure at 2-m height [kPa]; e_a = mean hourly actual vapor pressure at 2-m height [kPa]; Δ = slope of the saturation vapor pressure curve at T [$kPa\ ^{\circ}C^{-1}$]; γ = psychrometric constant [$kPa\ ^{\circ}C^{-1}$]. Values of Δ , γ , R_n , G , e_s , and e_a and other supporting equations are calculated according to Allen *et al.* (1998), where complete details on ET_o model assumptions and equations are provided.

The saturation vapor pressure (e_s) is dependent on temperature (T), while the actual average hourly actual vapor pressure (e_a) is calculated based on e_s and the hourly relative humidity RH [%]:

$$e_s(T) = 0.6108 \exp\left(\frac{17.27T}{T + 237.3}\right) \quad (B2)$$

$$e_a = e_s(T) \frac{RH}{100} \quad (B3)$$

The slope of the saturation vapor pressure curve at temperature T , Δ , and the psychrometric constant, γ , are given by:

$$\Delta = \frac{4098 \left[0.6108 \exp\left(\frac{17.27T}{T + 237.3}\right) \right]}{(T + 237.3)^2} \quad (B4)$$

$$\gamma = \frac{c_p p}{\epsilon \lambda}, \quad (B5)$$

where: c_p is the specific heat at constant pressure, equal to $1.013 \cdot 10^{-3}$ [$MJ\ kg^{-1}\ ^{\circ}C^{-1}$] for average atmospheric conditions, λ is the latent heat of vaporization, equal to 2.45 [$MJ\ kg^{-1}$], ϵ is the ratio of molecular weight of water vapor/dry air = 0.622 , and p is the atmospheric pressure [kPa], calculated as a function of z , the elevation above the sea level [m]:

$$p = 101.3 \left(\frac{293 - 0.0065z}{293} \right)^{5.26} \quad (B6)$$

The hourly soil heat flux density (G) in equation B1 was estimated as $G = 0.1 \cdot R_n$ during daytime and $G = 0.5 \cdot R_n$ during nighttime, while the hourly net radiation (R_n) is calculated as the difference between the net shortwave radiation, R_{ns} [$MJ\ m^{-2}\ h^{-1}$], and the net longwave radiation, R_{nl} [$MJ\ m^{-2}\ h^{-1}$]:

$$R_n = R_{ns} - R_{nl}, \quad (B7)$$

in which the hourly net shortwave radiation R_{ns} is given by:

$$R_{ns} = (1 - \alpha) R_s, \quad (B8)$$

where α is the albedo, equal to 0.23 for grass, and R_s is the measured incoming solar radiation [$MJ\ m^{-2}\ h^{-1}$].

The hourly net longwave radiation R_{nl} was calculated as:

$$R_{nl} = \sigma T_{hr,K}^4 \left(0.34 - 0.14 \sqrt{e_a} \right) \left(1.35 \frac{R_s}{R_{so}} - 0.35 \right), \quad (B9)$$

with σ the Stefan-Boltzmann constant equal to $2.043 \cdot 10^{-10}$ [$\text{MJ m}^{-2} \text{h}^{-1}$], $T_{hr,K}$ the hourly mean temperature [K], and R_{so} [$\text{MJ m}^{-2} \text{h}^{-1}$] the clear sky radiation as calculated based on the station elevation z [m] and the extraterrestrial radiation R_a [$\text{MJ m}^{-2} \text{h}^{-1}$] as:

$$R_{so} = (0.75 + 2 \cdot 10^{-5} z) R_a, \text{ with} \quad (B10)$$

$$R_a = \frac{12(60)}{\pi} G_{sc} d_r [(\omega_2 - \omega_1) \sin(\phi) \sin(\delta) + \cos(\phi) \cos(\delta) (\sin(\omega_2) - \sin(\omega_1))] \quad (B11)$$

where: G_{sc} is the solar constant equal to 0.0820 [$\text{MJ m}^{-2} \text{min}^{-1}$], d_r is the inverse relative distance Earth-Sun:

$$d_r = 1 + 0.033 \cos\left(\frac{2\pi}{365} J\right), \quad (B12)$$

in which J is the (Julian) number of the day in the year, δ is the solar declination [rad]:

$$\delta = 0.409 \sin\left(\frac{2\pi}{365} J - 1.39\right), \quad (B13)$$

ϕ is the latitude [rad], ω_1 and ω_2 are the solar angles at the beginning and end of the period:

$$\omega_1 = \omega - \frac{\pi t_1}{24}, \quad \omega_2 = \omega + \frac{\pi t_1}{24}, \quad (B14)$$

where ω is the solar time angle at the midpoint of the hourly period [rad], and $t_1 = 1$ [h]. The solar angle ω is given by:

$$\omega = \frac{\pi}{12} [(t + 0.06667(L_z - L_m) + S_c) - 12], \quad (B15)$$

in which t is the standard clock time at the midpoint of the period [h], L_z is the longitude of the centre of the local time zone [degrees west of Greenwich], equal to $75, 90, 105$ and 120° for the Eastern, Central, Rocky Mountain and Pacific time zones in the United States, and L_m is the longitude [degrees west of Greenwich]. The seasonal correction for solar time S_c [h] was calculated as:

$$S_c = 0.1645 \sin(2b) - 0.1255 \cos(b) - 0.025 \sin(b), \quad (B16)$$

$$b = \frac{2\pi(J - 81)}{364}$$

Appendix 3C

Table 3.C1. Regression relationships, regression coefficients, 95% confidence intervals, the coefficient of determination (R^2) and standard error of the estimate (SEE) at study and test sites for the June-July-August (JJA) period.

Model no.	Regression relationship	Regression coefficients	95% confidence intervals	R^2	SEE study sites, mm	SEE test sites, mm
i	$ET_{0-JJA} (R_s)$	$b_1 = -153.3$	-195.6 -111.0	0.66	72.9	67.1
		$b_2 = 3.4$	3.2 3.6			
ii	$ET_{0-JJA} (R_s, T)$	$b_1 = -218.9$	-263.2 -174.7	0.69	69.4	63.9
		$b_2 = 4.1$	3.8 4.4			
		$b_3 = -5.2$	-6.6 -3.7			
iii	$ET_{0-JJA} (R_s, T, RH)$	$b_1 = 575.2$	476.6 673.8	0.80	55.2	42.9
		$b_2 = 1.9$	1.5 2.2			
		$b_3 = -1.9$	-3.2 -0.7			
		$b_4 = -6.2$	-6.9 -5.5			
iv	$ET_{0-JJA} (R_s, T, RH, U)$	$b_1 = 442.7$	343.5 541.9	0.82	52.2	44.1
		$b_2 = 1.8$	1.5 2.2			
		$b_3 = 1.6$	0.1 3.0			
		$b_4 = -5.8$	-6.5 -5.1			
		$b_5 = 22.2$	16.5 27.9			
v	$ET_{0-JJA} (R_s)_{JJA}$	$b_1 = -251.6$	-300.7 -202.5	0.65	73.6	65.9
		$b_2 = 2.7$	2.6 2.9			
vi	$ET_{0-JJA} (R_s, T)_{JJA}$	$b_1 = -459.1$	-495.5 -422.7	0.84	48.8	44.0
		$b_2 = 2.3$	2.2 2.4			
		$b_3 = 13.9$	12.8 15.0			
vii	$ET_{0-JJA} (R_s, T, RH)_{JJA}$	$b_1 = 210.1$	147.5 272.7	0.92	33.9	32.2
		$b_2 = 1.2$	1.1 1.3			
		$b_3 = 9.8$	9.0 10.7			
		$b_4 = -4.2$	-4.6 -3.8			
viii	$ET_{0-JJA} (R_s, T, RH, U)_{JJA}$	$b_1 = 17.1$	-25.5 60.8	0.96	22.2	17.0
		$b_2 = 1.3$	1.2 1.4			
		$b_3 = 12.3$	11.7 12.8			
		$b_4 = -3.5$	-3.8 -3.3			
		$b_5 = 26.6$	24.6 28.7			

Chapter 4. Evaluating a distributed hydrologic model at the catchment scale against a hypothetical reality dataset – tests of soil parameterization

Abstract

Hydrologic data scarcity, mostly observed head and soil moisture states, is often identified as the one of the most important limitations in evaluating distributed hydrologic models. To overcome data limitation issues, we propose a framework for evaluating the sensitivity of distributed hydrologic models at the catchment scale that is based on a hypothetical reality (HR) dataset. The HR is a synthetically generated dataset using the finite element 3D fully coupled surface-subsurface Integrated Hydrology Model (VanderKwaak, 1999), that emulates the hydrologic behavior of the Tarrawarra catchment located in southeastern Australia. A second model, MODHMS (Panday and Huyakorn, 2004), is used against the HR for model calibration and subsequent sensitivity tests. We use test examples from long-term simulations to investigate the effects of soil parameterization, on both the integrated and distributed MODHMS hydrologic responses. Simulations show that at Tarrawarra, both the water retention curve and the saturated hydraulic conductivity K_{sat} , control the soil moisture spatial distribution and runoff generation during wet periods. For the same K_{sat} , more water retentive soils are less prone to pattern formation and less conducive to runoff generation than sandier soils, which are more responsive and have higher soil moisture spatial variability. For the same water retention curve, K_{sat} controls the level and spatial variability of soil moisture and affects the shape, timing, and magnitude of the hydrograph. During dry periods the water retention parameters and K_{sat} control the saturation level, but have little influence on pattern formation and spatial variability.

4.1. Introduction: why use hypothetical reality datasets to evaluate distributed hydrologic models?

4.1.1. Challenges related to applying physically-based distributed hydrologic models

Physically-based distributed hydrologic models that follow the blueprint of *Freeze and Harlan* [1969] numerically solve the partial differential equations governing water movement on the surface and through the soil. These models can incorporate spatial variability in the characterization of land cover, soil types, and driving data such as precipitation and potential evapotranspiration. They simulate spatial and temporal patterns of the distributed response (e.g. internal fluxes and states) and temporal variation of the integrated response (discharge). Examples of such models, many reviewed by *Kampf and Burges* [2007a], include THALES [*Grayson et al.*, 1992a, 1995], SHE [*Abbott et al.*, 1986a, 1996b], DHSVM [*Wigmosta et al.*, 1994, 2002], InHM [*VanderKwaak*, 1999], tRIBS [*Ivanov et al.*, 2004], MODHMS [*Panday and Huyakorn*, 2004] and many others. Although applications of distributed models often assume that the incorporation of spatial variability improves confidence in model predictions, in many cases these predictions are plagued by a relatively high degree of uncertainty in model parameters, scale, and process representation. The conflicting and confusing effects these uncertainties have on the simulated discharge have intrigued many hydrologists to the point where even distributed model concepts were questioned [*Grayson et al.*, 1992b], and many discussions about over-parameterization [e.g., *Beven*, 1989], parameter uncertainty [e.g., *Beven and Binley*, 1992], model parsimony and equifinality followed [e.g., *Beven*, 1993, 2006; *Ebel and Loague*, 2006]. Despite the many challenges related to applying such models, the interest in their capabilities to investigate environmental processes such as distributed hydrologic response, effects of land use changes, erosion and non-point sources, and contaminant transport among many others grew over time, and more models became available and were increasingly applied in many parts of the world.

The evaluation of distributed response is often difficult due to the scarcity in the observed soil states and scale discrepancies between instrument point measurements and models. However, the evaluation of hydrograph representation alone should not be considered sufficient in testing and evaluating distributed models [*Beven*, 1989]. Limited datasets of distributed hydrologic variables exist for a small number of experimental catchments around the world, and a few studies have considered model evaluation using both integrated and distributed responses [e.g., *Ebel et al.*, 2008; *Feyen et al.*, 2000; *Anderton et al.*, 2002a, 2002b; *Heppner et al.*, 2007; *Maneta et al.*, 2008a].

At the catchment scale, applications of physically-based distributed hydrologic models have revealed that successfully simulating the hydrograph does not necessarily mean runoff mechanisms [Grayson *et al.*, 1992a] or internal states are unique or equally well represented [Ebel and Loague, 2006; Kampf and Burges, 2007b; Ebel *et al.*, 2008; Maneta *et al.*, 2008]. Studies that have examined how simulated internal states compared with field observations, have found differences in the model performance between the calibration and validation periods [e.g., Refsgaard, 1997; Feyen *et al.*, 2000; Anderton *et al.*, 2002a, 2002b; Vázquez *et al.*, 2008]. Using continuous simulations, Ebel *et al.* [2008] reported that a physically based surface-subsurface model was unable to reproduce observed pore water pressure at sites where flow through bedrock fractures occurs. Heppner *et al.* [2007] found that while the peak flow rates and sediment discharges were well simulated with a physically-based model, the distributed soil moisture content was inadequately represented. Other studies have examined the way the simulated internal states relate to geographic and terrain attributes [e.g., Ivanov *et al.*, 2004; Wu *et al.*, 2007].

Model parameterization has been identified by many hydrologists as one of the biggest sources of uncertainty in applying distributed hydrologic models. Physically-based models are designed to work based on *a-priori* soil parameterization, with values directly measured in the field, or derived from other measurements. This approach can be challenging, due to the issues of heterogeneity and discrepancies between point measurements and model scale [Binely *et al.*, 1989; Christiaens and Feyen, 2001; Christiaens and Feyen, 2002; Anderton *et al.*, 2002b; Zehe *et al.*, 2006], and most often due to the complete lack of measured data. Measuring and/or deriving soil parameters is costly and time consuming, even at small scales. In the absence of any field measurements, parameters describing hydraulic soil properties can be directly extracted from existing databases using soil textural descriptions, if available, but many times these assigned parameter values are modified during calibration so that simulations match the observed hydrograph [e.g., Senarath *et al.*, 2000; Zhang and Savenije, 2005] and/or other internal nodes [e.g., Feyen *et al.*, 2000; Anderton *et al.*, 2002b; Maneta *et al.*, 2008a]. Changes to parameters during calibration are necessary to compensate for the uncertainties in the original parameter estimates as well as for other shortcomings related to model structure. This parameter adjustment process can lead to counterintuitive results, especially when automated calibration is used [e.g., Senarath *et al.*, 2000].

The direct use of database soil hydraulic parameters is also subjective, as the parameters depend on the on the number, type, and location of soil samples available in the data base used and may not be representative for the study catchment (see discussions by Beven, 1989; Christiaens and Feyen, 2001; Mirus, 2009). Investigating

four ways to obtain soil hydraulic parameters from pedo-transfer functions (PTFs), *Christiaens and Feyen* [2001] found that ROSETTA neural network model [*Schaap et al.*, 1999] predictions were least erroneous. Parameter uncertainty analysis emphasized the importance of soil moisture observations to identify effective soil hydraulic parameters [*Christiaens and Feyen*, 2001; *Christiaens and Feyen*, 2002].

4.1.2. Motivation for introducing a hypothetical reality dataset to support distributed hydrologic model testing at the catchment scale

Detailed long term field measurements have helped improve our understanding of distributed catchment hydrologic processes. However, the resources needed for gathering such information are substantial, and no existing data set has the spatial and temporal scope of measurements needed for a rigorous evaluation of any distributed model. Here we propose the use of a synthetic dataset termed *hypothetical reality* (HR) developed for this purpose. This concept has been previously explored using different types of models [e.g., *Troch et al.* 1993; *Loague*, 1988; *Gan and Burges*, 1990]. Tests against a HR of hydrologic response are a first step towards overcoming some of the issues encountered with extrapolating conclusions based on a series of unique, data-limited field sites. The use of HR instead of field measured data has the advantage of a significantly increased level of detail in hydrologic states and variables both spatially and temporally, and the HR is assumed to be error free.

4.1.3. Objectives of this study

The main objective of this work is to illustrate the use of a framework for evaluating distributed hydrologic models at the catchment scale based on a HR dataset. The HR hydrologic response is designed to emulate the hydrologic response of the Tarrawarra catchment, Australia in great detail (see [*Mirus et al.*, 2009]). A distributed model can be evaluated against the HR dataset using both the integrated (discharge) and distributed responses (e. g. total head and degree of saturation). As a second model, we use MODHMS [*Panday and Huyakorn*, 2004; *HydroGeoLogic, Inc*, 2006], to show the flexibility and functionality of the proposed framework. In the following sections we describe: i) the HR dataset, ii) MODHMS application to Tarrawarra, iii) testing objectives, model scenarios and evaluation strategies, iv) provide examples of test scenarios that include tests of soil parameters, and v) results and discussion.

4.2. Tarrawarra-like Hypothetical Reality

The zero-order Tarrawarra catchment (37°39'S, 145°26'E, 100 m elevation) is a 10.5 ha grass pasture located about 50 km east of Melbourne, in southern Australia (Figure 4.1a). The area has a temperate Mediterranean climate with mild winters with no snow and warm dry summers. Most of the rainfall occurs during the May to October period. The hydrology of the catchment has been extensively investigated [e.g., *Western and Grayson, 1998; Grayson and Western, 1998; Western et al., 1998a, 1998b, 1999, 2001; Thierfelder et al., 2003; Park and van de Giesen, 2004; Wilson et al., 2004; Teuling and Troch, 2005; Teuling et al., 2006; Perry and Niemann, 2007, 2008*]. There are no permanent channels within the catchment, but ephemeral surface runoff occurs during some storms. The dominant runoff generation mechanism is saturation excess (Dunne) overland flow [*Western and Grayson, 1998; Mirus et al., 2009*]. The relief consists of gently sloping hills forming two converging depressions in which water accumulates and flows downhill to the catchment outlet. Soil depth varies between 0.4m on the higher elevation areas to 1.5m in the depressions, and the hills have slopes of about 11-14% with the main drainage line of about 4% [*Western and Grayson, 1998*]. Topographic features define the spatial patterns of soil moisture during the wet season; more water accumulates in the depressions than in the rest of the catchment, driven by lateral surface and subsurface flow [*Grayson et al., 1997; Western et al., 1999*]. During summer, when the landscape is dry, there is relatively little spatial organization of soil moisture [*Western et al., 1999*]. The catchment has a structure and topography that is representative of many zero order catchments around the world with temperate to Mediterranean sub-humid climate conditions where water movement through soil is influenced by local topography and soil characteristics.

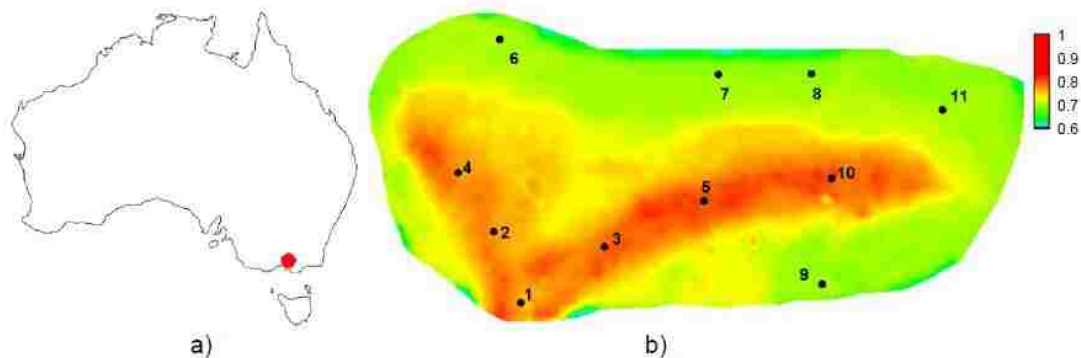


Figure 4.1 a) Tarrawarra location, Australia and b) example of snapshot of degree of saturation from the HR hydrologic response in the top 2 cm, 12 May 1996, 0:00AM.

The Tarrawarra-like HR hydrologic response is generated using the high resolution fully coupled 3D variably saturated subsurface and 2D surface flow Integrated Hydrologic Model (InHM) [VanderKwaak, 1999]. This HR was developed in two steps. First, InHM was set up to simulate the dominant hydrologic features of the Tarrawarra catchment using the original data collection described in *Western and Grayson* [1998]. Details of the first step, the development of InHM boundary value problem for Tarrawarra, parameter evaluation and simulation results are thoroughly described in *Mirus et al* [2009]. In the second step we used a different, 11-year long meteorological record from the closest available station (37°73'S, 145°41'E, elevation: 83 m), located about 12.1 km driving distance southwest from Tarrawarra. We selected the period Jan 1, 1996 – Dec 31, 2006 because it had data with high enough resolution and quality to be assembled into half-hourly potential evapotranspiration (PET) rates using the Penman-Monteith [Monteith, 1981; Allen et al., 1998] model. Precipitation time series were prepared from measurements at the same station. The calendar year 1996 was the most balanced year, with the annual PET within 2% of annual precipitation of 950 mm. The remaining 10 years were marked by unusual dry weather in Australia [Pincock, 2007], with annual PET at Tarrawarra exceeding annual precipitation by percentages ranging from 25% in 2004 to 63 % in 1997.

Using the 11-year long half-hourly time series of PET and precipitation, assumed uniformly distributed across the catchment, as inputs to the *Mirus et al.*, [2009] Tarrawarra InHM boundary value problem, an HR response was generated for long term assessments. The resulting 11-year long time series of hydrograph output and internal states at 55 observation nodes (at four depths: 0.02m, 0.1m, 0.5m and 1m, for each of the 11 locations shown in Figure 4.1b) as well as daily “snapshots” of the distributed response at all nodes, 73,425 in total, during the 6-month long (May to October) wet season each year.

4.3. Distributed model testing and evaluation methods

4.3.1. Test model, MODHMS

To illustrate the functionality of the proposed model evaluation framework, we use a three dimensional fully-coupled surface-subsurface distributed model, MODHMS [Panday and Huyakorn, 2004; HydroGeoLogic, Inc, 2006], as a test model. MODHMS is a complex model suitable for catchment-scale applications where lateral flow is important for topography driven soil moisture patterns to form. The modular flexible structure

allowed MODHMS to be used previously in variety of problems such as parameter exploration and optimization [Vrugt et al., 2004; Shoups et al. 2005; Maneta et al., 2008], estimation of shallow water evaporation in irrigated regions [Young et al., 2007] and tropical catchment simulations [Werner et al, 2006].

MODHMS is a grid-based model, built on the original USGS MODFLOW [McDonald and Harbaugh, 1988] platform for groundwater flow that numerically solves a finite-difference form of Richards' equation, for unsaturated subsurface flow and the diffusive wave approximation to the de Saint Venant equations for the shallow water overland flow derived by Gottardi and Venutelli [1993]. Model equations are described by Panday and Huyakorn [2004] and HydroGeoLogic, Inc [2006] and briefly summarized in Appendix 4A. The van Genuchten formulations are used for the functional forms of the relative permeability, k_{rw} , and soil moisture retention curves, (Eq.3 and 4 in Appendix 4A).

4.3.2. Evaluation objectives and model scenarios

4.3.2.1. Testing objectives

The *evaluation objectives* constitute the main model sensitivity questions to be addressed (e.g. how does the soil depth affect soil moisture patterns in MODHMS?). Here we address two specific testing objectives related to the MODHMS configuration of soil parameters: I) how does the shape of the soil moisture retention curve affect MODHMS hydrologic response, and II) what is the sensitivity of the saturated hydraulic conductivity, K_{sat} , to hydrologic response for the same soil moisture retention curve? In our approach, we first configure a MODHMS reference scenario using a similar parameterization to the model used to generate the HR dataset (see [Mirus et al., 2009]). The purpose of the reference scenario was not to re-create the HR or to compare the two models, but rather to establish a base case run with similar soil stratigraphy and soil parameterization, where only the ET module was minimally calibrated to match the HR. From this reference scenario we explore how the soil parameters and soil depths affect MODHMS hydrologic response through model *exploratory/behavioral runs*.

4.3.2.2. Testing scenarios

4.3.2.2.1. Reference case scenario

In the reference case scenario, the Tarrawarra catchment is represented in MODHMS by a plan view grid of 20 rows and 40 columns of cells of 14.25 by 13.50 m size. The domain is discretized vertically into 38 layers of variable depth from the surface as follows: 0.02

m (layers 1-11), 0.05m (layers 12-23), 0.1m (layers 24-28), and 0.2-0.33 m, with progressively increasing thickness (layers 29-38). The soil is stratified in three layers: A horizon, B horizon, and bedrock, with layer depths of 0.22, 1.1 and 14.5 m, respectively. The saturated hydraulic conductivities K_{sat} are 2×10^{-6} , 2×10^{-7} and $2 \times 10^{-9} \text{ m} \cdot \text{s}^{-1}$, respectively, and the van Genuchten parameters α are 4, 4.5, and 6 m^{-1} , and β are 2.5, 2.0, and 1.5, respectively [Mirus et al, 2009]. Residual water content was set constant for all layers: $\vartheta_r = 0.3 \text{ m}^3 \cdot \text{m}^{-3}$ while the saturated water content, ϑ_s , was 0.48, 0.38 and $0.2 \text{ m}^3 \cdot \text{m}^{-3}$ for the three hydrogeologic layers, respectively [Mirus et al, 2009]. The main difference between the MODHMS reference case scenario and HR InHM soil parameterization is the use of constant, rather than Kriged soil depths for the A horizon layer (Fig.2 in [Mirus et al, 2009]). The catchment bottom and lateral boundaries are considered as no-flow boundaries and the surface boundary condition is set to a zero depth gradient. The digital elevation model (DEM) grid cell size was 5m and the overland flow parameterization was similar to InHM [Mirus et al, 2009].

4.3.2.2.2. Model scenarios for objectives I and II

In the model scenarios designed for objectives I and II, we test the sensitivity of simulations to soil parameterization, specifically the saturated hydraulic conductivity K_{sat} and the van Genuchten parameters for both the relative permeability (Eq.3) and soil moisture retention curve (Eq.4) in Appendix 4A. We used the ROSETTA soil database and computer program for estimating soil hydraulic parameters with hierarchical PTFs [Schaap et al., 2001].

ROSETTA's simplest model provides a look-up table of class-average values of hydraulic parameters for the twelve United States Department of Agriculture (USDA) textural classes along with one standard deviation (SD) uncertainties of the class average values. ROSETTA can also provide estimates of the hydraulic characteristics from other types of soil information such as field soil texture measurements, bulk density, and one or two water retention points with a neural network based model. Perusal of the ROSETTA look-up table (a section is shown in Table 4.1 for three textural classes in ROSETTA's units and format, with SD in parentheses) shows that ϑ_r , ϑ_s , α , and β have widely overlapping variation intervals between soil textural classes. An example of the relatively high scatter around the average retention curve for loam is also illustrated in Fig.7, Schaap et al. [2001].

Table 4.1 Excerpt from ROSETTA textural class look-up table.

Textural class	ϑ_r $\text{cm}^3 \cdot \text{cm}^{-3}$	ϑ_s $\text{cm}^3 \cdot \text{cm}^{-3}$	$\log(\alpha)$ $\log_{10}(1/\text{cm})$	$\log(\beta)$ \log_{10}	K_{sat} $\log(\text{cm} \cdot \text{day}^{-1})$
Clay loam	0.079 (0.076)	0.442 (0.079)	-1.801 (0.69)	0.151 (0.12)	0.913 (1.09)
Loamy sand	0.049 (0.042)	0.390 (0.070)	-1.459 (0.47)	0.242 (0.16)	2.022 (0.64)
Silty clay	0.111 (0.119)	0.481 (0.080)	-1.790 (0.64)	0.121 (0.10)	0.983 (0.57)

We establish MODHMS A, B, and C primary scenarios assuming the average values for ϑ_r , α , and β , representative for the clay loam, loamy sand, and silty clay textural classes in ROSETTA, shown in Table 4.1. The ϑ_r , α , and β values that define the shape of the soil moisture retention curve varied between the A, B, and C scenarios, but we maintained K_{sat} and ϑ_s fixed at $3.26 \times 10^{-6} \text{ m} \cdot \text{s}^{-1}$, and $0.45 \text{ m}^3 \cdot \text{m}^{-3}$, respectively, values within one standard deviation interval for all three textural classes. For comparison, the averaged measured soil hydraulic conductivities K_{sat} at Tarrawarra in the top 30 cm and between 30 and 60 cm are $3.74 \times 10^{-6} \text{ m} \cdot \text{s}^{-1}$ and $1.17 \times 10^{-6} \text{ m} \cdot \text{s}^{-1}$, respectively after removing the outliers.

To test the influence of K_{sat} , in the secondary scenarios A1, A2, B1, B2, C1, and C2 we maintained the same ϑ_r , ϑ_s , α , and β and changed K_{sat} sequentially to the upper and lower limits of one SD interval for K_{sat} for each textural class. The three shapes of soil moisture retention curve cover a range of potential behaviors among classes or even within the same class. An example showing the variability of the shape within a class is illustrated in Figure 4.2a for clay loam where the average for the class is drawn as well as the curves assuming a one SD shift from the average for all van Genuchten parameters. Soil parameterizations for all scenarios are summarized in Table 4.2. For comparison again, the soil moisture retention curve drawn using the van Genuchten parameters predicted by ROSETTA based on soil samples collected at the site for the top 30 cm is similar to ROSETTA's clay loam textural class (Figure 4.2a). Figures 4.2b, 4.2c and 4.2d show the soil water retention curves for the three soil layers used in the MODHMS reference scenario and the clay loam, silty clay, and loamy sand textural curves from the ROSETTA look-up table, respectively, for ϑ_s equal to $0.45 \text{ m}^3 \cdot \text{m}^{-3}$ used in the A, B, and C scenarios. We use the same soil depth and ET representation as in the reference case scenario. All scenarios assume one homogenous layer type (clay loam, or loamy sand, or silty clay, respectively), overlaying a bedrock layer having the same depth and soil parameters as in the reference case scenario. Half-hourly precipitation and potential evapotranspiration rates were assumed constant across the catchment in all scenarios.

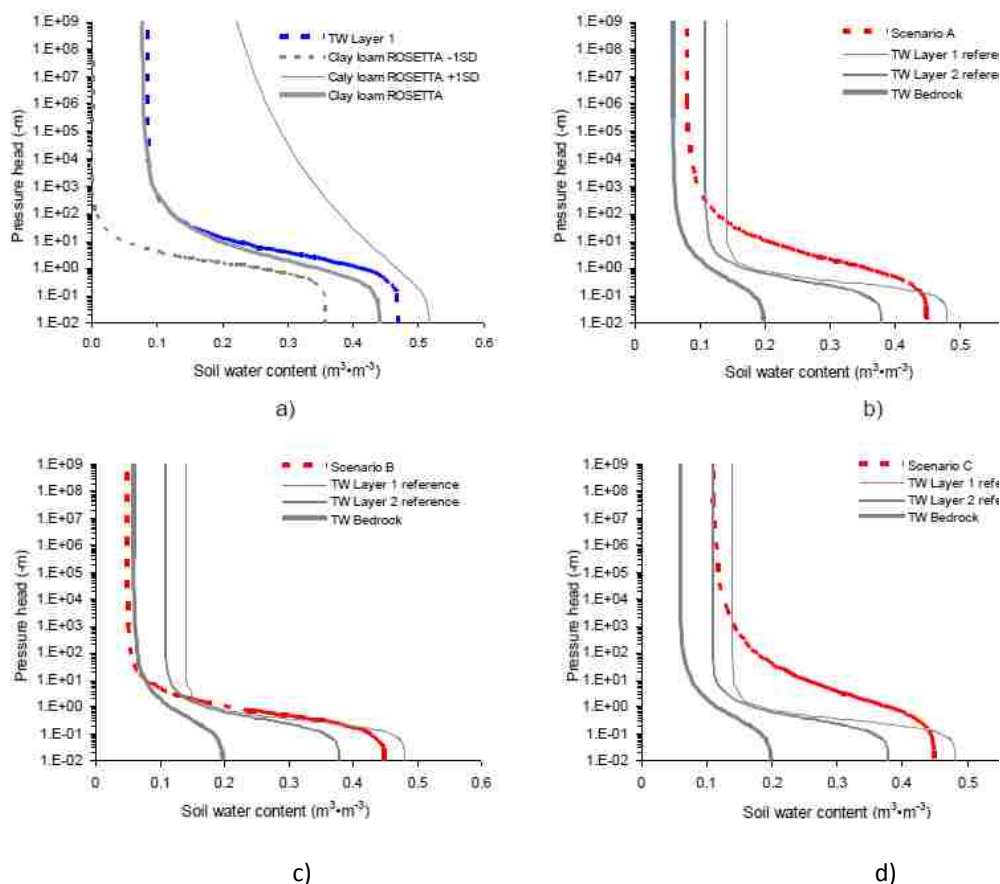


Figure 4.2 a) Clay loam water retention curves and the approximate curve at Tarrawarra predicted by ROSETTA; b), c), d) soil water retention curves of the three layers used in the MODHMS reference scenario and the clay loam, loamy sand, and silty clay curves used in the MODHMS A, B, and C scenarios.

Table 4.2 Summary of soil parameterization in all scenarios addressing testing objectives I and II.

Scenario	Testing objective	K_{sat} $\log(\text{cm}\cdot\text{day}^{-1})$	$\log(\alpha)$ $\log_{10}(1/\text{cm})$	$\log(\beta)$ \log_{10}	θ_r $\text{m}^3\cdot\text{m}^{-3}$	Soil depth m	Soil class
A	I	1.450	-1.801	0.151	0.079	1.32	Clay loam
A1	II	-0.177	-1.801	0.151	0.079	1.32	Clay loam
A2	II	2.003	-1.801	0.151	0.079	1.32	Clay loam
B	I	1.450	-1.459	0.242	0.049	1.32	Loamy sand
B1	II	1.382	-1.459	0.242	0.049	1.32	Loamy sand
B2	II	2.662	-1.459	0.242	0.049	1.32	Loamy sand
C	I	1.450	-1.790	0.121	0.111	1.32	Silty clay
C1	II	0.413	-1.790	0.121	0.111	1.32	Silty clay
C2	II	1.553	-1.790	0.121	0.111	1.32	Silty clay

4.3.2.3. Scenario evaluation

As part of the model sensitivity tests we employ continuous long-term simulations from which we select representative runoff events or dry periods for a closer analysis. This approach allows us to avoid the use of periods that are influenced by the choice of initial conditions and that may or may not be representative of the catchment hydrologic behavior. Because Tarrawarra is an ephemeral catchment, during the wet periods we evaluate both the hydrograph and soil moisture states, whereas during the dry period when no runoff occurs only the soil moisture patterns are examined.

We analyze the 1 June 1999 to 11 November 2000 period, which included two wet seasons separated by a dry season. For all scenarios, we first simulate a warm-up period, 1 August 1996 to 1 June 1999, which begins in the wet season of 1996. The initial conditions are specified as a fully saturated domain, in accordance with the HR states on 1 August 1996 0:00 AM. At Tarrawarra, the estimated PET typically exceeds accumulated precipitation during the summer months, and is the opposite during the winter months [*Western and Grayson, 1998*]. During the 1999 and 2000 wet seasons, that are part of the evaluation period, precipitation exceeded PET by 8% in 1999 and was lower than PET by about the same amount in 2000. In the dry season of 1999-2000, PET was higher than the accumulated precipitation by approximately 50%. For comparison, during all wet seasons of the 1996-2006 HR period, precipitation to PET ratios ranged between 1.16 and 0.66 and between 0.29 and 0.74 during the dry seasons.

We show the simulated MODHMS hydrograph for the entire evaluation period for the reference case scenario and compare the HR temporal soil moisture variation patterns at 4 different depths at a “wet” location (node 4 in Figure 4.1b) and a “dry” location, (node 11 in Figure 4.1b). The “wet” node (4) is located in a swale, the “dry” node (11) is near the upper catchment boundary where water movement is vertical with little lateral supplemental delivery. We show soil moisture variations at node 4 at 0.02m and 0.5 m depth and node 11 at 0.1 and 1 m depth to illustrate a range of distributed response between wet and dry locations and for a range of depths. For the 9 scenarios investigated we extract two shorter time periods from the evaluation period for a closer examination: an 11-day wet period, 6 August 1999 4:00 PM to 17 August 1999 2:00 AM (Figure 4.3a, period A), and an 8-day dry period 20 January 2000 8:00 AM to 28 January 2000 10:30 AM (Figure 4.3a, period B).

We show how different parameter configurations listed in Table 4.2 affect the near surface MODHMS generated hydrologic response; the distributed response is illustrated with modelled soil moisture time series at 0.02 m and 0.1 m for the wet (4) and the dry

(11) nodes and for the wet and the dry periods (A and B). Soil moisture spatial patterns for the top 2 cm are shown every 24 hours; there are 8 patterns during the wet period A, and 9 during the dry period B.

Soil moisture temporal and spatial distribution patterns for the MODHMS simulation results can be compared visually with those from the HR. We quantify the MODHMS hydrograph output for all scenarios relative to the HR hydrograph using the Nash-Sutcliffe efficiency criterion NSE [Nash and Sutcliffe, 1970] NSE.

$$NSE = 1 - \frac{\sum (Q_{MODHMS} - Q_{HR})^2}{\sum (\bar{Q}_{HR} - Q_{HR})^2} \quad (4.1)$$

where Q_{MODHMS} is the MODHMS discharge generated for each scenario, Q_{HR} is the HR discharge and \bar{Q}_{HR} is the average HR discharge for the period of interest.

4.4. Simulation results

4.4.1. MODHMS Reference case scenario

During the 1 June 1999 to 11 November 2000 evaluation period, 19 HR hydrograph events larger than $5 \text{ l}\cdot\text{s}^{-1}$ occurred, 5 in the wet season of 1999, and 14 in the wet season of 2000, with peak magnitudes ranging between $6.2 \text{ l}\cdot\text{s}^{-1}$ to $77.7 \text{ l}\cdot\text{s}^{-1}$. The timing and magnitude of the simulated reference case scenario MODHMS hydrographs match well with the HR, with a NSE of 0.86 (time increment 30 minutes) for the entire evaluation period (Figure 4.3a and Table 4.3). The larger peak flow rates are simulated better, especially when antecedent soil moisture conditions are closer to saturation. Smaller peak flow rates are at times overestimated, mostly when they have drier antecedent conditions, such as the peaks occurring during the wet period A for which the NSE dropped to 0.25.

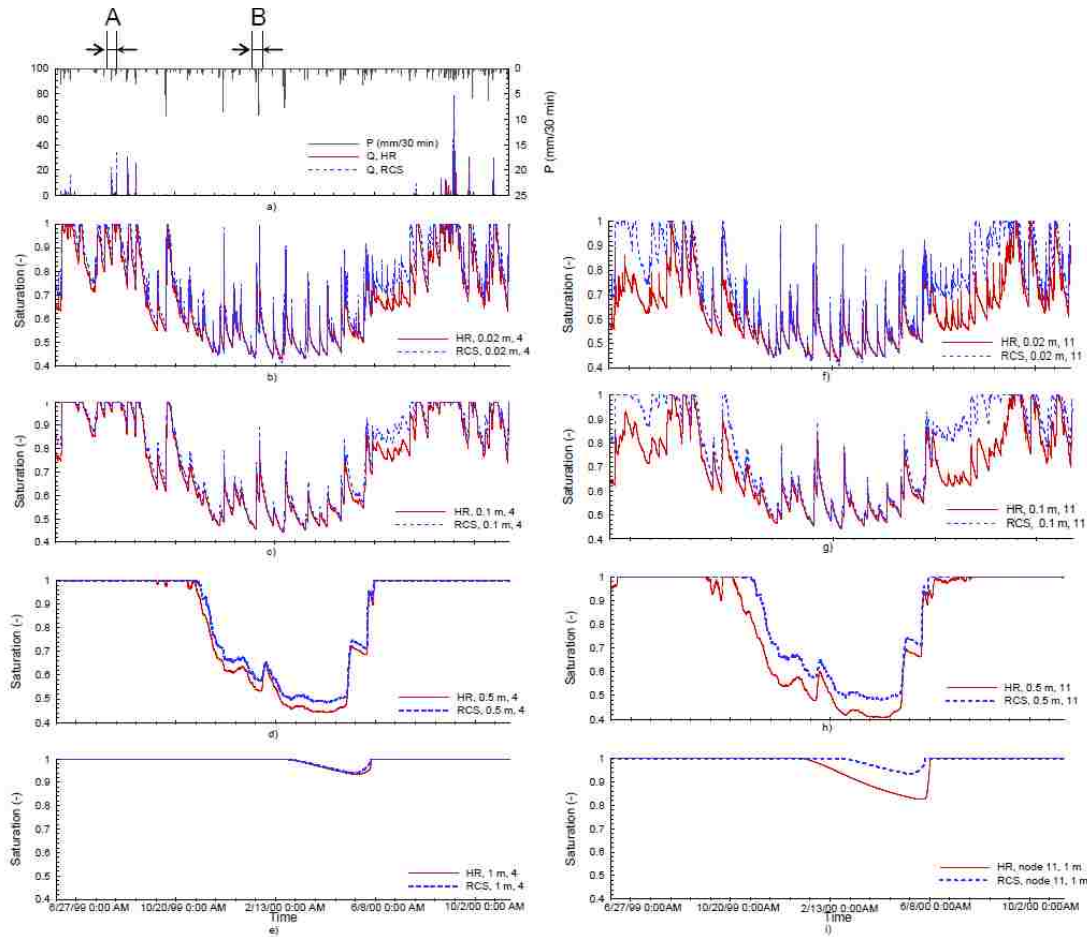


Figure 4.3 a) HR and MODHMS reference case scenario (RCS) hydrographs, b) - i) HR and MODHMS RCS saturation at node 4 and node 11, depths 0.02, 0.1, 0.5 and 1 m during the evaluation period.

Figures 4.3b – 4.3i, which show time series of saturation, s , indicate that the MODHMS reference case scenario approximates very well the HR saturation at wet node 4 at all depths: 0.02, 0.1, 0.5 and 1m. At dry node 11, s is well simulated during the dry period, but tends to reach saturation faster near the surface during the wetter periods as shown in Figure 4.3 f and g. Deeper soil saturation levels at node 11 differ slightly in timing and magnitude from the HR, but the temporal variation patterns are generally consistent with the HR (Figure 4.3g and h). These discrepancies are likely due, among other factors, to the differences in soil depth representation (Krieged in InHM and constant in MODHMS) and to the ET parameterization in MODHMS.

4.4.2. MODHMS A, B, and C scenarios, wet period A

The wet period A is characterized by long duration, relatively low intensity rain events, typical of the Tarrawarra wet seasons. During wet period A, two HR runoff events occurred: the first peak hydrograph, with a magnitude of $12.3 \text{ l}\cdot\text{s}^{-1}$, occurred 9 h after the beginning of the 11-hour long rain event (maximum intensity of 2.5 mm/30 min) (Figure 4.4a). The antecedent soil moisture states ranged from saturation values on the upper slopes of about 0.6 to about 0.8 in the depressions (Figure 4.4f, first HR (i)). A second higher peaked hydrograph followed, influenced by the wetter soil moisture conditions associated with a 4-h duration antecedent rain event shown in Figure 4.4f, HR (vi); the depressions are largely saturated and the upper slopes have saturation of about 0.8. The peak flow rate was $18.1 \text{ l}\cdot\text{s}^{-1}$ and the total rain duration was 13 h (maximum intensity of 1.3 mm/30 min). During wet period A the surface at node 11 remained unsaturated (Figure 4.4 d-f) and the HR peak hydrographs were of small to medium size compared with the range of peak flow rates simulated during the evaluation period (Figure 4.3) and during the entire HR (1996 – 2006) period, for which most of the peaks ranged between 10 to $75 \text{ l}\cdot\text{s}^{-1}$ with only three peaks higher than $100 \text{ l}\cdot\text{s}^{-1}$.

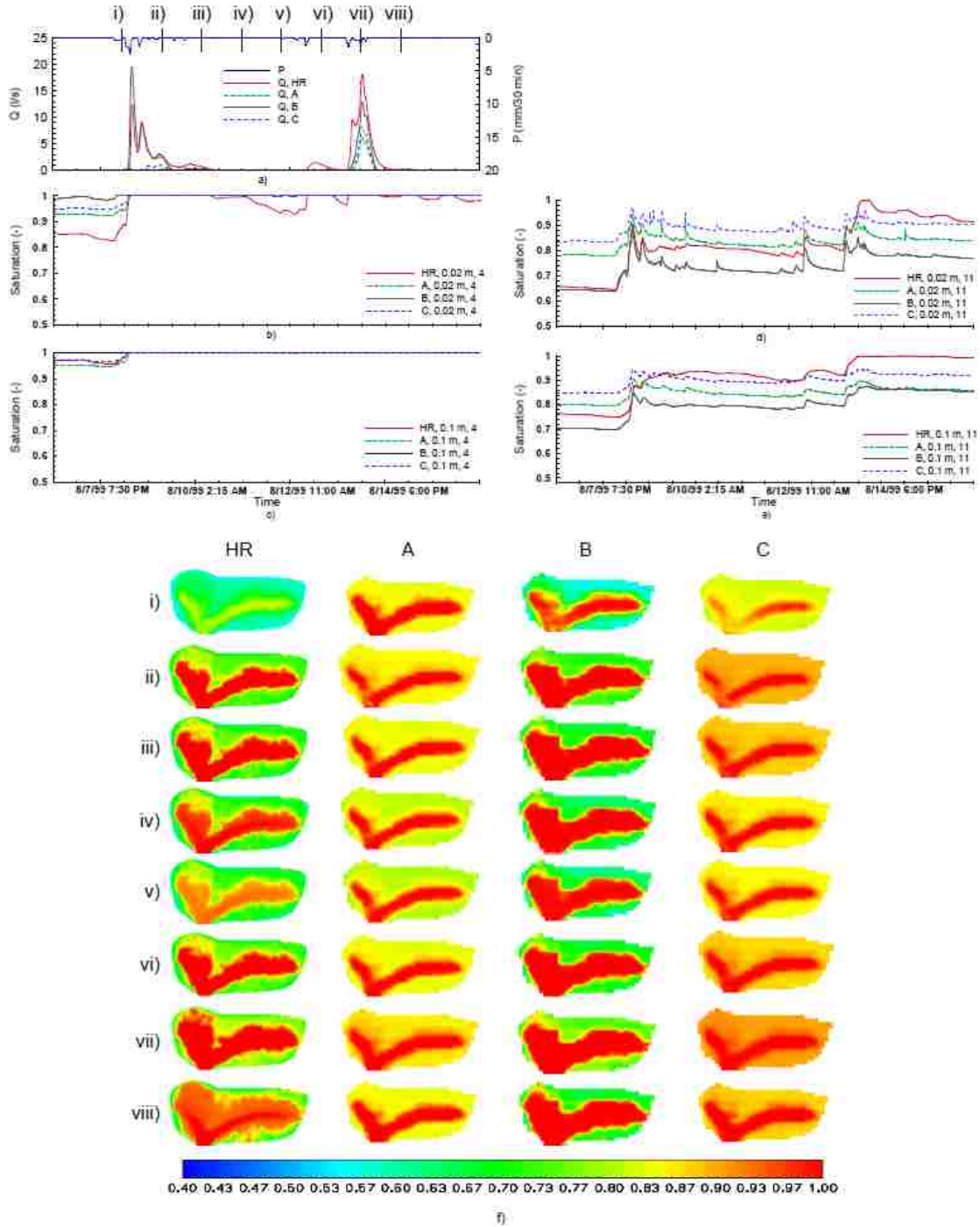


Figure 4.4 a) HR and A, B, and C MODHMS hydrographs during the wet period A; b) - e) HR and A, B, and C MODHMS saturation at node 4 and node 11, depths 0.02 and 0.1 m; f) spatial distribution of HR and A, B, and C MODHMS saturation in the top 2 cm at 24 h intervals, 8 August 1999, 0:00 AM to 15 August 1999, 0:00 AM.

The A, B, and C scenarios assume the same K_{sat} and soil porosity and different soil moisture retention curves (Table 4.2). Figure 4.4a shows that only the MODHMS B scenario produced both HR hydrograph events during the wet period A, while the A, and C scenarios produced only the second peak, with a smaller magnitude in both cases, and lower NSE values (Table 4.3). The B scenario had the highest saturation level at the wet observation node 4 and the lowest at the drier region of node 11 (Figure 4.4 b-f). After the first rain event, the soil remained saturated in the wetter region 4 for all scenarios, while at the drier node 11 none of the A, B, and C soil moisture scenarios yielded saturation (Figure 4.4 b-f). The spatial distributions of saturation, shown every 24 hours beginning on 8 August 1999 0:00 AM in Figure 4.4f, indicate that the loamy sand B scenario approximates best the HR soil moisture patterns.

Table 4.3 MODHMS efficiency criterion NSE for the 10 MODHMS scenarios during the 1 June 1999-11 November 2000 evaluation period and wet and dry periods A and B.

Scenario	NSE evaluation period	NSE wet period, A
Reference case	0.86	0.25
A	0.28	0.26
A1	-2.9	0.10
A2	0.28	0.61
B	0.62	0.75
B1	0.65	0.75
B2	0.13	0.48
C	0.24	0.40
C1	-0.35	-0.15
C2	0.29	0.42

4.4.3. MODHMS A, B and C scenarios, dry period B

The dry period B (Figure 4.5a) is characterized by two different rain events: a 14.5-hour long duration, low intensity (2.6 mm/30 min) event, followed by a 3.5-hour short duration, higher intensity (9.2 mm/30 min) summer storm. After the first rain event, the HR soil moisture increased from a relatively uniform saturation of about 0.4 to about 0.8 (Figure 4.5 b –e). The soil dried relatively uniformly for about 4.5 days, when a second event produced a very small peak hydrograph of only $0.6 \text{ l}\cdot\text{s}^{-1}$ (Figure 4.5a).

Compared with the wet period A, during which the dry and the wet node had noticeably different temporal variation patterns, the HR saturation varies similarly, in shape and

magnitude (Figure 4.5 b-e) during dry period B at both wet node 4 and dry node 11,. Saturation levels simulated for the A, B, and C MODHMS scenarios also vary uniformly at wet and dry nodes 4 and 11, with the loamy sand B scenario approximating best the HR (Figure 4.5 b-e). The spatial distributions of saturation, (every 24 hours from 22 January 2000, 0:00 AM), show that during dry period B there are no clear soil moisture organization patterns and that the wet (in the depressions) and the dry regions (upslope) vary relatively uniformly with different magnitudes for the three (A, B, and C) scenarios, irrespective of the shape of soil moisture retention curve (Figure 4.5 f). No HR soil moisture spatial distributions are available for dry period B, however, Figure 4.5 b-e and other nodes examined (Figures not shown) indicate that the HR soil moisture, s is relatively uniformly distributed across the catchment during the summer season. No peak hydrographs were simulated for the A, B, and C scenarios during dry period B.

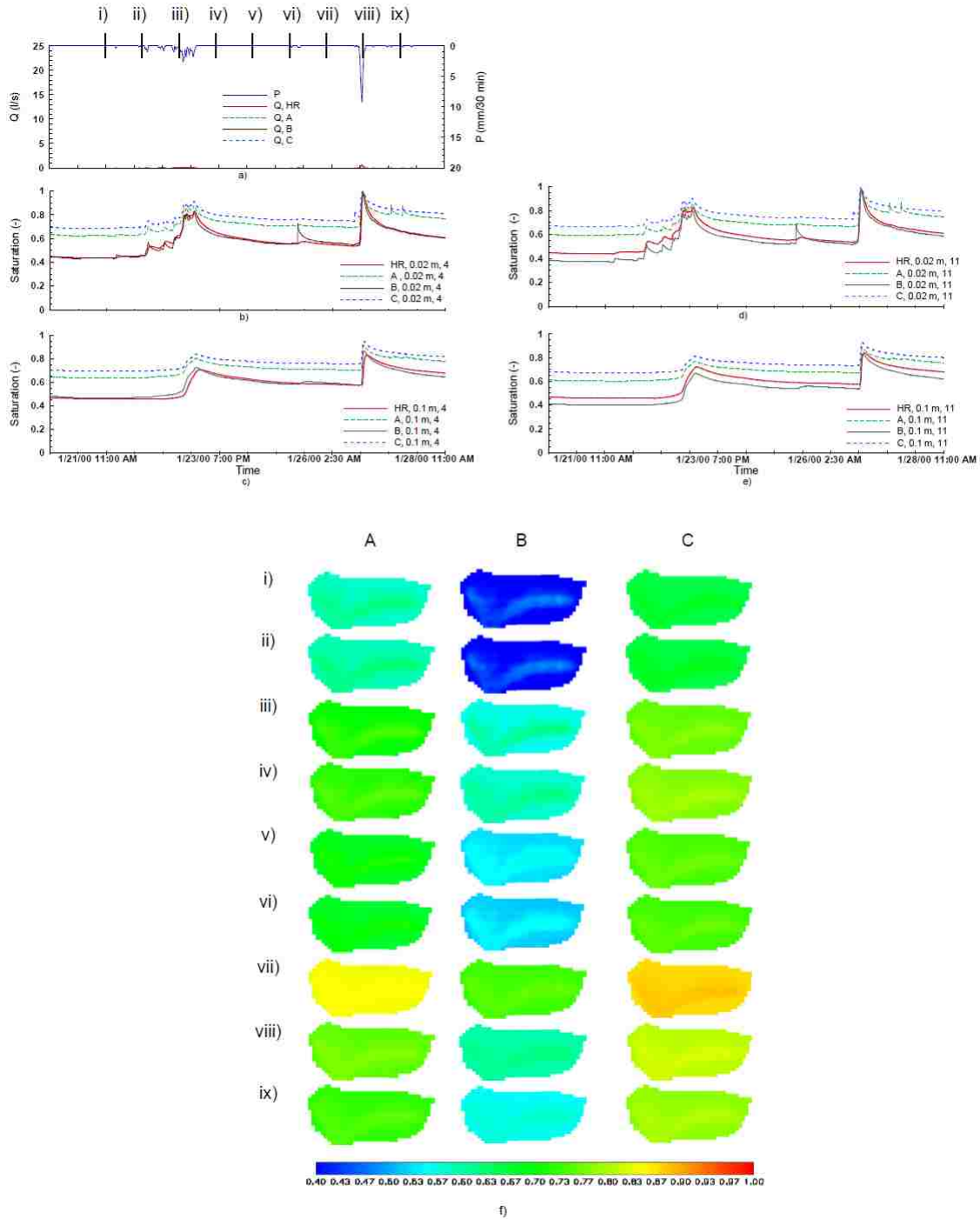


Figure 4.5 a) HR and A, B, and C MODHMS hydrographs during the dry period; B b) - e) HR and A, B, and C MODHMS saturation at node 4 and node 11, depths 0.02 and 0.1 m; f) spatial distribution of HR and A, B, and C MODHMS saturation in the top 2 cm at 24 h interval, January 21 2000, 0:00 AM to January 29 2000, 0:00 AM.

4.4.4. MODHMS A1, A2, B1, B2, C1, and C2 scenarios, wet period A

The A1, A2, B1, B2, C1, and C2 scenarios assume the same class average soil moisture retention curve of clay loam, loamy sand, and silty clay, respectively, for which K_{sat} was sequentially set to the lower and upper values of the 1-SD interval from the class mean according to the ROSETTA database (Table 4.2). The integrated response for wet period A varied from not simulating the peak hydrographs at all in the C1 scenario to approximating relatively well the HR in the B1 scenario; the NSE ranged between -0.15 and 0.75 (Table 4.3). Figures 4.6 b, c, g, h, l, and m show that at wet node 4, the soil is saturated or near saturation in all cases, but the integrated response (Figure 4.6 a, f, k), and saturation levels at dry node 11 (Figure 4.6 d, e, i, j, n, o), vary widely between scenarios.

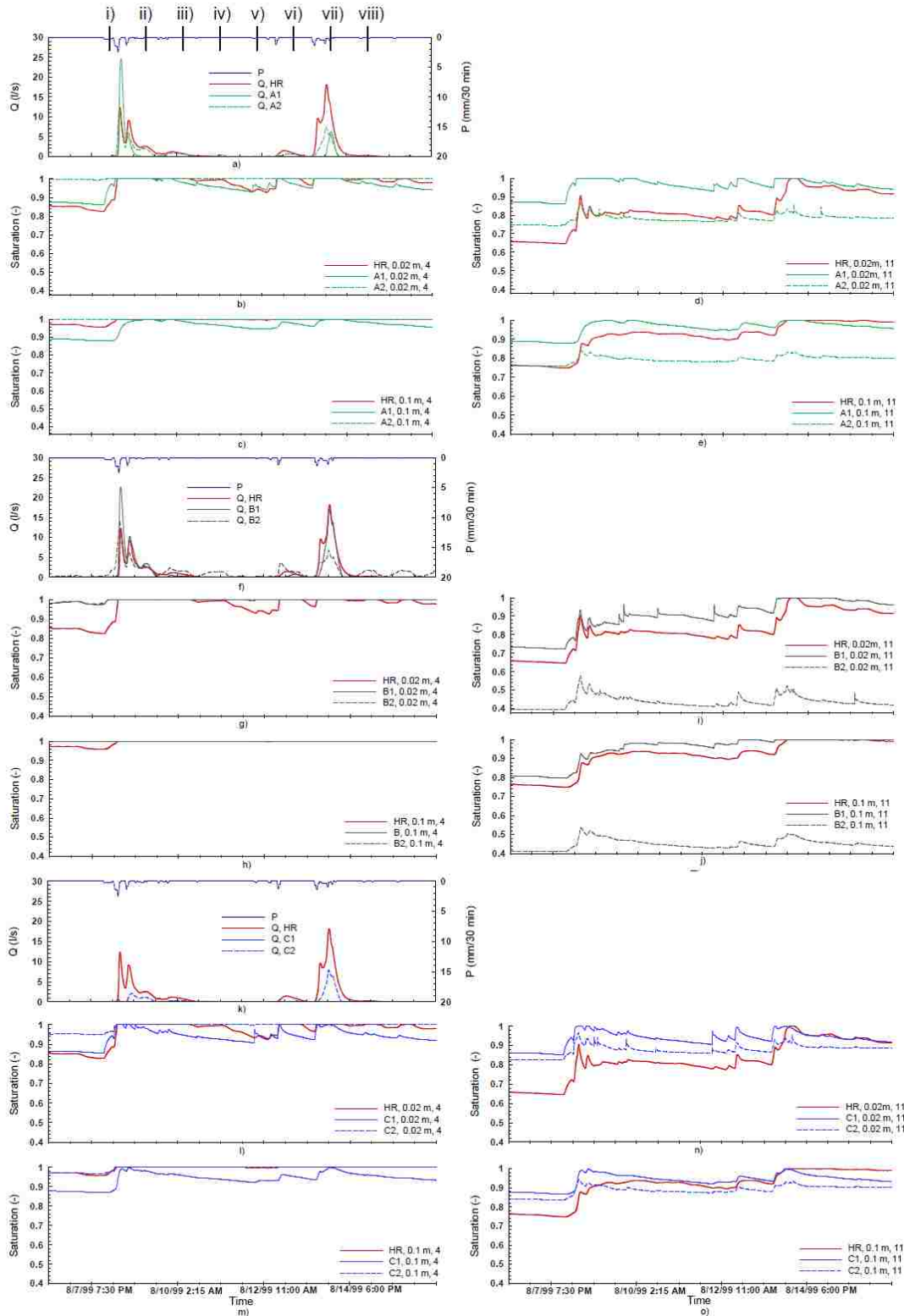


Figure 4.6 a), f), k) HR and A1, A2, B1, B2, C1, and C2 MODHMS hydrographs during the wet period A; b) - e), g) - j) and l) - o) HR and A1, A2, B1, B2, C1, and C2 MODHMS saturation at node 4 and node 11, depths 0.02 and 0.1 m.

The wet period A spatial distributions of saturation (Figure 4.7) show a wide range of soil moisture distribution patterns, that vary in both shape and magnitude across the catchment. For the more moisture retentive soils, such as the low K_{sat} clay loam and the silty clay (A1 and C1 scenarios), no discernable patterns were generated; these two scenarios have the lowest NSE values, estimated for both the entire evaluation period and for wet period A (Table 4.3), indicating an inappropriate soil parameterization for Tarrawarra. The high K_{sat} A2, and C2 scenarios saturation distributions show the typical soil moisture distribution pattern, with the water at or near saturation in the depressions, but for a smaller area than the HR (Figure 4.7); the near surface saturation variability is generally lower than for the HR and the upslope areas are wetter in both cases, with scenario C2 the wettest. MODHMS scenario B1 (loamy sand, low K_{sat}) spatial saturation distributions approximated best the HR near surface saturation, and consequently the integrated response of all scenarios investigated. A different soil moisture spatial distribution pattern was simulated for the high K_{sat} , B2 scenario, where water drained readily towards the depressions leaving the upslope area very dry (Figure 4.7).

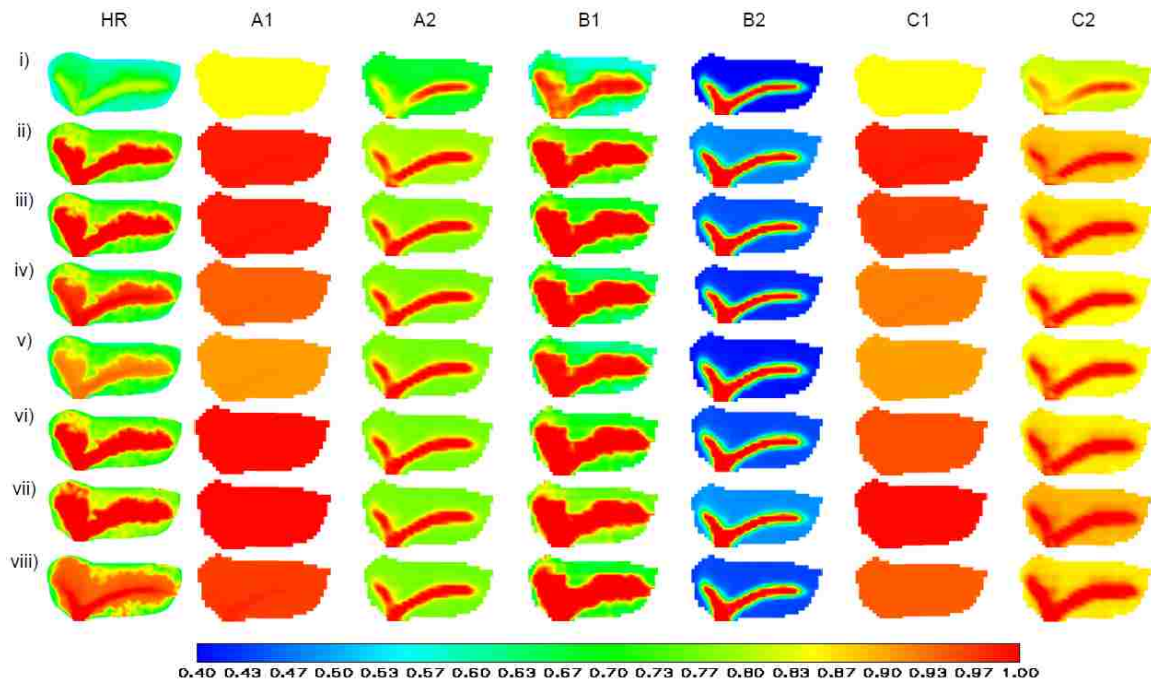


Figure 4.7 Spatial distribution of HR and A1, A2, B1, B2, C1 and C2 MODHMS saturation in the top 2 cm at 24 h interval, 8 August 1999, 0:00 AM to 15 August 1999, 0:00 AM during the wet period A.

4.4.5. MODHMS A1, A2, B1, B2, C1, and C2 scenarios, dry period B

During the dry period B, soil moisture varied with relatively little spatial variability across the catchment for all A1, A2, B1, B2, C1, and C2 scenarios, regardless of soil parameterization (Figures 4.8 and 4.9). The soil moisture magnitude varied between scenarios. In the case of the low K_{sat} clay loam and silty clay A1 and C1 scenarios the saturation level was relatively high after the first rain event and the catchment therefore reached saturation faster during the second high intensity storm, promoting high peak hydrographs during the summer period where no HR peaks occurred.

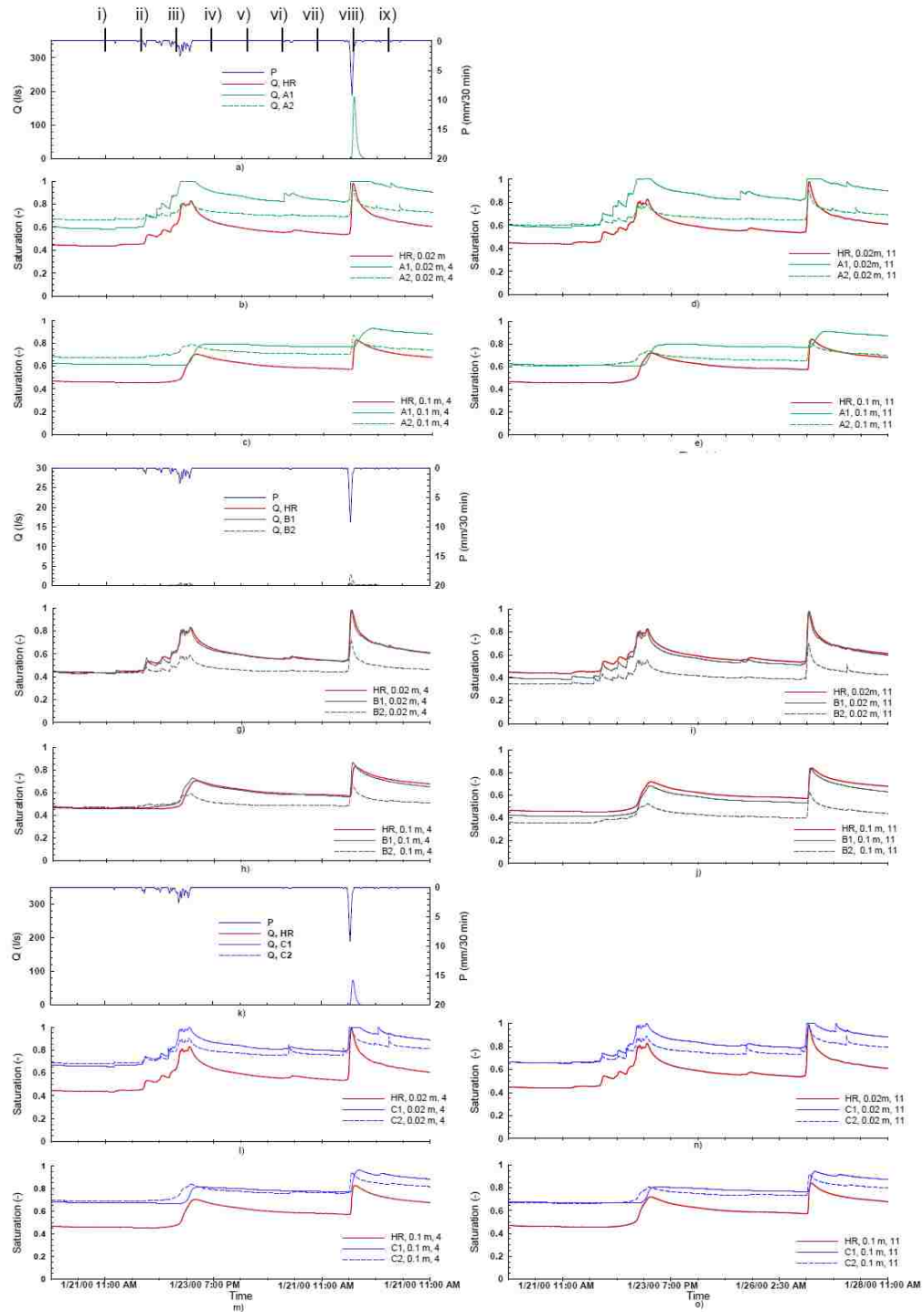


Figure 4.8 a), f), k) HR and A1, A2, B1, B2, C1, and C2 MODHMS hydrographs during the dry period B; b) - e), g) - j) and l) - o) HR and A1, A2, B1, B2, C1, and C2 MODHMS saturation at node 4 and node 11, depths 0.02 and 0.1 m.

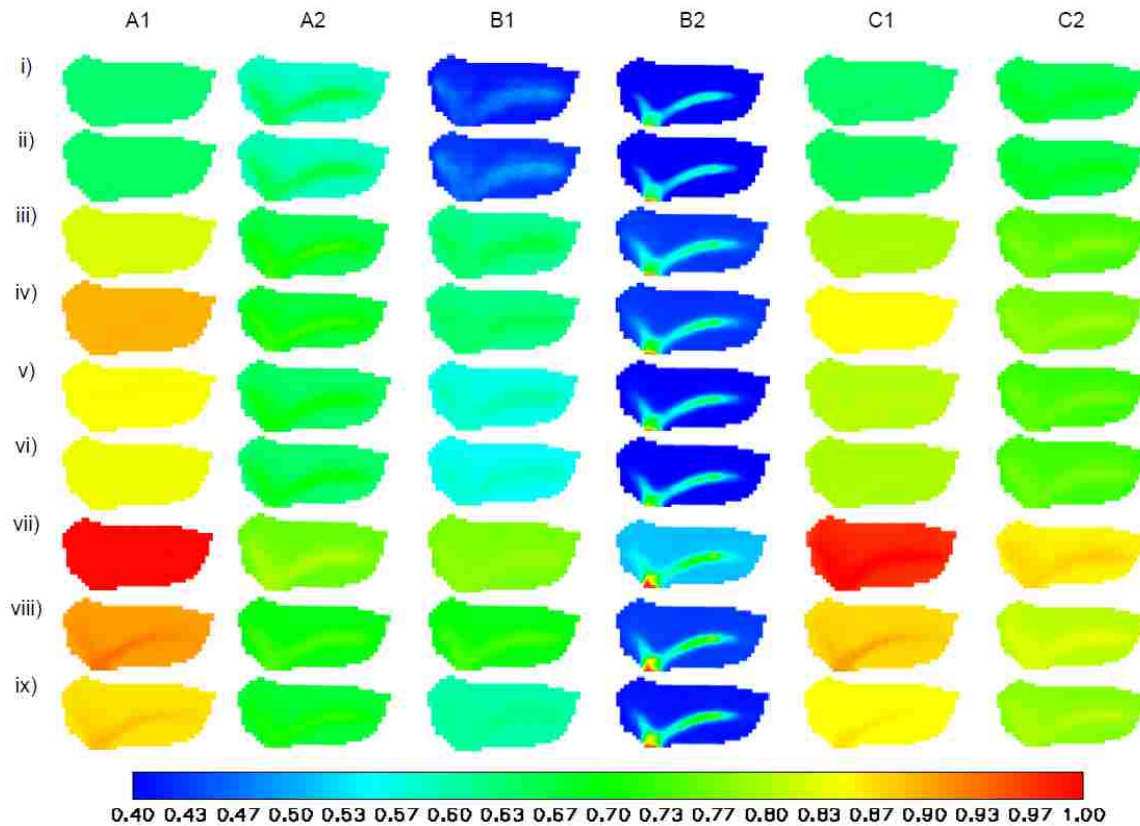


Figure 4.9 Spatial distribution of HR and A1, A2, B1, B2, C1, and C2 MODHMS saturation in the top 2 cm at 24 h interval, January 21 2000, 0:00 AM to January 29 2000, 0:00 AM during the dry period B.

4.5. Discussion

4.5.1. Influence of the soil moisture retention curve and saturated hydraulic conductivity on the near surface hydrologic response

The A, B, and C scenarios address the question of how does the shape of the soil moisture retention curve affect the MODHMS integrated response (discharge) and distributed response (soil moisture), assuming the same K_{sat} , soil porosity, soil depth, overland flow, and ET parameterization. Wet period A simulation results show that different curves affect the soil moisture spatial distribution patterns, which in turn, influence the hydrograph shape, timing, and magnitude (Figure 4.4). The loamy sand B scenario has a larger near saturation or saturated area adjacent to the depressions prior to the storms compared with the more water retentive A, and C scenarios (Figure 4.4 f); these soil hydraulic properties allow the water to move faster through the soil,

approximate better the HR spatial distribution of soil moisture, and generate timely runoff.

The first peak hydrograph of the wet period A, which was associated with dry initial conditions was simulated in the B scenario with higher magnitude than the HR but relatively adequate shape and timing, while in the A, and C parameterizations very little runoff was produced (Figure 4.4a). A second peak, associated with wetter, but not completely saturated initial conditions, was simulated for all A, B, and C scenarios; these hydrographs had smaller peak magnitudes than the HR and shifts in timing and shape. The more water retentive soils (A, and C) had generally higher levels of saturation, with less spatial variability across the catchment, however, their hydraulics allow for smaller and delayed peak hydrographs during wet period A when the surface soil was unsaturated.

In contrast with wet period A, during dry period B, when ET effects are more significant, there was very little spatial organization of soil moisture for all A, B, and C MODHMS scenarios (Figure 4.5 f). This behavior is consistent with field observations at Tarrawarra [Western *et al.*, 1999]. As expected, the van Genuchten parameters affected the saturation level of each scenario, with the loamy sand the driest, and silty clay the wettest, but patterns were not easily discernable following rain events (Figure 4.5 a-f).

The wet period A, A1, A2, B1, B2, C1, and C2 MODHMS simulations, addressing the sensitivity of K_{sat} for the same water retention curve, confirm the conclusions of several other studies [e.g., Binley *et al.*, 1989; Mirus, 2009] that the saturated hydraulic conductivity K_{sat} plays an important role in the spatial variability of soil moisture and for runoff generation. Figure 4.7 shows that a low K_{sat} tends to increase the area of the saturated region around the depressions and reduce the spatial variability of soil moisture across the catchment area during rain events, while a high K_{sat} is more favorable to pattern formation for all water retention curves. The combination of a “sandier” van Genuchten parameterization and high K_{sat} values tends to increase soil moisture spatial variability and favors pattern formation, while a more water retentive soil parameterization and low K_{sat} tends to maintain the soil wetter with less spatial variability. Figure 4.6 and Figure 4.7 show that K_{sat} appears to have greater influence on the level of saturation and pattern formation for a sandy soil parameterization and less influence for more water retentive soils.

The A2, and C2 scenarios illustrate the importance of adequately simulating the antecedent spatial distribution of soil moisture and the need for model parameterization evaluation under wet and dry season conditions and precipitation patterns and for both dry and wet periods within them. During wet period A, the A2 and

C2 scenarios saturation distributions captured, to a certain extent, the HR patterns, with lower spatial variability and generally higher moisture content (Figure 4.7). However, despite their NSE values of 0.61 and 0.40, respectively, during the wet period A, their overall performance for the entire evaluation period is poorer than the loamy case B, and B1 scenarios (Table 4.3). This is partly due to several peak hydrographs simulated during the intermediate dry period between the two wet seasons of the evaluation period (Figures not shown).

The antecedent conditions, expressed as level of soil saturation, influenced by soil parameterization, play a critical role for runoff generation during dry periods when storms have relatively high intensity and short duration. An example in Figures 4.8a, c and Figure 4.9 shows that more water retentive soils and lower K_{sat} values (A1, and C1 scenarios) tend to increase summer saturation and favor the simulation of peak hydrographs during high intensity summer rain events.

Dry period B, A, A1, A2, B1, B2, C1, and C2 simulation results show, that for the same water retention curve, the low and high K_{sat} values affect only the level of saturation across the catchment, and have little influence on soil moisture spatial variability and pattern formation (Figure 4.9). Figures 4.5f and 4.9 indicate that during the dry period, soil moisture spatial distributions are insensitive to both water retention curve shape and K_{sat} parameterization

4.5.2. Implications for model calibration

In many distributed model applications there is little or no information on soil, or soil water properties, and the problem of how to parameterize soil hydraulic properties remains subjective. The virtual experiments at Tarrawarra detailed in this study have illustrated a large range of catchment responses as a result of varying soil hydraulic parameters. In practice, model calibration of soil hydraulic parameters depends on the scale of the modeled domain. For larger areas, these parameters are typically established by the hydrological modeler based on generic soil information (data bases) and scarce (if any) field observations about the soil characteristics. The quality of information in the database and the domain spatial heterogeneity play an important role in model performance. At the small catchment spatial scale (e.g. Tarrawarra) model applications typically benefit more from model parameterizations based on field characterization of soil data, but the issue of spatial heterogeneity remains. For example, based on soil data collected at Tarrawarra, ROSETTA predicted a water retention curve similar to the average class for clay loam (Figure 4.2). However,

MODHMS scenarios showed that a more “sandier” behavior is needed to simulate soil moisture patterns similar to the HR and comparable appearance, timing, and peak magnitude of the hydrograph. Such a “sandier” curve can however lie in the clay loam class interval; the van Genuchten parameters vary within the same soil class (see example in Figure 4.2) and overlap between classes.

MODHMS tests illustrate the consequences of a plausible range of soil parameterization and underline the importance of behavioral parameterization. For gently sloping catchments such as Tarrawarra and for periods when the soil remains unsaturated and the water movement is controlled by soil hydraulics and topography, a potentially useful strategy would be to identify the behavioral shape of the soil moisture retention curve (based on the data base or field observed data) that controls the internal states and spatial patterns and then test the effects of K_{sat} on runoff during both dry and wet periods. For this approach, distributed soil moisture observations across dry and wet areas (or transects) at different depths are most useful. In some cases, the water retention parameters have little influence on the simulated hydrograph [e.g. *Vázquez et al.*, 2008] and only K_{sat} is calibrated. Other applications, however report sensitivities of the unsaturated parameters [e.g., *Christiaens and Feyen*, 2001; *Christiaens and Feyen*, 2002; *Mirus*, 2009]. The virtual experiments at Tarrawarra showed that soils with the most sensitive response have a “sandy” behavior of the soil moisture retention curve and high values of K_{sat} . For heterogeneous soils and larger domains this approach is more complicated due to the distributed nature of the parameter sets across the modeled domain.

Model scenarios investigated here support the conclusions of other studies (e.g. *Christiaens and Feyen* [2002]) that soil moisture measurements are critical for model soil parameterization. Distributed observations during both dry and wet periods and across dry and wet areas are especially informative to characterize the hydrologic behavior of ephemeral catchments. In addition to field data, remotely sensed soil moisture measurements are a promising source of information on pattern formation. Advances in soil moisture pattern analysis for calibrating distributed hydrologic models [e.g., *Wealands et al.*, 2005] show promise and need to be explored.

4.6. Summary and conclusions

We address two testing objectives related to configuration of soil parameters in a complex distributed hydrologic model: how does the shape of the soil moisture retention curve affect the integrated and distributed response, and what is the influence

of the saturated hydraulic conductivity for the same water retention curve? We select two different periods for closer investigation from the long term simulations: a wet period, characterized by cold weather patterns when the water movement through soil is controlled by the topography and soil hydraulics and a dry period, during which the soil is dry and the ET influence is more significant.

Simulation results show that the shape of the water retention curve, representing the nonlinear relationship between the pressure head and soil water content, influences the soil moisture spatial patterns, which in turn influence the timing, shape and magnitude of the simulated hydrograph. During wet periods when soil moisture patterns are forming, the more water retentive soils, such as clay loam, and silty clay, were less prone to pattern formation, had higher levels of saturation and less spatial variability and, overall, were less conducive to runoff generation than the sandier soil. For the same water retention curve, the saturated hydraulic conductivity K_{sat} plays an important role in both soil moisture spatial variability and runoff generation. More water retentive soils with low K_{sat} are more resistant to pattern formation, while sandy soils with high K_{sat} are more prone to pattern formation and have higher spatial variability. In general, low K_{sat} tends to decrease spatial variability of soil moisture and high K_{sat} to increase it. In contrast with the wet period when soil moisture patterns are forming, during the dry period very little spatial organization was simulated for all scenarios. During this period the water retention parameters and K_{sat} affect the level of saturation only, which is relatively uniformly distributed across the catchment, and are less influential for pattern formation and spatial variability.

We conclude that for gently undulating catchments such as Tarrawarra, for which the subsurface flow is important, the form of MODHMS parameterization of both soil moisture retention curve and saturated hydraulic conductivity K_{sat} are important for adequate representation of soil moisture patterns and timely runoff production. In this regard, if available, observed distributed hydrologic variables are valuable to assist a behavioral parameterization. The use of the hypothetical reality dataset opens the door for many other models, scenarios, and variables to be investigated in a hybrid approach, such as this work, between model testing and concept-development simulations of Mirus [2009] and Loague [2010].

4.7. References

Abbott, M. B., J. C. Bathurst, J. A. Cunge, P. E. O'Connell, and J. Rasmussen (1986a), An introduction to the European Hydrological System– *Système Hydrologique Européen*,

“SHE,” 1, History and philosophy of a physically based, distributed modelling system, *J. Hydrol.*, 87, 45– 59.

Abbott, M. B., J. C. Bathurst, J. A. Cunge, P. E. O’Connell, and J. Rasmussen (1986b), An introduction to the European Hydrological System– Système Hydrologique Européen “SHE,” 2, Structure of a physically-based, distributed modelling system, *J. Hydrol.*, 87, 61–77.

Allen, R.G., L.S. Pereira, D. Raes, M. Smith (1998), Crop Evapotranspiration: Guidelines for Computing Crop Water Requirements. FAO Irrigation and Drainage Paper 56. FAO, Rome, Italy, p. 300.

Anderton, S., J. Latron and F. Gallart (2002a), Sensitivity analysis and multi-response, multi-criteria evaluation of a physically based distributed model. *Hydrol. Process.* 16(2): 333–353.

Anderton, S., J. Latron, S. White, P. Llorens, M.C. Salvany, F. Gallart, and E. O’Connell (2002b), Internal validation of a physically-based distributed model using data from a Mediterranean mountain catchment. *Hydrology and Earth System Sciences* 6(1): 67–83.
Beven K. (1993), Profecy, reality and uncertainty in distributed hydrological modeling, *Advances in Water Resources*, 16, 41-51.

Beven K. (2006), A manifesto for the equifinality thesis. *J. Hydrol.* 320: 18–36.
Beven, K and A., Binley (1992), The future of distributed models—model calibration and uncertainty prediction. *Hydrol. Process.* 6:279–298.

Beven, K. (1989), Changing ideas in hydrology - The case of physically-based models. *J. Hydrol.*, 105:157-172.

Binley, A., K. Beven, and J. Elgy (1989), A physically based model for heterogeneous hillslopes. 2 Effective hydraulic conductivities, *Water Resour. Res.*, 25(6), 1219–1226.

Breuer, L., J.A., Huisman, P. Willems, H. Bormann, A. Bronstert, B.F.W. Croke, H. -G. Frede, T. Gräff, L. Hubrechts, A. J. Jakeman, G. Kite, J. Lanini, G. Leavesley, D.P.

Lettenmaier, G. Lindström, J. Seibert, M. Sivapalan and N. R. Viney (2009), Assessing the impact of land use change on hydrology by ensemble modeling (LUCHEM).I: Model intercomparison with current land use. *Advances in Water Resources*, 32 (2), 129-146.

Brooks, R.H. and A.T. Corey (1966), Properties of porous media affecting fluid flow, *J. Irrig. Drainage Div., Proc. ASCE*, IR 2.

Carpenter T.M. and K.P. Georgakakos (2006), Intercomparison of lumped versus distributed hydrologic model ensemble simulations on operational forecast scales, *J. Hydrol.*, 329, (1-4), 174-185.

Christiaens, K. and Feyen J. (2001), Analysis of uncertainties associated with different methods to determine soil hydraulic properties and their propagation in the distributed hydrological MIKE SHE model, *J. Hydrol.* 246, 63-81.

Christiaens, K. and Feyen J. (2002), Constraining soil hydraulic parameter and output uncertainty of the distributed hydrological MIKE SHE model using the GLUE framework, *Hydrol. Process.*, 16, 373-391, doi: 10.1002/hyp.335

Ebel, B.A. and K. Loague (2006), Physics-based hydrologic response simulation: Seeing through the fog of equifinality. *Hydrol. Process.*, 20, 2887-2900.

Ebel, B.A., K., Loague, D.R., Montgomery, and W.E. Dietrich (2008), Physics-based continuous simulation of long-term near-surface hydrologic response for the Coos Bay experimental catchment. *Wat. Resour. Res.*, 44: W07417, doi:10.1029/2007WR006442.

Feyen L, R., Vázquez, K., Christiaens O., Sels, J. Feyen (2000), Application of a distributed physically-based hydrological model to a medium size catchment, *Hydrology and Earth System Sciences* 4(1): 47–63.

Freeze, R. A., R.L. Harlan (1969), Blueprint for a physically-based, digitally-simulated hydrologic response model, *J. Hydrol.*, 9, 237-258.

Gan, T.Y. and S.J. Burges (1990), An assessment of a conceptual rainfall runoff model's ability to represent the dynamics of small hypothetical catchments: 2: Hydrologic responses for normal and extreme rainfall. *Water Resour. Res.* 26: 1605–1619.

Gottardi, G. and M.Venutelli (1993), A Control-Volume finite-element model for two dimensional overland flow, *Advances in Water Resources*, 16 277-284.

Grayson, R. B., and A. W. Western (1998), Towards area1 estimation of soil water content from point measurements: time and space stability of mean response. *J. Hydrol.* 207, 68-82.

Grayson, R. B., G. Bloschl, and I. D. Moore, Distributed parameter hydrologic modelling using vector elevation data: THALES and TAPESC (1995), in *Computer Models of Watershed Hydrology*, edited by V. P. Singh, pp. 669– 696, *Water Resour. Publ.*, Highlands Ranch, Colo.

Grayson, R. B., I. D. Moore, and T. A. McMahon (1992a), Physically based hydrologic modeling: 1. A terrain-based model for investigative purposes, *Water Resour. Res.*, 28, 2639– 2658.

Grayson, R.B., A.W. Western, F.H.S. Chiew and G. Blöschl (1997), Preferred states in spatial soil moisture patterns: local and non-local controls. *Wat. Resour. Res.* 33 (12), 2897–2908.

Grayson, R.B., I.D. Moore, and T.A., McMahon (1992b), Physically based hydrologic modeling, 2, Is the concept realistic? *Water Resour. Res.*, 28(10), 2659-2666.

Heppner, C.S., K. Loague and J. E., VanderKwaak (2007) Long-term InHM simulations of hydrologic response and sediment transport for the R-5 catchment, *Earth Surface Processes and Landforms*, 32, 1273-1292.

HydroGeoLogic (HGL) Inc., (2006), MODHMS (Version 3.0) - A MODFLOW-based Hydrologic Modeling System. Documentation and User's Guide, HydroGeoLogic Inc., Reston, Virginia.

Ivanov, V. Y., E. R. Vivoni, R. L. Bras, and D. Entekhabi (2004), Catchment hydrologic response with a fully distributed triangulated irregular network model, *Water Resour. Res.*, 40, W11102, doi:10.1029/2004WR003218.

Kampf, S. K., and S. J. Burges (2007a), A framework for classifying and comparing distributed hillslope and catchment hydrologic models, *Water Resour. Res.*, 43, W05423, doi:10.1029/2006WR005370.

Kampf, S.K. and S.J. Burges (2007b), Parameter estimation for a physics-based distributed hydrologic model using measured outflow fluxes and internal moisture states, *Water Resources Research* 43, W12414, doi:10.1029/2006WR005605.

Kristensen, K.J. and S.E. Jensen (1975), A model for estimating actual evapotranspiration from potential evapotranspiration. *Nordic Hydrology* 6, 170–188.

Loague, K., C.S. Heppner, B.A. Ebel, J.E. VanderKwaak (2010), The Quixotic search for a comprehensive understanding of hydrologic response at the surface: Horton, Dunne, Dunton, and the role of concept-development simulation. *Hydrol. Process.* 24, 2499-2505.

Loague, K.M. (1988), Impact of rainfall and soil hydraulic property information on runoff predictions at the hillslope scale. *Water Resour. Res.* 24: 1501–1510.

Maneta, M.P., S. Schnabel and V.G. Jetten (2008a), Continuous spatially distributed simulation of surface and subsurface hydrological processes in a small semiarid catchment, *Hydrol. Process.* 22, 2196-2214, doi:10.1002/hyp.6817.

Maneta, M.P., S. Schnabel, W.W. Wallender, S. Panday, and V.G. Jetten (2008b), Calibration of an evapotranspiration model to simulate soil water dynamics in a semiarid rangeland, *Hydrol. Process.* 22, 4655-4669, doi:10.1002/hyp.7087.

McDonald, M.G., and A. W. Harbaugh, A.W. (1988), A modular three- dimensional finite-difference ground-water flow model: U.S. Geological Survey Techniques of Water-Resources Investigations, book 6, chap. A1, 586 p.

Mirus, B.B. (2009), How does runoff begin (and end)? PhD Dissertation, Stanford University, Stanford, California, pp. 288.

Mirus, B.B., K. Loague, J.E. VanderKwaak, S.K. Kampf, and S.J. Burges (2009), A hypothetical reality of Tarrawarra-like hydrologic response. *Hydrological Processes* 23, 1093-1103. doi:10.1002/hyp.7241.

Mohanty, B.P., R.S. Bowman, J.M.H. Hendrickx, and M.T. van Genuchten (1997), New piecewise-continuous hydraulic functions for modeling preferential flow in an intermittent-flood-irrigated field, *Water Resour. Res.*, 33(9):2049-2063.

Monteith, J.L., (1981), Evaporation and surface temperature. *Q. J. R. Meteorol. Soc.* 107, 1–27.

Nash, J.E., and J.V. Sutcliffe (1970), River flow forecasting through conceptual models, Part I – A discussion of principles, *J. Hydrol.* (10), 282-290.

Panday, S., and P. S. Huyakorn (2004), A fully coupled physically-based spatially-distributed model for evaluating surface/subsurface flow, *Adv. Water Resour.*, 27, 361–382.

Park, S.J., N. van de Giesen (2004), Soil–landscape delineation to define spatial sampling domains for hillslope hydrology, *J. Hydrol.* 295, 28–46.

Perry M.A., J.D. Niemann (2007), Analysis and estimation of soil moisture at the catchment scale using EOFs, *J. Hydrol.*, 334: 388–404.

Perry M.A., J.D. Niemann (2008), Generation of soil moisture patterns at the catchment scale by EOF interpolation, *Hydrology and Earth System Sciences*, 12: 39–53.

Pincock, S. (2007), Climate politics: Showdown in a sunburnt country, *Nature* 450, 336-338, doi:10.1038/450336a.

Reed, S., V., Koren, M. Smith, Z. Zhang, F. Moreda, D.-J. Seo (2004), Overall distributed model intercomparison project results, *J. Hydrol.*, 298(1–4), 27–60.

Refsgaard, J. C. (1997). Parameterisation, calibration and validation of distributed hydrological models. *J. Hydrol.*, 198, 69-97.

Schaap, M.G., F.J. Leij and M.T. van Genuchten (1999), Bootstrap neural network approach to predict soil hydraulic parameters, In: van Genuchten M.T., F.J. Leij and L. Wu (Eds.), Proceedings of the international workshop on characterization and measurement of the hydraulic properties of unsaturated porous media: Riverside, California, 22-24 October 1997, 1237-1250.

Schoups, G., J. W. Hopmans, C. A. Young, J. A. Vrugt, and W. W. Wallender (2005), Multi-criteria optimization of a regional spatially-distributed subsurface water flow model. *J. Hydrol.*, 311(1-4), 20-48.

Senarath, S., F. Ogden, C. Downer, and H. Sharif (2000), On the Calibration and Verification of Two Dimensional, Distributed, Hortonian, Continuous Watershed Models, *Water Resour. Res.*, 36(6), 1495-1510.

Teuling, A.J., P.A. Troch (2005), Improved understanding of soil moisture variability dynamics, *Geophysical Research Letters*, 32: L05404, doi:10.1029/2004GL021935.

Teuling, A.J., R. Uijlenhoet, F. Hupet, E.E. van Loon, P.A. Troch (2006), Estimating spatial mean root-zone soil moisture from point-scale observations, *Hydrology and Earth System Sciences* 10: 755–765.

Thierfelder, T.K. R.B. Grayson, D. von Rosen, A.W. Western (2003), Inferring the location of catchment characteristic soil moisture monitoring sites. Covariance structures in the temporal domain. *J. Hydrol.*, 280, 13–32.

Troch, P.A., M. Mancini, C. Paniconi, and E.F. Wood (1993). Evaluation of a distributed catchment scale water balance model. *Water Resour. Res.* 29(6), 1805-1817.

van Genuchten M. T. (1980), A closed-form equation for predicting the hydraulic conductivity of unsaturated soils. *Soil Sci.Soc. Am. J.*, 44, 892-898.

VanderKwaak, J. E. (1999), Numerical simulation of flow and chemical transport in integrated surface-subsurface hydrologic systems, Univ. of Waterloo, Waterloo, Ont., Canada.

Vázquez, R., P. Willems and J. Feyen (2008) Improving the predictions of a MIKE SHE catchment scale application by using a multi-criteria approach, *Hydrol. Process.*, 22, 2159-2179.

Vrugt, J.A., G. Schoups, J.W. Hopmans, C. Young, W.W. Wallender, T. Harter and W. Bouten (2004), Inverse modelling of large-scale spatially distributed vadose zone properties using global optimization, *Water Resour. Res.* 40 (6) Art. No. W06503.

Wealands, S. R., R. B. Grayson and J. P. Walker (2005). Quantitative comparison of spatial fields for hydrological model assessment – some promising approaches, *Advances in Water Resources* 28, 15–32.

Weiler, M. and J.J. McDonnell JJ (2004), Virtual experiments: a new approach for improving process conceptualization in hillslope hydrology, *J. Hydrol.* 285, 3–18.

Werner A. D., M.R. Gallagher, S.W. Weeks (2006), Regional-scale, fully coupled modeling of stream-aquifer interaction in a tropical catchment. *J. Hydrol.* 328, (3-4), 497-510.

Western, A., W. and R. B., Grayson (1998), The Tarrawarra data set: soil moisture patterns, soil characteristics and hydrological flux measurements, *Water Resour. Res.* 34:1010, 2765-2768.

Western, A.W., G. Blöschl, and R.B. Grayson (1998a), Geostatistical characterisation of soil moisture patterns in the Tarrawarra catchment, *J. Hydrol.* 205, 20-37.

Western, A.W., G. Blöschl, and R.B. Grayson (1998b), How well do indicator variograms capture the spatial connectivity of soil moisture? *Hydrol. Process.* 12, 1851-1868.

Western, A.W., G. Blöschl, and R.B. Grayson (2001), Toward capturing hydrologically significant connectivity in spatial patterns. *Wat. Resour. Res.* 37(1), 83-97.

Western, A.W., R.B. Grayson and T.R. Green (1999), The Tarrawarra project: high resolution spatial measurement, modelling and analysis of soil moisture and hydrologic response. *Hydrol. Process.* 13. 633–652.

Wigmosta, M. S., B. Nijssen, P. Storck, and D. P. Lettenmaier (2002), The distributed hydrology soil vegetation model, in *Mathematical Models of Small Watershed Hydrology and Applications*, edited by V. P. Singh, pp. 7 –42, *Water Resour. Publ.*, Highlands Ranch, Colo.

Wigmosta, M. S., L. W. Vail, and D. P. Lettenmaier (1994), A distributed hydrology-vegetation model for complex terrain, *Water Resour. Res.*, 30, 1665– 1679.

Wilson D.J., A.W. Western, R.B. Grayson (2004), Identifying and quantifying sources of variability in temporal and spatial soil moisture observations, *Wat. Resour. Res.* 40: W02507, doi:10.1029/2003WR002306.

Wu, S., J. Li, G.H. Huang (2007) Modeling the effects of elevation data resolution on the performance of topography-based watershed runoff simulation, *Environmental Modelling & Software* 22, 1250- 1260.

Young, C., W. Wallender, G. Schoups, G. Fogg, B. Hanson, T. Harter, J. Hopmans, R. Howitt, T. Hsiao, S. Panday, K. Tanji, S. Ustin, K. Ward (2007), Modeling shallow water table evaporation in irrigated regions, *Irrig Drainage Syst*, 21, 119-132, doi: 10.1007/s10795-007-9024-4.

Zehe E., H. Lee, and M. Sivapalan (2006): Dynamical process upscaling for deriving catchment scale state variables and constitutive relations for meso-scale process models, *Hydrology and Earth System Sciences*, 10, 981-996.

Acknowledgments

We thank Ben Mirus for generating the Tarrawarra hypothetical reality dataset. This research was funded by NSF Grant (NSF – EAR-0537410).

Appendix 4A

The three-dimensional variably-saturated subsurface and the surface flow equations that are solved numerically by MODHMS are:

$$\frac{\partial}{\partial x} \left(K_{xx} k_{rw} \frac{\partial h_G}{\partial x} \right) + \frac{\partial}{\partial y} \left(K_{yy} k_{rw} \frac{\partial h_G}{\partial y} \right) + \frac{\partial}{\partial z} \left(K_{zz} k_{rw} \frac{\partial h_G}{\partial z} \right) - W + q_{go} + q_{gc} = \phi \frac{\partial S_w}{\partial t} + S_w S_s \frac{\partial h_G}{\partial t} \quad (A1)$$

$$\frac{\partial h_o}{\partial t} - \frac{\partial}{\partial x} \left(dk_x \frac{\partial h_o}{\partial x} \right) - \frac{\partial}{\partial y} \left(dk_y \frac{\partial h_o}{\partial y} \right) - dq_{og} - dq_{oc} = 0 \quad (A2)$$

where: K_{xx} , K_{yy} , and K_{zz} are the principal hydraulic conductivities in the x , y , and z directions, respectively [$L T^{-1}$]; k_{rw} is the relative permeability, a function of water saturation; h_G is the hydraulic head of the subsurface flow system defined as $h_G = \psi + z$, where ψ is the pressure head [L] and z is the gravitational head [L], with z defined positive upwards; W represents the flux per unit volume of sources or sinks of water [T^{-1}]; q_{go} is the flux per unit volume to the subsurface from the 2-D overland flow domain [T^{-1}]; q_{gc} is the flux per unit volume to the subsurface from the 1-D channel or surface water feature domain [T^{-1}]; ϕ is the porosity; S_w is the water saturation estimated from the moisture retention curve as a function of the pressure head; S_s is the specific storage of the porous media [L^{-1}]; and t is time [T].

In Eq.A2 $h_o = z_o + d$ is the water surface elevation [L]; d is the flow depth; z_o is the surface elevation [L]; q_{og} is the flux per unit volume from surface to subsurface, with $q_{go} = -q_{og}$, [T^{-1}]; q_{oc} is the flux per unit volume of overland flow from the channel [T^{-1}]; k_x and k_y are conductance terms [LT^{-1}], derived by *Gottardi and Venutelli* [1993].

In Eq.A1, when the saturation S_w equals 1, the equation solves the 3-D flow for the fully saturated domain. The S_w derivative with time is eliminated from the first term of the left hand side of Eq.A1 and Eq.A1 becomes equivalent to the equation used to describe the fully saturated groundwater flow originally implemented in MODFLOW [McDonald and Harbaugh, 1988]. The surface characterized by $S_w = 1$ is the position of the water table.

The *van Genuchten* [1980] formulation for both k_{rw} and pressure heads ψ as functions of water saturation are Eq. A3 and Eq. A4:

$$k_{rw} = S_e^{1/2} e^{\left[1 - (1 - S_e^{1/\gamma})^\gamma\right]^2} \quad (A3)$$

$$S_e = \frac{S_w - S_{wr}}{1 - S_{wr}} = \begin{cases} \frac{1}{\left[1 + (\alpha \psi)^\beta\right]^\gamma}, & \psi < 0 \\ 1 & \psi \geq 0 \end{cases} \quad (A4)$$

where k_{rw} is the relative permeability, S_e is the effective water saturation, S_w is the water saturation, equal to the water content ϑ divided by porosity Φ , S_{wr} is the residual water saturation, equal to the residual water content ϑ_r divided by porosity Φ , α and β are empirical, fitting parameters and $\gamma = 1 - 1/\beta$. Eq. A4 is the functional form of the soil moisture retention curve.

Chapter 5. Modeling how vegetation cover affects climate change impacts on streamflow timing and magnitude in the upper Tuolumne Basin, Sierra Nevada

Abstract

Many studies have shown that onset of snow-melt based streamflow occurs earlier in the spring in North America due to warming temperatures. However, the role vegetation cover plays in the rate of advance has been less investigated. In the Tuolumne river basin of the Sierra Nevada, California, most river water is provided by high elevation snowmelt. This water is especially important during summer conditions for mountain ecosystems and for downstream water supply. We investigated, through hydrologic modeling, the impact of the extent and density of canopy cover on the rate of streamflow timing on the peak and late summer flows in the upper Tuolumne basin (2,600-4,000 m) of the Sierra Nevada. We used the Distributed Hydrology Soil Vegetation Model (DHSVM) for the hydrologic modeling of the basin, assuming four vegetation scenarios: current forest (partial cover, 80% density), all forest (uniform coverage, 80% density), barren, and thinned forest (partial cover, 40% density) for a medium-high emissions scenario (A2) from the Geophysical Fluid Dynamics Laboratory (GFDL) CM2.1 model. Significant advances in streamflow timing, quantified as the center of mass, COM, of over one month were projected for all vegetation scenarios. However, there were differences between these scenarios for the same climate dataset from the GFDL CM2.1 model. When forest covered the entire area, the COM occurred on average 12 days earlier, with the rate of advance higher by about $0.06 \text{ days}\cdot\text{year}^{-1}$ over 100 years compared to the case assuming current forest coverage. On average, over the 100-year period the all forest peak and late summer flows were lower by about 20% and 27%, respectively compared to the corresponding values for the current forest scenario. Under barren and reduced canopy cover conditions the COM occurred later by about 7 and 5 days, respectively, with lower rates of COM advance and 19% higher peak and 23% higher late summer flows in the barren case, and 13% higher peak flows and 9% higher late summer flows in the case of thinned forest compared with the current forest scenario over the simulation period. Peak summer flows decreased with increasing temperatures in time by 22%, 27%, 16% and 18% for the current forest, all forest, barren and thinned forest, respectively. Examination of modeled changes in energy balance components at forested and barren sites when temperature is increasing indicated that increases in net longwave radiation are higher in the forest case and have a higher contribution to melting earlier in the season when shortwave radiation is smaller. These increases contributed to increased midwinter melt at temperatures above freezing and caused decreases in accumulation, and faster melt rates. The higher accumulation at barren sites increased snowpack retention and had the potential to decrease the rate of streamflow advance to earlier dates and to increase summer flows in the Tuolumne basin.

5.1. Introduction

Mean timing of snowmelt runoff has advanced by approximately 1-3 weeks in many mountainous catchments across western North America (Stewart *et al.* 2005; Regonda *et al.*, 2005). This trend toward earlier snowmelt and earlier streamflow timing has been attributed to the broad-scale increase of winter and spring temperatures by about 1°–3°C over the past 50 years (Stewart *et al.*, 2005). These changes appeared to be sensitive to the effects of increased air temperature, primarily in basins below about 2500 m (Regonda *et al.*, 2005), and are expected to continue in the future, due to anticipated climate change effects (Leung and Wigmosta 1999; Hamlet and Lettenmaier, 1999; Leung *et al.*, 2004).

In addition to climate, vegetation cover type and extent also affect streamflow patterns (Jones and Post, 2004), and watershed managers have options in how they choose to manage the vegetation cover to control streamflow patterns (Grant *et al.*, 2008). Therefore, the role vegetation plays in the magnitude of these changes in a warming climate is of interest. Forests interact with snow through altering its spatial distribution and energy exchanges with the environment. Forests reduce ground-level incoming shortwave radiation while increasing longwave radiation (Hardy *et al.* 2004; Link *et al.* 2004; Boon, 2009), and reduce turbulent energy transfer at the snow surface (Hardy *et al.* 1997). The absence of vegetation causes snow accumulation and melt rates to increase and evapotranspiration to decrease (Whitaker *et al.*, 2002). Melt rates were found generally to be higher in the barren areas than under the forest in Canada (Boon, 2009; Burles and Boon 2011; Winkler *et al.*, 2005). However, differential snowmelt rates between the barren regions and the forest may vary with elevation. At lower elevation, snowmelt rates in Canadian forests were lower than in the clear-cut areas, whereas at higher elevation, snowmelt rates of forested and barren areas approached equality (Whitaker *et al.*, 2002). At temperatures above freezing, melt rates were higher under the forest, but at near-freezing temperatures melt rates in the barren areas were higher in the central Pyrenees; these differences were attributed to increased net longwave radiation at temperatures above 0°C, and to the lower albedo under the forest (López-Moreno and Latron, 2008).

The effects of vegetation changes on streamflow have long been investigated due to their economical and ecological importance. Historically, paired watershed experiments have evaluated forest harvesting effects on the magnitude of peak summer flows (Hewlett, 1971; Hewlett, 1982; Robinson *et al.*, 2003; Jones and Post, 2004; Andréassian, 2004; Grant *et al.*, 2008). In general, changes in streamflow as a result of vegetation disturbance varied with the nature of basin, vegetation type, elevation and climate, but in most cases higher peak flows have been reported in the clear cut basins compared with control vegetated basins. More recently, in addition to paired watershed

studies, hydrologic modeling has been used as a means of identifying changes in the magnitude and frequency of the peak flows in response to vegetation cover changes (e.g., Schnorbus and Alila, 2004; Alila *et al.*, 2009; Cuo *et al.*, 2009; Kuraś *et al.*, 2012). Hydrologic modeling allows for comparisons of streamflow time series generated assuming different land cover scenarios, while maintaining the same climatic and precipitation patterns (same model forcing data). In these modeling experiments, partial or total removal of forest canopies was found to increase both the magnitude and frequency of annual peak discharge in watersheds located in British Columbia, Canada (Schnorbus and Alila, 2004; Kuraś *et al.*, 2012).

In this study we use hydrologic modeling to explore the role of vegetation on streamflow timing and magnitude under a warming climate for the upper Tuolumne River basin of the Sierra Nevada, California. The regional hydrology is very important for California water, as part of the Tuolumne River snowmelt is stored in the downstream Hetch Hetchy reservoir, which is a major component of the San Francisco water supply system. The timing of snowmelt and the amount of water available are therefore of great interest for resource managers concerned with water supply for agricultural, urban and industrial use. Previous studies of Sierra Nevada basins have shown that streamflow timing will likely occur earlier as a result of climate change, leading to longer periods of lower flows during the summer, when water is most needed (Maurer *et al.*, 2007; Null *et al.*, 2010). These prolonged low flow conditions are detrimental not only for downstream water supply but also to the region's mountain ecosystems (Lowry *et al.*, 2010; Lowry *et al.*, 2011).

The upper Tuolumne River basin drains to Tuolumne Meadows, where the stream depths are closely linked to groundwater levels and distributions of meadow vegetation (Loheide *et al.*, 2009; Loheide and Lundquist 2009; Lowry *et al.* 2011). Meadow vegetation, and associated restoration strategies are intimately tied to local stream hydrographs, which in turn, are controlled by integrated processes across their contributing watershed (Lowry *et al.* 2011). Park managers developing long-term conservation plans are interested in how climate warming is likely to affect the meadow hydrology.

To address this question, we use the Distributed Hydrology Soil Vegetation Model (DHSVM, Wigmosta *et al.* 1994) to simulate historic and projected future streamflows and additionally to explore how the vegetation cover influences streamflow timing and magnitude. Within the model, we create virtual experiments by specifying different vegetation scenarios to emulate paired watershed experiments, while applying the same future meteorology from a medium-high emissions scenario, A2 (IPCC, 2001) of the Geophysical Fluid Dynamics Laboratory (GFDL) CM2.1 model.

DHSVM explicitly models the effects of shading and vegetation cover, and has previously been applied to evaluate effects on streamflow patterns from climate change (Leung and Wigmosta 1999; Battin *et al.*, 2007; Wiley and Palmer, 2008) and forest harvesting

(Whitaker *et al.*, 2002; Schnorbus and Alila, 2004; Kuraś *et al.*, 2012). In a review of hydrologic models for applications studying forest management and climate change, DHSVM was identified to be the most suitable model to address questions related to forest effects on streamflow (Beckers *et al.* 2009). The model was previously applied in the upper Tuolumne river basin to simulate boundary conditions that were then used as input in a groundwater model to evaluate hydrologic conditions for the Tuolumne Meadows ecology (Lowry *et al.* 2010; Lowry *et al.* 2011).

We chose the upper Tuolumne area as a case study for this investigation because: i) it is a high elevation basin important for providing snowmelt water during the critical summer low flow conditions, ii) the basin is sensitive to changes in climate which will affect the meadow ecology, and, iii) forest cover manipulation was identified as a means to increase snow retention in other high elevation regions of the Sierra Nevada (e.g. Bales *et al.*, 2011b). Streamflow series derived from four different vegetation scenarios and the same climate scenario from the GFDL CM2.1 model were analyzed for changes in timing, peak magnitude and frequency, and summer low flow magnitude and frequency. These stream flow metrics are important for the meadow ecology and for downstream reservoir management. The main purpose of this analysis was to determine how land cover affects the basin sensitivity to climate change (i.e. is a forested basin more or less sensitive than a barren basin?). Section 2 of this paper describes the study site, Section 3 provides details on models and methods, Section 4 discusses the results and implications, and Sections 5, and 6 provide a summary of the findings, and conclusions, respectively.

5.2. Study site and data sources

The upper Tuolumne basin, located in Yosemite National Park in the Sierra Nevada of California is a high elevation basin, ranging from 2600 to 4000m above sea level (Figure 5.1). Its area of 186 km² comprises about 16% of the downstream Hetch Hetchy reservoir's drainage area. The underlying soils are thin (typically less than 1m deep) and are derived from low permeability intrusive rocks (granodiorite), which erode slowly and interact little with streamflow (Huber, 1987). High elevation, complex topography, and low infiltration make the system snowmelt dominated. The climate is Mediterranean, with cold and wet winters and warm and dry summers. Over 80-90% of annual precipitation (800-1000mm) falls as snow, but there is significant seasonal and inter-annual variability in precipitation (Epke *et al.*, 2010). The basin is covered at lower elevations by dense forest (*Pinus contorta*, 39% of the total basin area) and by herbaceous meadow vegetation (meadow, 36%), and is barren (granitic bedrock, 24%) at higher elevations (Figure 5.1).

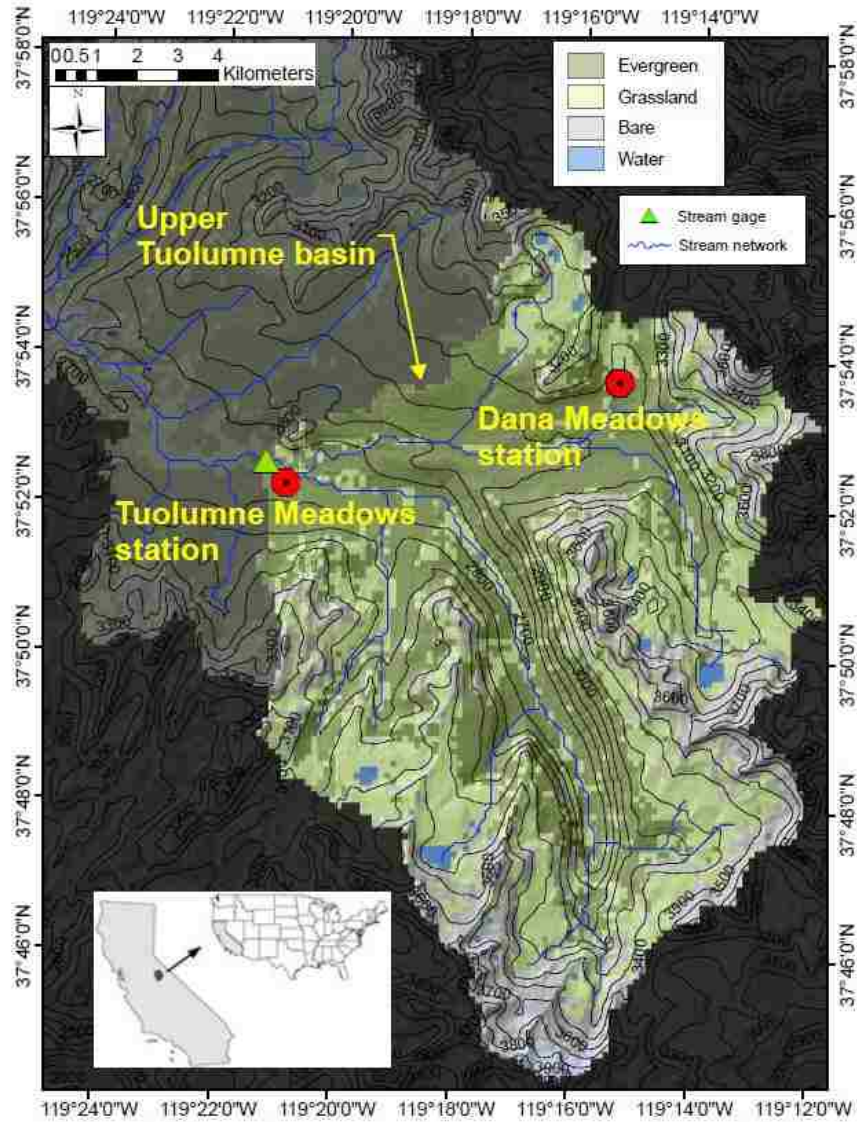


Figure 5.1 Upper Tuolumne basin, Sierra Nevada, California.

Streamflow data were collected as part of the Yosemite Hydroclimate Monitoring Project beginning in August of 2001 (Lundquist *et al.* 2003; Lundquist *et al.* 2004). Stream stage was manually measured during the summer season, and was also recorded half-hourly with Solinst Levellogger © pressure transducers at the location shown as a solid triangle in Figure 5.1. Observed stream stage timeseries were transformed into streamflow using rating curves relating water level to discharge calculated from manual measurements (Rantz *et al.*, 1982).

The 2003-2009 period used for model calibration experienced a relatively large range of climate conditions and hydrologic variability which is representative of the region. An analysis of the long-term historic streamflow record (1916-2009) in the neighboring Merced basin (United States Geological Survey, USGS, gage 11264500) showed that the

2003-2009 period encompassed conditions ranging between the 9th percentile (2007, the driest year) and 95th percentile (2008, the wettest year). Meteorological data were obtained from the Dana Meadows (Lat: 37.9°N, Long: 119.3°W, 2966 m) and Tuolumne Meadows (Lat: 37.6°N, Long: 119.7°W, 2600 m) snow pillow sites (Figure 5.1), which are managed by the California Department of Water Resources.

5.3. Hydrologic modeling, climate data, and methods for streamflow analysis

5.3.1. Hydrologic model description and model set-up

The Distributed Hydrology Soil Vegetation Model, DHSVM, calculates the full surface energy balance independently at each model grid cell, including terrain shading effects, radiation attenuation, wind modification, and snow-canopy processes (Wigmosta *et al.* 1994; Storck 2000; Storck *et al.* 2002). DHSVM represents the seasonal snowpack as a two-layer system, and solves the full surface energy balance at each time step. The surface (top) layer actively exchanges energy and mass with the atmosphere. The pack (bottom) layer acts as a mass and energy reservoir and exchanges inputs of heat and melt water with the surface layer.

Vegetation is represented in DHSVM as a two-level coverage, with the overstory covering a specified fraction of the pixel, typically the canopy closure, and an understory. Interception is modeled as a function of precipitation and snow interception efficiency, until a maximum value is reached. Intercepted snow is subject to sublimation, mass release from the canopy (added to the snowpack as rain), and melt (estimated through an energy balance equation). Evapotranspiration is represented by the Penman-Montieth approach (Shuttleworth, 1992), assumed to occur at the potential rate from the wet surfaces and dependent on the soil moisture under unsaturated conditions. Calculations of evapotranspiration are based on weather variables, aerodynamic resistance (dependent on the wind velocity profile and vegetation characteristics), and canopy resistance (dependent on temperature, vapor pressure deficit, photosynthetically active radiation and soil moisture). Above the overstory a logarithmic (flat plate boundary) wind profile is assumed, whereas through the overstory and understory wind decreases exponentially until it meets a new (lower velocity) logarithmic profile near the surface (Wigmosta *et al.*, 1994). DHSVM simulates overland flow and both saturated and unsaturated subsurface flow. Streamflow is routed through a network in which each stream section is treated as a linear reservoir using a Muskingum-Cunge algorithm. Model equations representing the snowpack energy balance are given in Appendix 5A. Additional model details and conceptualization of hydrologic processes and model equations are described in Wigmosta *et al.*, 1994 and Wigmosta *et al.* 2002, and summarized in several subsequent

studies in which DHSVM was used (e.g. Thyer *et al.* 2004; Jost *et al.* 2009 or Bewley *et al.* 2010).

For the upper Tuolumne basin, DHSVM was run at a three-hour time step with a 150-m grid resolution. This resolution was chosen to best resolve the stream networks and water transfers between grid cells, while remaining coarse enough to maintain computational efficiency. Spatial inputs of elevation, vegetation, soil type and depth, geology, and terrain shading were pre-processed from available NPS and USGS datasets. Temperature was distributed across the basin with a constant lapse rate of $-6.5^{\circ}\text{C km}^{-1}$, which was the average found from a distributed network of over 40 sensors in this region (Lundquist and Cayan, 2007). Precipitation was distributed using relative weighting derived from maps of monthly climate normal precipitation from the Parameter-elevation Regressions on Independent Slopes Model (PRISM; Daly *et al.* 1994; Daly *et al.* 2002; Daly *et al.* 2008). Forest coverage (Figure 5.1) was represented as a single class (conifers, predominantly lodgepole pine *Pinus contorta*,) of uniform 80% fractional coverage (of the pixel). Vegetation parameters have been established based on data from personal communications with park managers and from the literature, primarily from studies that applied DHSVM at sites where lodgepole pine forests were present (e.g. Thyer *et al.*, 2004; Bewley *et al.*, 2010). Model parameters are given in Table 1.A1, Appendix 5A.

Temperature, relative humidity, incoming shortwave radiation, and wind speed data used for calibrating the model for years 2003-2009 were recorded at Dana Meadows (Figure 5.1). Because the precipitation data record at this station was affected by instrument failure during 2006 to 2009, we used precipitation measured at Tuolumne Meadows (Figure 5.1), which was scaled by a factor of 1.3 to match the Dana Meadows records. Thus, PRISM precipitation weights were referenced to the Tuolumne Meadows site location. The factor of 1.3 matched the ratio of the two stations during the years of overlap. The air temperature lapse rate ($-6.5^{\circ}\text{C km}^{-1}$) was checked through lapsing the air temperature recorded at Tuolumne Meadows and comparing it to air temperature recorded at Dana Meadows. This comparison revealed a relatively uniform scatter around the 1:1 line and indicated that this lapse rate is suitable for representing air temperature distribution across the upper Tuolumne basin. In addition to this comparison, and given the importance of varying temperature with elevation, we also examined the model's sensitivity to constant lapse rates of $-4.5^{\circ}\text{C km}^{-1}$ and $-8.5^{\circ}\text{C km}^{-1}$, relative to the base case of $-6.5^{\circ}\text{C km}^{-1}$. Although variations in lapse rates have been found to affect basin hydrology in other basins (e.g., Minder *et al.* 2010), varying the lapse rate had little effect on streamflow in our study area because the overall elevation range in the basin is relatively small, and the forcing temperature is located near the middle of the overall range (Figure 5.1). The $-8.5^{\circ}\text{C km}^{-1}$ lapse rate resulted in slight increase/decrease in late-season discharge, and a shift of ± 2 days in COM. Therefore, we kept the lapse rate constant at $-6.5^{\circ}\text{C km}^{-1}$, which was found to better represent temperature variations with elevation for all further simulations.

Incoming shortwave radiation was distributed using solar geometry calculations, then corrected for terrain shading effects using monthly maps of terrain shadowing constructed using the solar geometry from day 15 of each month (Wigmosta *et al.* 1994). Soil saturated hydraulic conductivity values were estimated using the USDA soil classifications (USDA NRCS 2006) and mean saturated conductivity values provided by Carsel and Parrish (1988) for each soil class (Table 1.A1, Appendix 5A). During preliminary sensitivity tests, these were varied by one order of magnitude (both higher and lower), but model results were relatively insensitive to these variations. Soil depths were checked during field visits and found to be less than 1m in most locations and less than 3m in most meadow locations, which is consistent with reported values (USDA NRCS 2006) and those used in DHSVM (Lowry *et al.*, 2010). Forest parameters were set to 80% fractional coverage, 5.0 leaf-area-index (LAI), and 30% radiation attenuation (k , Eq. A5, Appendix 5A) based on park vegetation surveys, discussions with park foresters, and values reported in the literature (Table 1.A1, Appendix 5A). Additional discussion of model parameter sensitivity is provided in Appendix 5A.

The stream network was developed from a hydrologically-conditioned 150-m DEM; small (1-3 m) adjustments to individual elevation pixels were made to force the derived stream network to match the NPS stream map, which was developed from site surveys. These adjustments were necessary because some streams in the area are routed via incised bedrock channels that are not represented on a 150-m DEM. Modeled streamflow was routed at each time step using the stream channel network, with each stream section treated as a linear reservoir. Water also entered the channel via overland flow and saturated subsurface flow in the soil layers. Because the majority of the basin is made up of intrusive igneous granodiorite, influences from deep groundwater were negligible.

5.3.2. Climate data and model scenarios

To explore potential changes in the basin hydrology as a result of increasing temperature and as a function of vegetation cover, we performed two types of simulations. First we ran model ΔT sensitivity tests on the historical record and then we used long-term climate data based on output from Geophysical Fluid Dynamics Laboratory (GFDL) CM2.1 model (Stouffer *et al.* 2006; Delworth *et al.* 2006; Knutson *et al.* 2006). For the ΔT temperature sensitivity tests we considered the two extreme vegetation scenarios, forest and barren, for the historic 2003-2009 period. The temperature was raised by $\Delta T = 3^\circ\text{C}$ in the forcing dataset, and the results were compared with the simulations run using the historic meteorology. This ΔT was chosen to represent the approximate temperature increase by the last decades of the century in the GFDL scenario. The purpose of running the ΔT sensitivity tests (model scenarios 1-4, Table 5.1) was to allow comparisons of the energy balance components, snow water

equivalent (SWE) and streamflow between forested and barren cases for the historic temperature T and increased, historic T + 3°C forcing data.

Table 5.1 DHSVM scenarios for ΔT sensitivity tests.

Scenario	Vegetation cover	Scenario assumptions
1	All forest	Historic T
2	All forest	Historic T + 3°C
3	Barren	Historic T
4	Barren	Historic T + 3°C

The climate scenario is a medium-high emissions scenario (A2) from the GFDL model that assumes emissions increase continuously to near 30 Gt yr⁻¹ by 2100 (IPCC 2001). This scenario was chosen to be compatible with other climate impacts studies in the region, and was identified as appropriately representing plausible future conditions in California (e.g. Maurer 2007; Cayan *et al.*, 2008). We initially considered a range of four climate scenarios based on the Parallel Climate Model, PCM (Washington *et al.* 2000; Meehl *et al.* 2003) and GFDL CM2.1 models' output for both B1 and A2 IPCC scenarios for a range of projected temperature increases ranging from 1.7 °C (PCM B1) to 3.9 °C (GFDL A2) following Cayan *et al.*, 2008. While exact numbers vary, the qualitative nature of the impacts was the same across scenarios. For clarity, we chose the A2 GFDL scenario to illustrate the findings for this study.

Downscaled climate data for the A2 GFDL scenario for the 2001-2100 period (daily minimum and maximum temperature and daily precipitation) were retrieved from <http://tenaya.ucsd.edu/wawona-m/downscaled>, where a data collection representing future climate scenarios was made available as part of USGS CASCaDE (Computational Assessments Scenarios of Change for the Delta Ecosystems) project. The downscaling procedure of transforming the coarse resolution information from the A2 GFDL model (2.5° x 2.5°) to a finer resolution (1/8° x 1/8°) followed the method of constructed analogues described in Hidalgo *et al.*, (2008).

For the Tuolumne area, the 1/8° cell closest to the Dana Meadows station was selected for the climate data. Because this cell had a mean elevation different than the Dana Meadows elevation, we bias-corrected the projected climate dataset for differences in temperature and precipitation. Monthly biases in air temperature and precipitation were estimated based on the climate model output averaged over the 1971-2000 historic period and PRISM averages for the same period. Air temperature was corrected using these monthly biases, and precipitation was scaled by a factor of 1.2 (the mean 1971-2000 bias) for the entire 2001-2100 period. The total annual precipitation and annual average temperature for the climate change scenario are shown in Figure 5.2. While there was no quantified trend in precipitation, the last two decades were drier than the average. There is a significant increase in air temperature of about 3.5-3.9 °C by the end of the century (Figure 5.2).

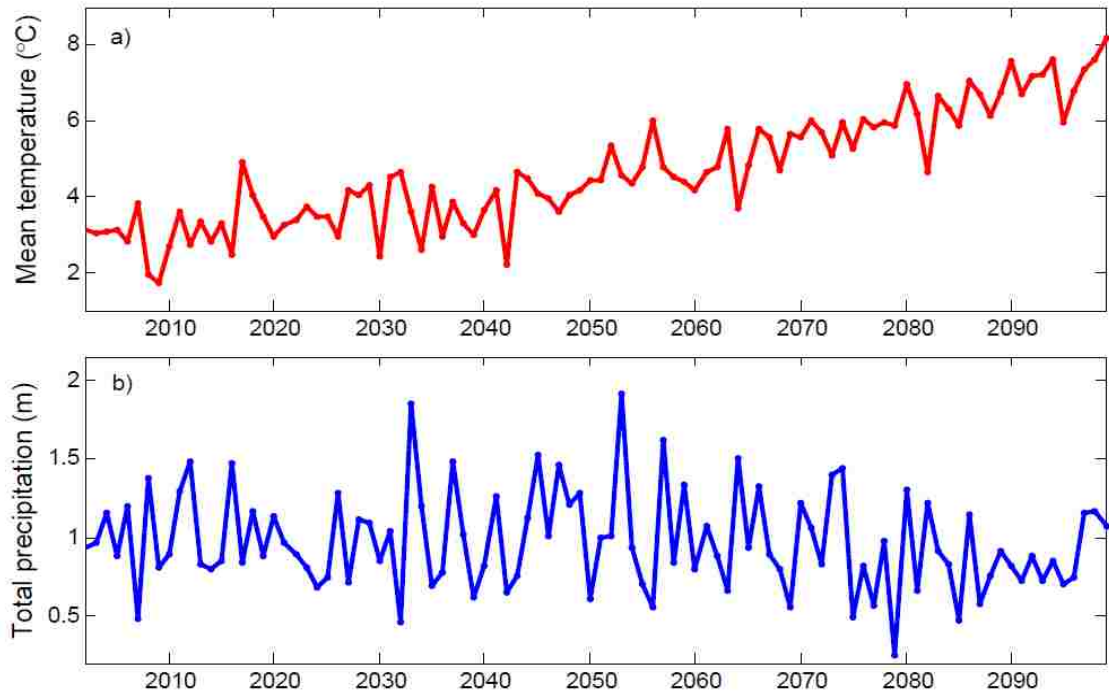


Figure 5.2 a) Mean annual temperatures and b) total precipitation for the climate simulation period 2001-2100.

Once the climate input data were established, we set up DHSVM to simulate streamflows for the 2001-2100 period assuming four different vegetation scenarios: 1) current forest, spatially distributed on the extent shown in Figure 5.1, as the base case, 2) entire basin covered by forest, 3) entire basin is barren, and 4) current forest extent, but fractional coverage is reduced, presumably as a result of thinning or controlled fire. The four vegetation scenarios are summarized in Table 5.2. These scenarios were considered to explore the basin sensitivity to climate warming as a function of forest cover extent and density to address the question of whether a more forested basin is more or less sensitive than a less forested basin to changes in climate. For all of these runs, we used the DHSVM setup for the calibration period, in which we only changed the extent and fractional cover, keeping the remaining forest parameters constant, with climate forcing for the years 2001-2100.

Table 5.2 DHSVM vegetation scenarios for the A2 GFDL climate data.

Model scenario	Scenario assumptions
current forest	distributed forest (on 39% of the basin surface, extent shown in Figure 5.1), 80% fractional coverage over each forested pixel
all forest	uniform forest cover, 80% fractional coverage over each pixel
barren	barren
thinned	distributed forest (on 39% of the basin surface, extent shown in Figure 5.1), 40% fractional coverage over each forested pixel

5.3.3. Methods to analyze changes in streamflow patterns

Changes in streamflow patterns were evaluated using the center of mass, COM (as in Stewart *et al.* 2005), the date on which fractional cumulative discharge reaches 50%, and monthly fractional flows (MFF), the ratio of flow volume in each month to the total flow volume of the water year. To test for existence of trends in the COM and MFF timeseries we applied the Mann-Kendall test (Mann, 1945, Kendall, 1975, Helsel and Hirsch, 2002), a robust non-parametric test for trend, in which the null hypothesis assumed that COM and MFF are independent random variables (no trend). Prior to assigning the trend, we tested if the presence of autocorrelation in the timeseries was affecting the significance of the trend with algorithms provided in Yue *et al.*, 2002. Because the Mann-Kendall test detects only the existence and direction of a trend, it was used in conjunction with Theil-Sen or Sen's slope estimator (Theil 1950a-c, Sen, 1968), which quantified the magnitude of the linear trend (applied in Lettenmaier *et al.*, 1994; Yue and Hashino, 2003). All trends are reported for 5% significance level.

To test whether the COM timeseries for the four vegetation scenarios are stochastically different (do not follow the same distribution), we used the non-parametric Mann Whitney U test (Mann and Whitney 1947), also known as the Wilcoxon rank-sum test, for equality of the medians. The test has no underlying distribution of the data, and the null hypothesis assumes that any two COM series are drawn from the same distribution. The purpose of this test is to assess the uncertainty in the projected COM series for the four vegetation scenarios and to assign statistical confidence if the difference between scenarios is significant.

The changes in summer flows are important for meadow ecology and for estimating the water volumes that are to be distributed downstream for water supply. We used the Mann-Kendall trend tests to determine if trends exist in the lowest 7-day average low flows during the July-August period. Because the climate data are non-stationary, the typical probability distribution fitting technique to examine changes in frequency (e.g. Schnorbus and Alila, 2004, Kuràs *et al.*, 2012) is not suitable, as the probability of occurrence of extreme events may change in time (Wigley, 2009). Instead, we used the simple discharge threshold technique (e.g. Tague *et al.*, 2008) to illustrate the differences in frequency of occurrence of low flows between the model scenarios, in which for each scenario, a relative frequency is calculated as the number of years in which the lowest 7-day average low flow is less than a threshold value, divided by the total number of years.

5.4. Results

5.4.1. Model evaluation for the historic period, 2003-2009

DHSVM performance for the 2003-2009 period was evaluated through comparing the modeled and observed hydrographs (Figure 5.3a, b) and SWE at the two snow pillow locations in the basin, Dana Meadows and Tuolumne Meadows for the available record (Figure 5.3c,d). The Nash-Sutcliffe efficiency, *NSE* (Nash and Sutcliffe, 1970) and sum of the error squared (R^2) model evaluation criteria for the hydrograph (daily timestep) were both equal to 0.87, indicating a “very good” performance of the model to capture patterns of the observed hydrograph (where the “very good” category, as classified by Moriasi *et al.*, 2007, was assigned a range of *NSE* between 0.75 and 1). Other classifications of *NSE* are more restrictive, such as that of James and Burges (1982) who suggest a *NSE* in excess of 0.95 as a very good performance. Errors are due to both model uncertainty and rating curve extrapolation at high flows. The model was able to represent the snow accumulation and melt for a range of climate conditions at the two snow pillow sites, Dana Meadows and Tuolumne Meadows as shown in Figure 5.3c,d. The missing SWE observations in Figure 5.3c,d were due to instrument failure.

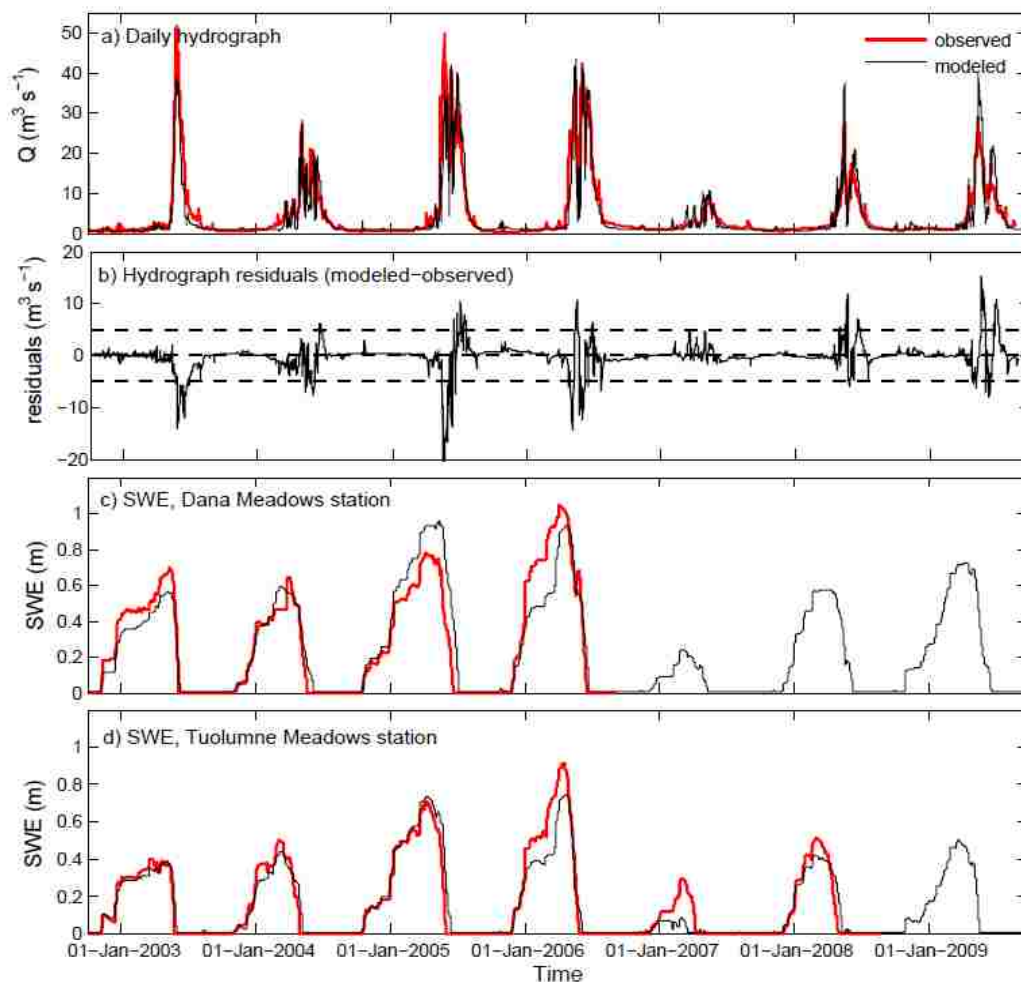


Figure 5.3 DHSVM calibration: a) simulated and observed daily hydrographs, b) hydrograph residuals, c) and d) simulated and observed SWE at Dana Meadows and Tuolumne Meadows sites, respectively.

Special consideration was given to representing the hydrograph recession limbs and the late summer low flows, as the simulated DHSVM fluxes in the meadow area were used as boundary conditions for a groundwater model in a study designed to evaluate the effects of dry soil conditions on the Tuolumne Meadow plant communities (Lowry *et al.*, 2010). Because summer precipitation is low (only 3% of the annual total during July-August period for 2003-2009), most of the summer flow results from high-elevation melt. Figure 5.3c,d shows that snow is disappearing at Dana Meadows (2966 m) around mid-June and at Tuolumne Meadows (2600 m) at the end of May, with an average difference of about two weeks. This difference is consistent with observations by Rice *et al.*, (2011) that for elevations between 1800 and 3900m, for each successively higher 300m elevation band, snow has disappeared 2-3 weeks later than the 300-m band

below it. At higher elevations snow persists until the end of August or September, or remains present during the entire year (Lundquist and Loheide, 2011; Rice *et al.*, 2011).

5.4.2. Simulated changes in streamflow timing and magnitude as a function of vegetation cover in a warming climate

5.4.2.1. Temperature sensitivity tests

To explore the differences in hydrograph characteristics and SWE, as well as the changes in the energy balance components at forested and barren sites when temperature increases, we analyzed the model output using the sensitivity tests described in Section 3.2. These tests were run for the calibration period 2003-2009, from which we extracted the October 1st 2003 – October 1st 2004 period (water year 2004) to illustrate the results. The 2003-2009 period included a range of conditions (Figure 5.3). While water year 2004 was an average year, it was found representative for the types of changes seen in both wet and dry years. In the first set of tests (scenarios 1-4, Table 5.1), in both temperature cases, historic T and historic T + 3 °C, the forest COM occurred earlier than the barren COM, with decreased peak hydrographs (Figure 5.4a,c). In the case of the higher temperature this difference was larger, increasing from 9 to 14 days. Winter temperatures exceeded 0 °C more frequently in the increased temperature scenario (Figure 5.4f, region C), generating snowmelt runoff (Figure 5.4a, region A). These midwinter peaks are more pronounced in the case of the forest (Figure 5.4a, region A) than in the case of barren (Figure 5.4c region B), due to increases in net longwave radiation, as further discussed in this Section. Midwinter melt was not apparent in any of the historic T tests (Figure 5.4a,c).

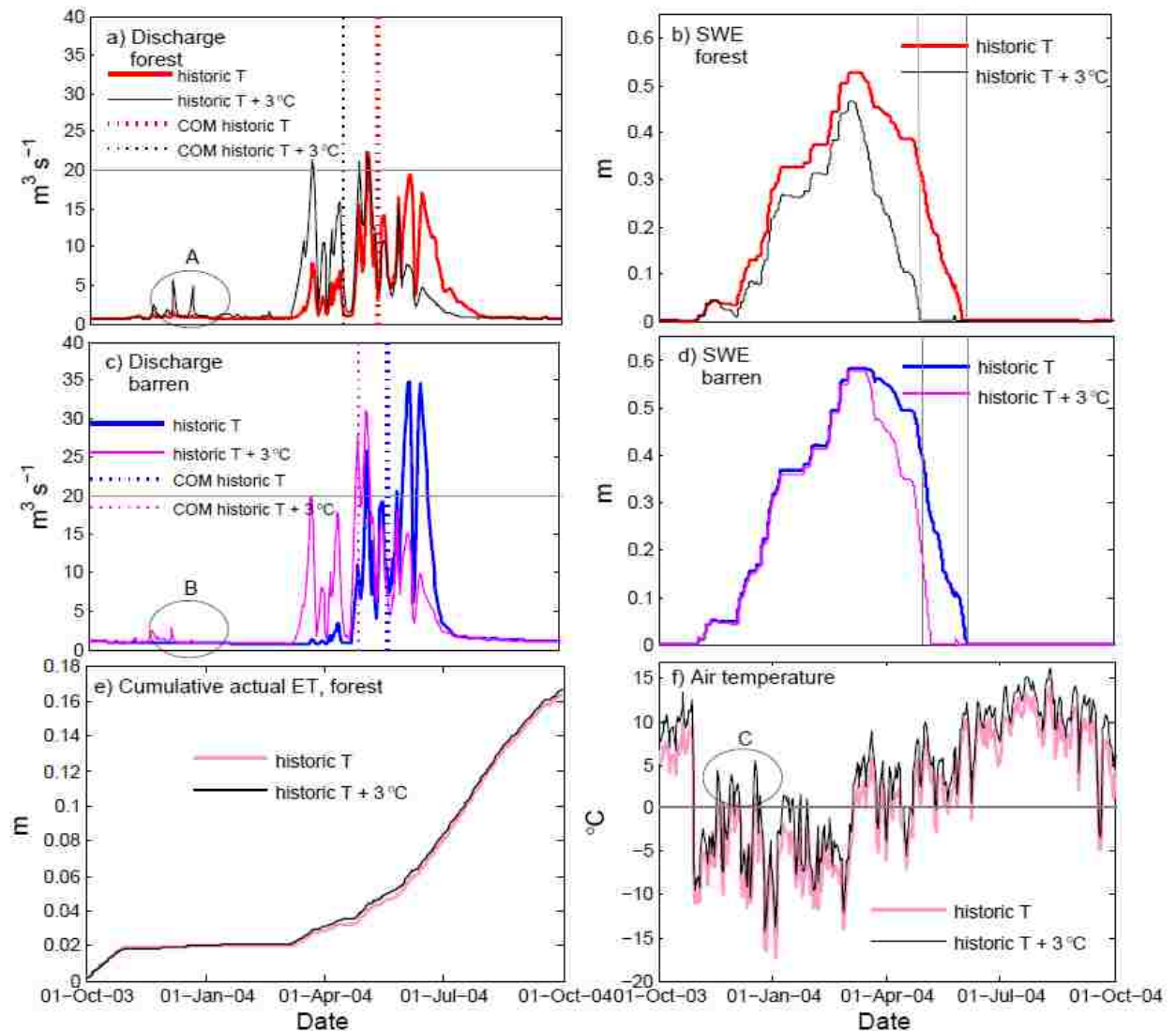


Figure 5.4 a) Simulated hydrographs assuming historic and increased air temperatures for uniform forest scenario and for b) barren scenario; c) and d) SWE levels for the same scenarios at Dana Meadows, respectively; e) forest cumulative actual evapotranspiration; f) historic and increased air temperature daily timeseries. Vertical lines identify COM for each hydrograph. All plots are shown for water year 2004. Horizontal (a, c) and vertical (b, d) continuous lines are reference thresholds.

The differences in streamflow timing depend on the snow accumulation and melt dynamics in the barren areas and under the forest. The simulated SWE at the flat Dana Meadows location (Figure 5.4b, d) show that accumulation is higher when trees are not present due to the lack of canopy interception. While snow accumulation on bare ground is similar in both temperature scenarios, during the melt period the higher air temperature melts the snow earlier (Figure 5.4d), leading to earlier streamflow timing (Figure 5.4c). Higher air temperatures produced more winter melt than in the forest case (A in Figure 5.4a) than in the barren case (B in Figure 5.4c). The snow accumulation

under the forest was therefore lower under warmer temperatures (Figure 5.4b) due to winter melt events (Figure 5.4a and 5.4b). This thinner forest snowpack melted earlier than the barren snowpack in the increased temperature scenario (vertical line in Figure 5.4b and 5.4d). Forest evapotranspiration increased only 3% with temperature (Figure 5.4e); therefore the changes in the forest hydrographs were mostly driven by the changes in snowmelt due to temperature increases.

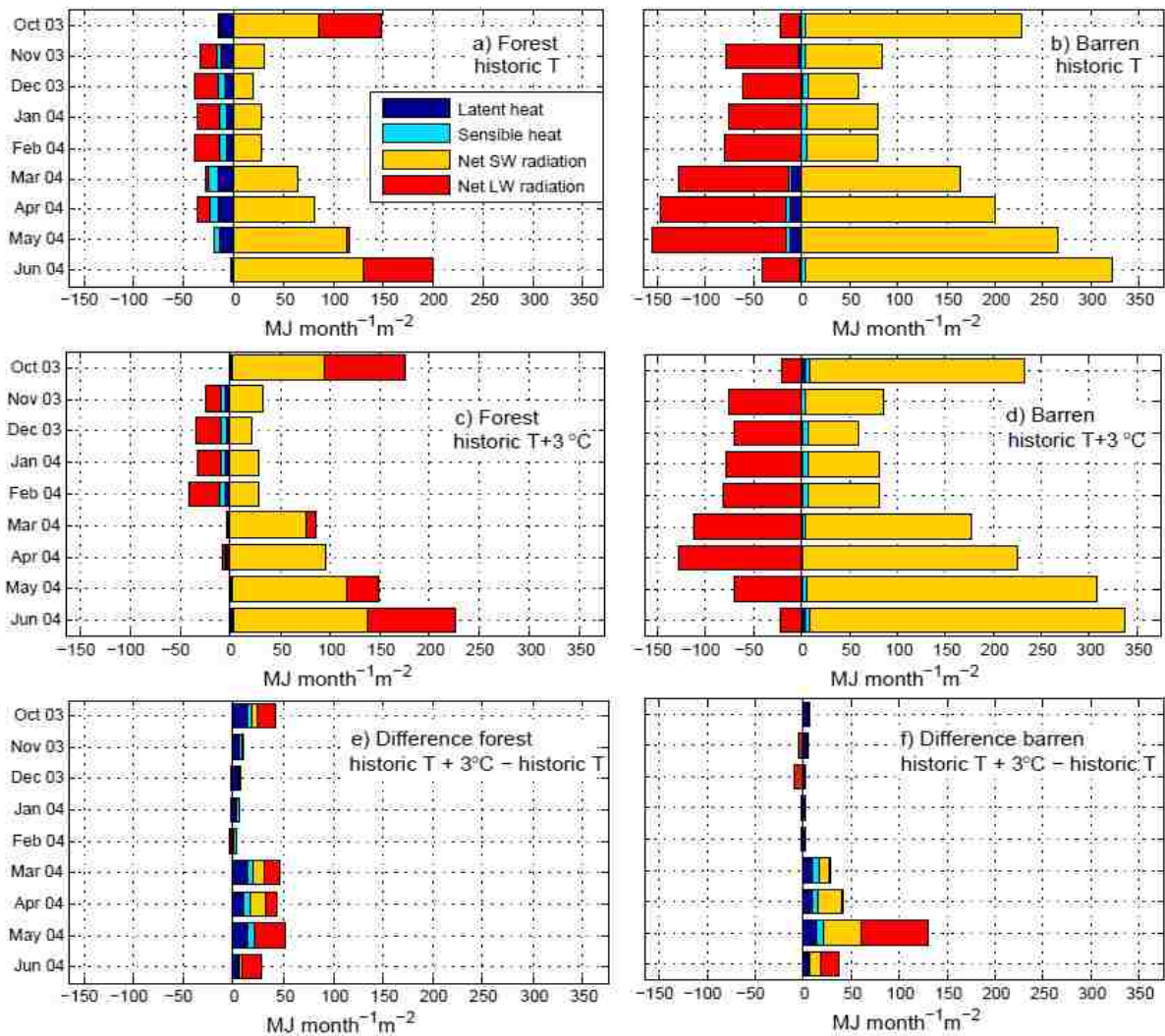


Figure 5.5 Monthly simulated energy balance components for the snowpack at Dana Meadows using historic temperatures for a) forested, and for b) barren; monthly energy balance components using a 3°C increase in temperature for c) forest, and for d) barren; monthly differences in energy balance components between the two temperature scenarios for e) forest, and for f) barren.

Increases in temperature increase the energy balance components both in the barren areas and under the forest. Figure 5.5a-d shows the monthly energy balance components of the snowpack (estimated by summing the three-hourly timeseries generated by the model described in Appendix 5A) for water year 2004 at Dana

Meadows for the two vegetation scenarios. The absolute magnitudes of net SW and net LW radiation were consistently larger for the barren scenario (Figure 5.5 b,d) than the forest scenario (Figure 5.5 a,c), but the net increases in the combined fluxes were larger for the forest case (Figure 5.5e) than the barren case (Figure 5.5f) for all months except May, June, and July. Time-series of turbulent fluxes, latent and sensible heat, were higher in the barren than in the forest case, but variations around zero caused monthly values to be small for all scenarios. For the forest case, the net longwave radiation increases most, followed by increases in latent heat flux and sensible heat flux, and in March and April, increases in net shortwave radiation (Figure 5.5e). The model simulated changes in shortwave radiation (Figure 5.5e, f) because the albedo algorithm is based on the simulated snow surface temperature (Eq. A6, A7, Appendix 5A), which was higher in the increased temperature scenario.

These changes are most evident in the spring and summer, although the smaller winter increases were enough to cause December and January melting in the +3°C forest scenario when no melt occurred in those months during the base case run (Figure 5.4 and Figure 5.6). Increases in energy balance components were larger in the forest case than the barren case in March, due primarily to greater increases in net longwave radiation (Figure 5.5e,f). Although the monthly melt rates were still higher in the barren case during March and April for both the base-case and warmer scenarios (Figure 5.6), the combination of interception (a thinner initial snowpack, Figure 5.4b), midwinter melt (Figure 5.4a), and greater increases in melt rates in Dec, Jan, and March (Figure 5.6b and 5.6c) led to the snowpack under the forest melting earlier than the snowpack on the bare ground in the +3°C scenario.

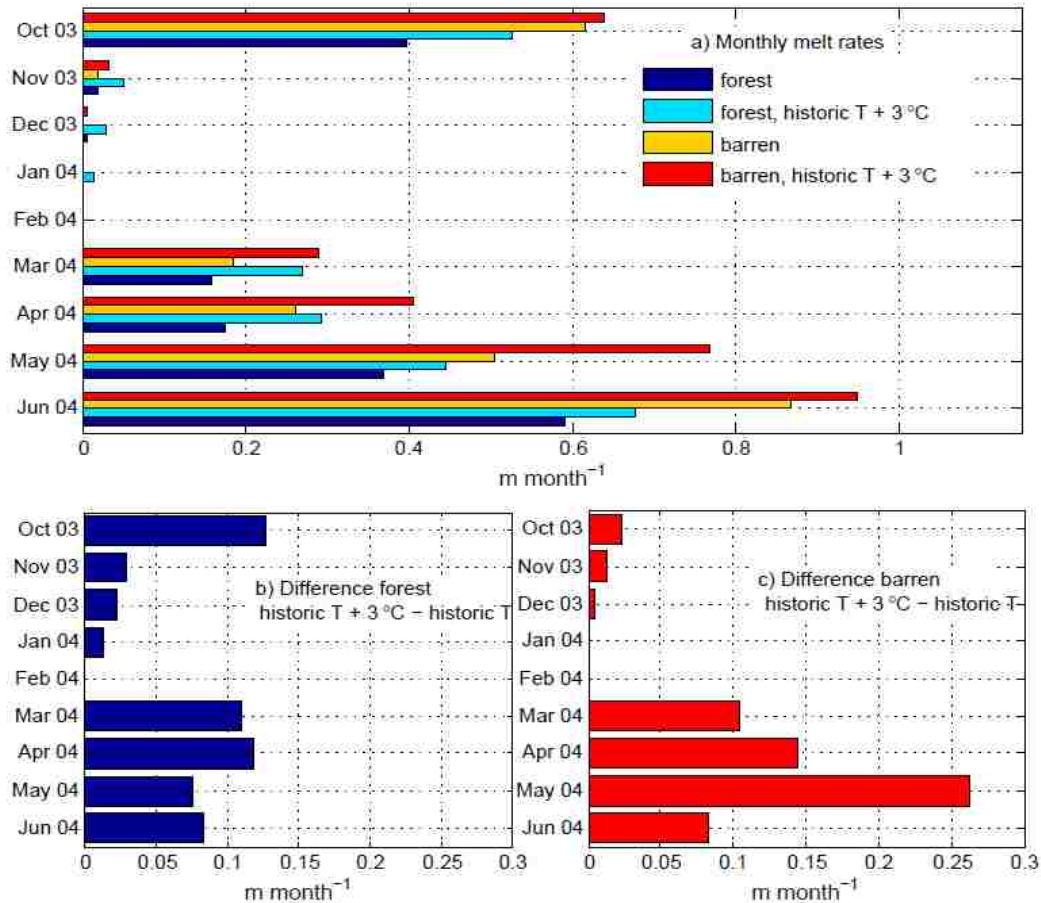


Figure 5.6 a) Monthly melt rates at Dana Meadows using historic and increased temperature for forest and for barren scenarios, b) difference in monthly melt rates using historic and increased temperature for forest, c) difference in monthly melt rates using historic and increased temperature for barren surface.

5.4.2.2. Climate change scenario

The ΔT sensitivity tests helped identify the changes in the hydrograph and energy balance components when temperature alone is increasing. By using a long-term (2001-2100) climate change scenario in which both temperature and precipitation change in concert we tested if the patterns were robust in a projected future scenario for the Tuolumne region. All DHSVM climate vegetation runs assumed the same future scenario derived from the GFDL global climate model A2 warming scenario, as previously described. The COM corresponding to the current vegetation scenario advanced by approximately 40 days, with an estimated Sen's slope of about $0.4\ days\cdot yr^{-1}$ (Figure 5.7a, b). The trends of earlier, simulated center of mass, COM, were found to be statistically significant for all vegetation scenarios, using the Mann-Kendall tests at the 95% confidence level. COM advances exceeded one month in all vegetation scenarios (Figure 5.7a). Figure 5.7b shows Sen's slopes magnitudes representing the rates of COM

displacement, which correspond from highest to lowest to all forest, current forest, thinned and barren, respectively.

Wilcoxon rank-sum tests on the COM vegetation timeseries indicated pairwise differences in the medians between the current forest, all forest and barren scenarios, respectively, showing that these COM series are stochastically different at a 95% confidence level (Figure 5.7c,d). However, no significant difference was found between the current forest and the thinned forest, and between the barren and the thinned forest scenarios, respectively (Figure 5.7c,d).

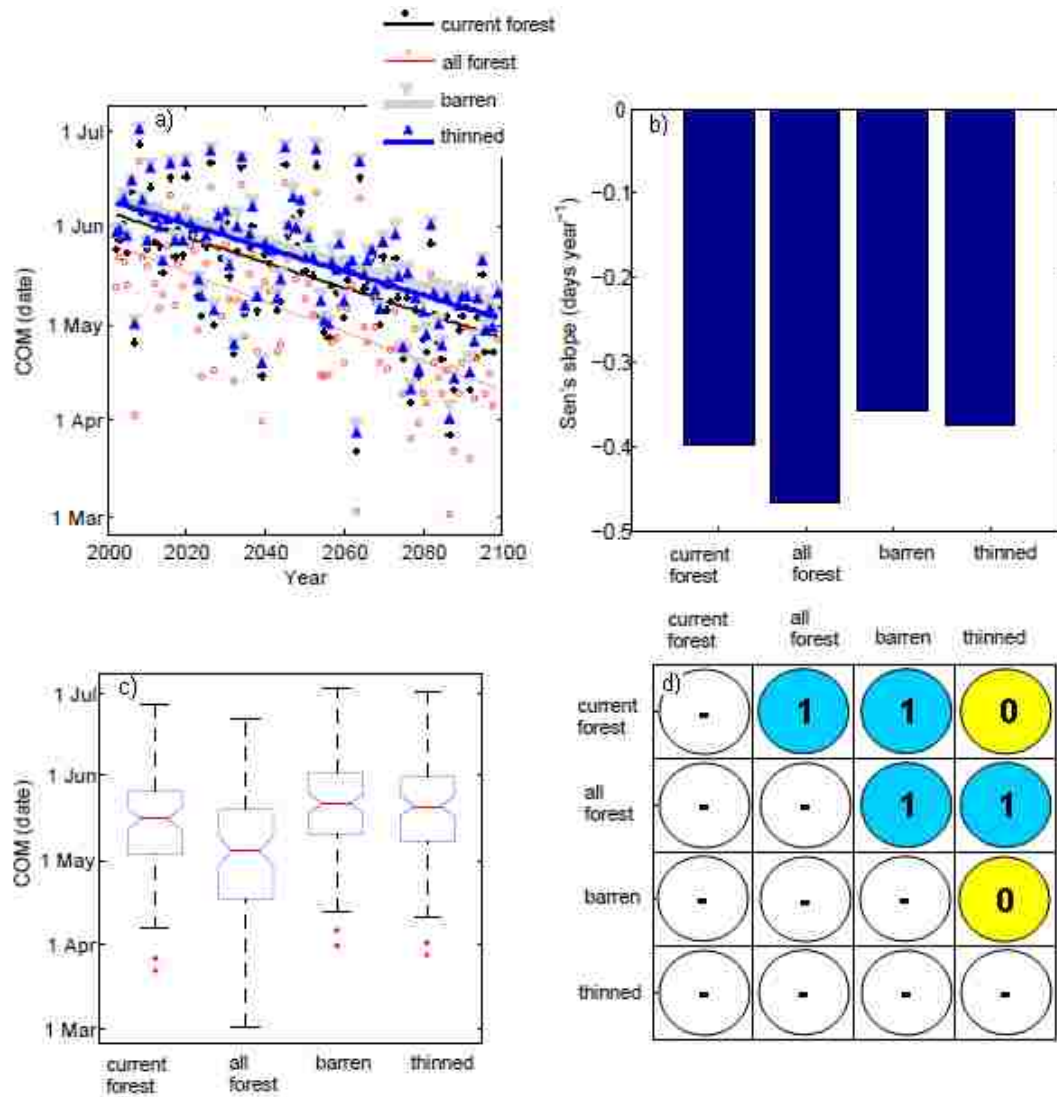


Figure 5.7 a) Center of mass, COM, for the four vegetation scenarios, b) Sen's slope of COM change, c) boxplots of the COM series, and d) diagram showing results from the Wilcoxon rank-sum test for the medians between combinations of any two COM series of the four vegetation scenarios: 0 indicates that the null hypothesis that the two COM

series are drawn from the same distribution cannot be rejected at the 95% confidence level, and 1 indicates a rejection of the null hypothesis.

Vegetation cover affects not only timing, but also the streamflow magnitude. This is illustrated in Figure 5.8a-d that shows the 20-year average monthly hydrographs during the 2001-2100 simulation period for the four vegetation scenarios. In the all forest scenario (Figure 5.8b), the hydrograph peak was smaller than in both the current vegetation (Figure 5.8a) and all barren (Figure 5.8c) scenarios, as there were increased losses to interception, sublimation and evapotranspiration. This effect is consistent with observations from both paired watershed and from modeling studies (e.g. Jones and Post, 2004; Schnorbus and Alila, 2004). Modeled differences in peak flows in DHSVM are mostly explained by the interception effects (e. g. Whitaker *et al.*, 2002).

The largest monthly flows of the year (May-July) were on average about 20% smaller in the all forest scenario (Figure 5.8b) compared with the base case current vegetation (Figure 5.8a) scenario, while barren (Figure 5.8c) and thinned (Figure 5.8d) forest flows were both on average higher (19% and 13%, respectively) than the base case vegetation scenario (Figure 5.8a), over all time periods simulated. However, early spring (March-April) flows were consistently the largest in the all forest (Figure 5.8b) scenario, resulting in earlier COM timing. Late-winter and early spring flows (January-March) were higher by 30%-40% in the all forest (Figure 5.8b) scenario and lower by about 24% over the same time period in the all barren (Figure 5.8c) scenario compared with the current vegetation (Figure 5.8a) scenario. Peak summer flows decreased with increasing temperature over the 100-year simulation period by about 22%, 27%, 16% and 18% for the current forest, all forest, barren and thinned forest scenarios, respectively. These larger differences are due to the lower precipitation during the last 20 years of the series (Figure 5.2b).

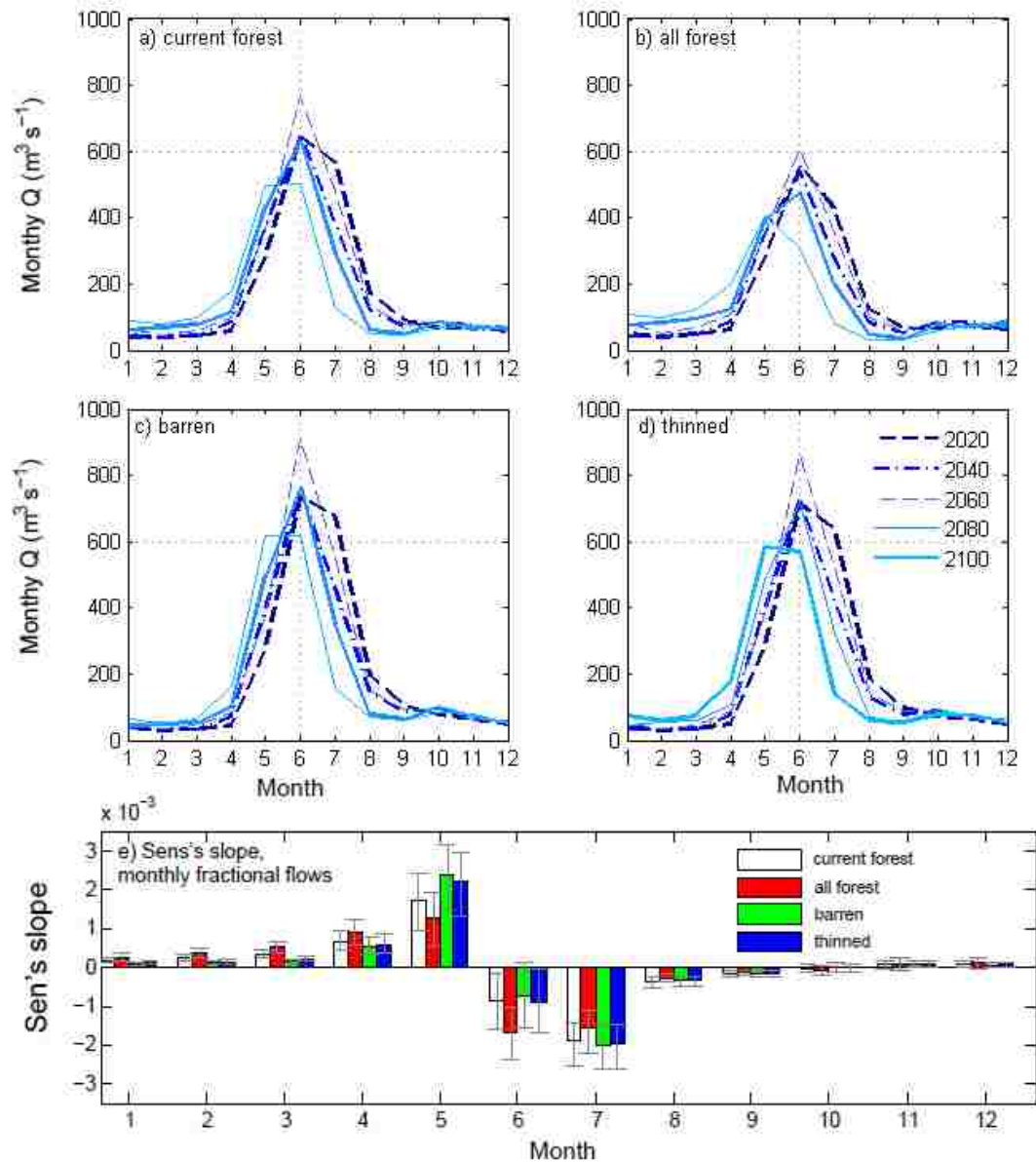


Figure 5.8. a) Twenty-year average monthly hydrographs at the beginning (dotted line) and end (continuous line) of the simulation period for current forest, b) all forest, c) barren and d) thinned forest scenarios, respectively; e) Sen's slope for monthly fractional flows for the entire 2001-2100 simulation period.

Changes in the hydrograph were determined by the trends in monthly fractional flows, MFF, shown in Figure 5.8e along with the 95% confidence intervals for the slope. Trends are significant if the 95% confidence intervals do not intersect the zero line. The steepest trends for all vegetation scenarios were in May (increases in MFF) and July (decreases in MFF), while during the fall months (October, November and December) there were no significant trends. The winter to spring MFF trends (January through April) are significantly steeper in the all forest scenario than in the all barren scenario (Figure 5.8e). This effect is also illustrated by the ΔT sensitivity runs (Figure 5.4a, b),

where COM advanced at a higher rate in the all forest scenario determining the steeper trends in winter monthly fractional flows shown in Figure 5.8e. Thus, when the forest is present, there is an increased tendency for midwinter melt than under barren conditions. This difference is driven by the trends in the energy balance components. For example, trend tests at the flat Dana Meadows location for forest and barren, the two extreme cases, showed that the temperature dependent components such as the monthly latent heat, sensible heat and net radiation (for functional forms see Appendix 5A) have positive trends for under the forest, compared to no trends or negative trends in the barren case during the January-April period.

The earlier snowmelt led to lower summer flows in all vegetation scenarios, with the most significant change occurring in July (Figure 5.8a-d). Thus, the Mann-Kendall tests showed significant declining trends in the 7-day average lowest flows for the July-August period. Barren conditions were likely to provide the highest summer flows, followed by thinned, current forest and all forest conditions (Figure 5.9a, b). The all forest scenario had the highest frequency of 7-day low flows below $2.0 \text{ m}^3\text{s}^{-1}$, followed by current forest, thinned and barren (Figure 5.9c). The fixed threshold value used to calculate the relative frequencies was $2.0 \text{ m}^3\text{s}^{-1}$, the average summer (July-August) lowest flows in the current forest scenario for the entire climate model period (Figure 5.9a, b). Compared to this value, the same average lowest flows for barren and thinned are 23% and 9% higher, while for all forest is 27% lower.

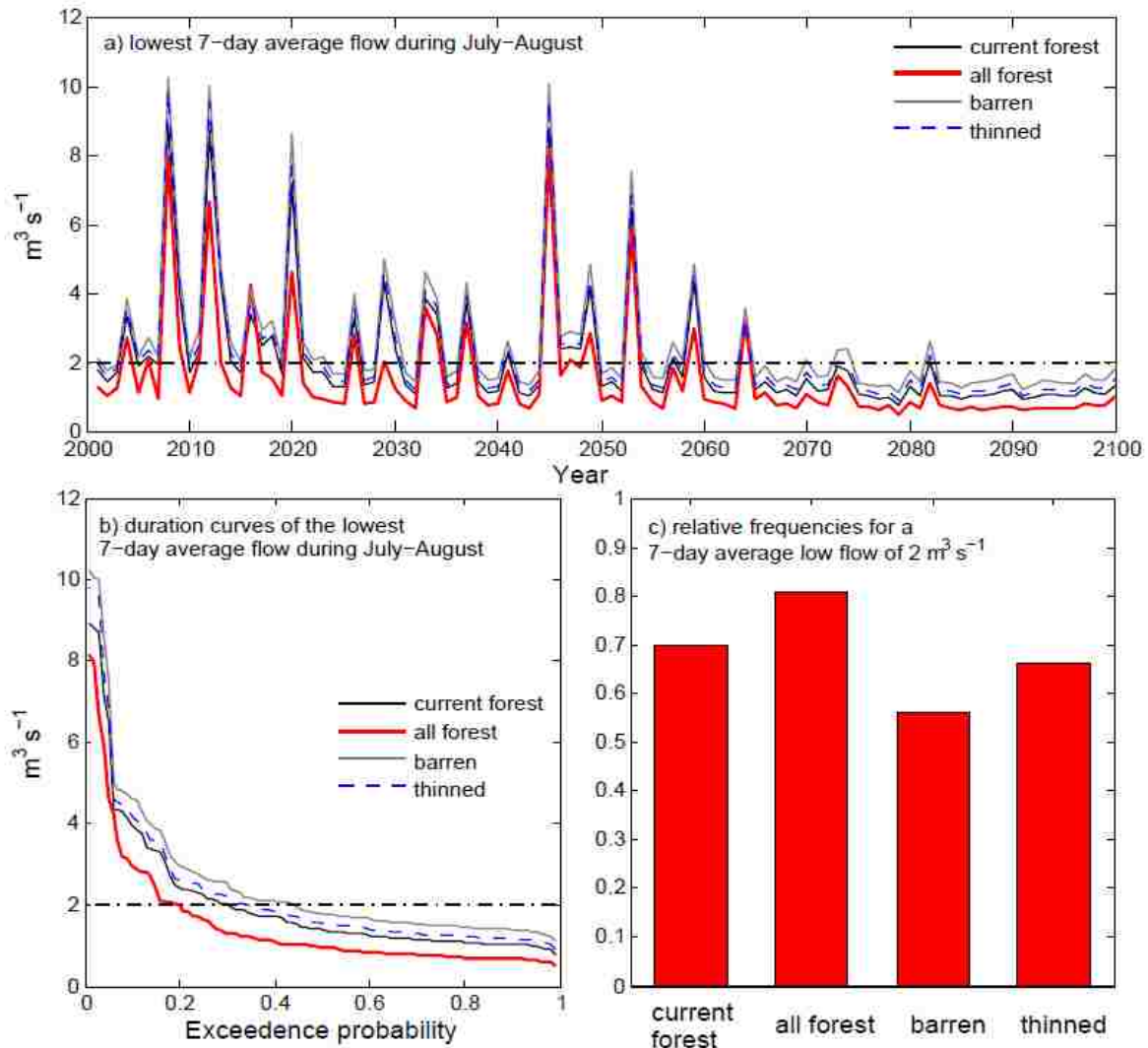


Figure 5.9 a) Lowest 7-day average low flow during July-August each year for the four vegetation scenarios, b) duration curves for the July-August 7-day average lowest flows, and c) relative frequencies, as the number of years in each the lowest 7-day average was below a threshold value ($2 m^3 s^{-1}$) divided by the total number of years.

5.5. Discussion

Hydrologic simulations in the upper Tuolumne basin in the Sierra Nevada Mountains showed that forest cover plays an important role in the rate of streamflow advances to earlier dates in response to climate warming. The idealized modeling experiments designed to address the sensitivity of the basin response to land cover (Table 5.2) have shown that a less vegetated basin maintains a thicker and colder snowpack that melts later in the season. This thicker snowpack was able to delay the rate of COM (center of mass) advancing, and to provide higher peak and late summer flows. Assuming the current vegetation cover, the COM was projected to occur earlier by about 40 days by the end of the century under the A2 warming scenario from the GFDL CM2.1 global

climate model. The most important changes in streamflow patterns determining the COM displacements were shifts to earlier snowmelt due to increased temperature, with higher winter flows and reduced peak and late summer flows. Similar hydrologic changes in response to climate warming were found at a lower elevation in the Tuolumne basin based on hydrologic simulations encompassing a much larger drainage area (3970 km²), stretching over 1600 m elevation range (Maurer, 2007).

The basin sensitivity to increasing temperature was tested under different vegetation scenarios. Under barren conditions the modeled accumulation was higher by about 10-30 %, than under the forest, mostly due to the lack of canopy interception. This range is consistent with field measurements in lodgepole pine (*Pinus contorta*) stands that have shown that snow accumulation in the barren areas can be 10-40% higher than under the forest and as high as 80-85% in some locations (summary from Table 2 in Murray and Buttle, 2003). With increasing temperature, the modeled difference in accumulation tended to widen with temperature as a result of increasing midwinter melt, and it was more pronounced at lower elevations (Figure 5.A1b,d,f,h).

Modeled melt rates were higher in the barren areas than under the forest during the spring-summer melting period (Figure 5.6), but the thinner snowpack under the trees melted earlier, especially at lower elevations (Figure 5.4b,d; Figure 5.A1b,d,f,h). Snow disappearing earlier under the forest or in the barren areas may depend on the snowpack thickness (Strasser *et al.*, 2011). At the flat Dana Meadows and Tuolumne Meadows locations modeled snow disappeared earlier under forested conditions during average years (e.g. 2004, Figure 5.4b,d; Figure 5.A1b,d,f,h), and also during dry and wet years of the 2003-2009 period (Figures not shown). This under the forest melting pattern was robust despite uncertain forest parameterization, as shown in Appendix 5A, Figure 5.A1b,d,f,h. Midwinter melt was higher when the snowpack under the forest was thinner. Figure 5.6b,c show that in contrast to the warm period (May-July), during the cold period (October-January) under the influence of higher winter temperatures, melt rates have a more significant increase under the forest. Midwinter melt was most evident during December and January, when for historic temperatures there was little to no melt in both forested and barren cases, but when temperatures were increased above 0°C values for several days, melt occurred under the forest (Figure 5.6a).

Slope, aspect and elevation all play an important role in the snow accumulation and melt patterns. For example, on the south facing slopes the snow melted faster in the barren areas than under the forest, while on the north facing slopes the snow melted faster under the forest in an eastern Canadian Rocky Mountain basin (Ellis *et al.*, 2011). The upper Tuolumne basin has both north and south facing slopes, but the north facing slopes are predominant. Most of the currently non-forested regions are north-facing, topographically shaded (Figure 5.1). Thus, the overall effect of the increase in the net longwave radiation was to melt the snow under the forest faster. The increased midwinter melt under warming temperatures enhances this faster melting under the

forest. In the barren areas, the thicker snowpack lasted longer, providing higher and later peak spring flows and higher late summer flows.

Field studies also reported that melt rates during the spring were generally higher in the barren regions or in clearcut areas than under the forest (Murray and Buttle, 2003, Boon, 2009, Burles and Boon 2011, Winkler, 2011), but the date of snow disappearance was found to vary as a function of location, aspect, snowpack thickness and canopy density. For example, snow cover loss occurred earlier by several days in a damaged forest or a clear cut than in a mature forest in the interior of British Columbia, Canada (Boon, 2009; Burles and Boon 2011; Winkler, 2011), while in central Ontario, for the same slope aspect, the snow disappeared simultaneously in the barren areas and under the forest (Murray and Buttle, 2003). These sites were located in a colder climate than the Tuolumne site, with lower chances of midwinter melt events.

Although there is significant spatial variability, as discussed above, reported field measurements in the Sierra Nevada Mountains indicate that snow in this region generally disappeared earlier or at about the same time under the forest than in the barren areas (Kittredge 1953, Lundquist and Lott, 2008; Bales *et al.*, 2011a, Kerkez *et al.*, 2012). Early historical observations from the 1930s and 1940s in the Central Sierra showed that snow disappeared earlier in regions with lower percentages of canopy cover (figure shown on page 54, Kittredge 1953). Spring (after March 9) melt rates were higher in the open than under the forest, but winter (before March 9) melt rates were higher under the forest for several years and most forest types (Table 28, Kittredge 1953). DHSVM SWE simulations in the Tuolumne area showed that at the two snow pillow locations the snow cover loss occurred earlier under the forest than in the barren areas (Figure 5.4b,d, Figure 5.A1b,d,f,h). This effect is more pronounced with increasing temperatures and midwinter melt events. Recent areal imagery taken in mid-June of 2011 near the Tuolumne area (Lat: 38°48'56", Long: 120°06'35") exemplifies these findings (Figure 5.A2). This image shows the snow disappearing first around the trunks of the trees, where melt rates have been found to be higher (Pomeroy *et al.*, 2009; Veatch *et al.*, 2009). Additional observational evidence of where and analysis of why snow lasts longer under forest cover versus in the barren areas remains a topic for future investigation.

The dynamics of snowmelt change with increasing temperature in both barren and forested scenarios. Field and modeling studies have found that incoming shortwave radiation and turbulent fluxes were higher in the barren regions than under the forest (Hardy *et al.*, 1997; Link and Marks, 1999a 1999b; Sicart *et al.*, 2004; Boon, 2009). Ablation in the barren areas is controlled by the shortwave radiation, whereas net longwave radiation has a smaller contribution to melting (Boon, 2009). In contrast, under the forest, longwave radiation has a higher contribution to melting (Boon, 2009; Burles and Boon, 2011). In the Tuolumne area, model temperature sensitivity tests showed that increases in temperature determined increases in both the net longwave radiation and turbulent fluxes under the forest that are higher than the increases in the

barren areas. These changes triggered higher melt rates under the forest, causing even earlier snow disappearance dates and exacerbating the effects of climate change in terms of streamflow timing advancing towards earlier dates. Temperature increases had a modest effect (3%) on simulated forest evapotranspiration. This effect is similar to findings of Safeeq and Fares (2011) who reported small increases of modeled DHSVM evapotranspiration with temperature alone (0.5 and 2% for a temperature increase of 1.1 and 6.4 °C).

Uncertainties in the upper Tuolumne simulations fall into three general categories, related to: i) the trend of future carbon emissions, ii) the climate model output and downscaling procedures, and iii) the hydrologic model. Current observations suggest that the A2 emissions scenario may be a conservative estimate of temperature change given current global trends in CO₂, and that the large-scale temperature increases may be even larger than those considered in this study. There is recognized uncertainty about the GCMs' ability to predict changes in large scale weather patterns, particularly as they relate to precipitation (e.g., Dai 2006, Maraun *et al.* 2010). This uncertainty from the GCMs may be larger than the uncertainty from the hydrologic models (Teng *et al.*, 2012), which primarily stems from the hydrologic model structure and model parameterization. In the Tuolumne area, the model tests showed that even when considering a relatively large uncertainty in forest parameterization the model simulated snow disappearing faster under the forest than in the barren regions, with this effect enhanced at higher temperatures.

Management decisions in snowmelt-dominated areas like Tuolumne Meadows, which are dependent on streamflow timing and magnitude for ecological purposes, can expect differing sensitivities to vegetation cover in a warming climate. The upper Tuolumne area is in Yosemite National Park, where timber is not harvested. However, results from the virtual experiments evaluated in this study can be extrapolated to other regional basins where forest management actions are considered for summer flow augmentation. For example, Bales *et al.*, (2011b) investigated forest management actions that can increase summer water yield on the west-side of the Sierra Nevada at 1500-3600m elevation, and suggested that canopy reduction through forest thinning has the potential to improve snow retention and increase streamflows. Preliminary results indicated that a reduction in forest cover by about 40% could increase the water yield by about 9% (Bales *et al.*, 2011b). These estimations are in agreement with the results from this study and the earlier findings of Kittredge (1953). Model simulations performed in the upper Tuolumne for the thinned forest scenario, in which the canopy cover is reduced to 50% of the current levels showed similar ranges: increases in the peak and late summer flows by about 13% and 9%, respectively. In addition to summer flow augmentation, forest thinning may also reduce fire risks, which are becoming higher with increasing temperatures (Graham *et al.*, 2004).

5.6. Summary and Conclusions

In the Tuolumne and Merced River basins of the California Sierra Nevada mountain range, 85-90% of annual snowmelt has been estimated to come from snowpack above 2100 m (Rice, *et al.* 2011). The amount of snowmelt water in the streams and the streamflow timing are important for the montane ecosystems and for downstream water supply. Maximizing snowpack retention above 2000m has the potential to decrease the rate of streamflow timing advancing to earlier dates and to increase summer flows. In this study we investigated, through hydrologic model simulations, the role of the vegetation cover in the rate of advancing of snowmelt timing in the upper Tuolumne River basin. We employed four different vegetation scenarios: current forest, forest on the entire basin, barren and thinned forest for the same climate warming medium-high emissions scenario from the GFDL 2.1 GCM. We also used sensitivity tests to evaluate changes in modeled energy balance components as a result of increasing temperatures and to assess the uncertainty in model forest parameterization. Analysis of the model simulations results indicated that:

- In the current forest cover scenario, warming temperatures caused earlier snowmelt timing, with increased midwinter melt and decreased peak and late summer flows. The center of mass, COM, the date on which fractional cumulative discharge reaches 50%, advanced by 40 days earlier in the season. Peak summer flows decreased with increasing temperatures by about 22%.
- The streamflow timing advanced towards earlier dates by over a month in all vegetation scenarios. The COM date at the beginning of the simulation period was dependent on the vegetation type, ranking from earliest to latest: all forest, current forest, thinned and barren (Figure 5.7a). The rate of advance varied between scenarios (Figure 5.7b) Relative to the starting date for each case, the COM advanced by 46, 37 and 39 days, respectively in the all forest, barren and thinned forest scenarios.
- The presence of forest on the entire basin area enhanced the effects of climate warming in the sense of advancing of streamflow timing. The center of mass occurred earlier in the season by about 12 days on average, and the rate of its advancing was higher by about $0.06 \text{ days}\cdot\text{year}^{-1}$ than in the case of current forest scenario over the 100-year period. Midwinter melt was increased. On average peak and late summer flows were decreased by about 20% and 27%, respectively, compared to the corresponding flows for the current forest scenario over the 100-year period. Peak summer flows decreased with temperature in time by about 27%.

- In contrast, a less vegetated basin maintains a thicker snowpack that disappears later in the season, increasing peak and late summer flows, and delaying streamflow timing. Compared with the current forest, in the barren and the thinned forest scenarios (in which canopy cover was reduced to 40%, half of the original value), COM occurred later by about 7-, and 5-days on average per 100 years, respectively. The rates of COM advancing were lower and the peak and late summer flows were higher by about 19% and 23%, respectively in the case of barren, and 13% and 9%, respectively in the case of thinned forest compared with the current vegetation scenario. Peak summer flows decreased in time on average by 16% and 18% respectively for the barren and thinned forest scenarios during the 100-year period.
- Modeled accumulation was lower under the forest than in the barren areas due to interception and midwinter melt. Melt rates were higher in the barren regions than under the forest, but the thinner snowpack under the forest disappeared earlier. Both melt rates in the barren areas and under the forest increase with increasing temperatures.
- Temperature controlled energy balance components (longwave radiation and turbulent fluxes) increased more under the forest than in the barren regions in a warming climate. These changes increase melt rates and midwinter melt.
- Longwave radiation has a higher contribution to melting in early spring when shortwave radiation is lower. In a warmer climate the forests melted the snow faster due to increases in net longwave radiation that are more significant at temperatures higher than 0°C.

Understanding forest hydrologic processes in the context of climate change is important for identifying management actions that have the potential to mitigate climate change effects such as the advancing of streamflow timing and diminished summer flows. The results presented here showed that reducing canopy cover increased snow retention, delayed streamflow timing and increased peak and late summer flows in the upper Tuolumne River basin located in the Sierra Nevada Mountains. Studies in other regions of the world are needed to provide additional insights about the role of vegetation in other climatic conditions and vegetation cover. Further work may also include sensitivity tests of precipitation to understand better the consequences of changes in both precipitation and temperature on streamflow patterns.

Acknowledgments

We thank Brian Huggett and Heidi Roop for help with field data collection, and Fred Lott for initial set-up of DHSVM. We thank Nick Burmeister for help with multiple computer

issues and transfers and Steve Burges for initial review of the manuscript. This research was supported by the National Science Foundation under Grant No. CBET-0729830 and Grant No. CBET-0729838.

5.7. References

Alila Y, Beckers J. 2001. Using numerical modelling to address hydrologic forest management issues in British Columbia, *Hydrological Processes* **15**: 3371–3387.

Alila Y, Kuraś PK, Schnorbus M, Hudson R. 2009. Forests and floods: A new paradigm sheds light on age-old controversies. *Water resources research* **45**, doi:10.1029/2008WR007207.

Andreadis KM, Storck P, Lettenmaier DP. 2009. Modeling snow accumulation and ablation processes in forested environments, *Water Resources Research* **45**, doi:10.1029/2008WR007042.

Andreassian, V., 2004. Waters and forests: from historical controversy to scientific debate. *Journal of Hydrology* **291**:1-27.

Battin J, Wiley MW, Ruckelshaus MH, Palmer RN, Korb E, Bartz KK, Imaki H. 2007. Projected impacts of climate change on salmon habitat restoration. *Proceedings of the National Academy of Sciences* **104** (16):6720-5.

Bales RC, Hopmans J, O'Geen T, Meadows M, Hartsough PC, Kirchner P, Hunsaker CT, Beaudette D. 2011a. Soil moisture response to snowmelt and rainfall a Sierra Nevada mixed-conifer forest. *Vadose Zone Journal* **10** (3): 786-799.

Bales RC, Battles JJ, Chen Y, Conklin MH, Holst E, O'Hara KL, Saksa P, Stewart W. 2011b. Forests and Water in the Sierra Nevada: Sierra Nevada Watershed Ecosystem Enhancement Project. Sierra Nevada Research Institute report number 11.1.

Beckers J, Smerdon B, Wilson M. 2009. Review of hydrologic models for forest management and climate change applications in British Columbia and Alberta. FORREX Forum for Research and Extension in Natural Resources, Kamloops, BC FORREX Series 25; 166. http://www.forrex.org/sites/default/files/forrex_series/FS25.pdf

Bewley D, Alila Y, Varhola A. 2010. Variability of snow water equivalent and snow energetics across a large catchment subject to Mountain Pine Beetle infestation and rapid salvage logging, *Journal of Hydrology* **388**: 464–479.

Bristow RL, Campbell GS. 1984. On the relationship between incoming solar radiation and daily aximum and minimum temperature. *Agricultural and Forest Meteorology* **31**: 159-166.

Boon S. 2009. Snow ablation energy balance in a dead forest stand. *Hydrological Processes* **23**: 2600–2610.

Burles K, Boon S. 2011. Snowmelt energy balance in a burned forest plot, Crowsnest Pass, Alberta, Canada. *Hydrological Processes*. **25**: 3012–3029, doi:10.1002/hyp.8067.

Carsel RF, Parrish RS. 1988. Developing joint probability distributions of soil water retention characteristics. *Water Resources Research* **24**: 755– 769, doi: 10.1029/WR024i005p00755.

Cayan DE, Maurer EP, Dettinger MD, Tyree M, Hayhoe K. 2008. Climate change scenarios for the California region. *Climatic Change* **87**: 21-42.

Cuo L, Lettenmaier DP, Alberti M, Richey JE. 2009. Effects of a century of land cover and climate change on the hydrology of the Puget Sound basin. *Hydrological Processes* **23**(6): 907–933.

Dai, A. 2006. Precipitation characteristics in eighteen coupled climate models. *Journal of Climate* **19**: 4605-4630.

Daly C, Neilson P, Phillips DL. 1994. A statistical-topographic model for mapping climatological precipitation over mountainous terrain. *Journal of Applied Meteorology* **33**: 140-158.

Daly C, Gibson WP, Taylor GH, Johnson G L, Pasteris P. 2002. A knowledge-based approach to the statistical mapping of climate. *Climate Research* **22**: 99-113.

Daly C, Halbleib M, Smith JI, Gibson WP, Doggett MK, Taylor GH, Curtis J, Pasteris PP. 2008. Physiographically sensitive mapping of climatological temperature and precipitation across the conterminous United States. *International Journal of Climatology* **28**:2031–2064 DOI: 10.1002/joc.1688.

Delworth, T. et al. 2006. GFDL’s CM2 global coupled climate models – Part 1: Formulation and simulation characteristics. *Journal of Climate* **19**: 643–674.

Ellis CR, Pomeroy JW, Essery RLH, Link TE. 2011. Effects of needleleaf forest cover on radiation and snowmelt dynamics in the Canadian Rocky Mountains. *Canadian Journal of Forest Research* **41**: 608-620.

Epke G, Finger M, Lusardi R, Marks N, Mount J, Nichols A, Null S, O'Rear T, Purdy S, Senter, A, Viers J. 2010. Confluence: A natural and Human History of the Tuolumne River Watershed. Department of Geology and Center for Watershed Sciences, University of California Davis Mount J, Purdy S (Eds); 189.

<http://watershed.ucdavis.edu/tuolumne/resources/ConfluenceTuolumneV1.pdf> , last accessed August 6, 2012.

Graham RT, McCaffrey S, Jain TB. 2004. Science basis for changing forest structure to modify wildfire behavior and severity, General Technical Report RMRS-GTR-120. U.S. Department of Agriculture, Forest Service, Rocky Mountain Research Station: Fort Collins; 43.

Grant GE, Lewis SL, Swanson FJ, Cissel JH, McDonnell. 2008. Effects of forest practices on peak flows and consequent channel response: A state-of-science report for western Oregon and Washington, General Technical Report PNW-GTR-760, Pacific Northwest Research Station United States Department of Agriculture, Portland, Oregon.

Hamlet AF, Lettenmaier DP. 1999. Effects of Climate Change on Hydrology and Water Resources in the Columbia River Basin. American Water Resources Association **35**(6): 1597-1623.

Hardy JP, Davis RE, Jordan R, Li X, Woodcock C, Ni W, McKenzie JC. 1997. Snow ablation modeling at the stand scale in a boreal jack pine forest. *Journal of Geophysical Research* **102** (D24): 29,397-29,405.

Hardy JP, Melloh R, Koenig G, Marks D, Winstral A, Pomeroy J, Link T. 2004. Solar radiation transmission through conifer canopies. *Agriculture and Forest Meteorology* **126**: 257-270.

Helsel DR, Hirsch RM. 2002. Statistical methods in water resources: U.S. Geological Survey Techniques of Water-Resources Investigations, book 4, chap. A3; 524.

Hewlett JD. 1971. Comments on the catchment experiment to determine vegetal effects on water yield. *Water Resources Bulletin* **7** (2): 376–381.

Hewlett JD. 1982. Principles of Forest Hydrology. The University of Georgia Press, Athens; 183.

Hidalgo H, Dettinger M, Cayan D. 2008. Downscaling with constructed analogues—Daily precipitation and temperature fields over the United States: California Energy Commission PIER Final Project Report CEC-500-2007-123; 48.

Huber NK. 1987. The Geologic Story of Yosemite National Park. United States Geological Survey Bulletin, 1595; 64.

Idso SB. 1981. A set of equations for full spectrum and 8- to 14- μm and 10.5- to 12.5- μm thermal radiation from cloudless skies. *Water Resources Research* **17**: 295-304.

IPCC, Intergovernmental Panel on Climate Change. 2001. Special Report on Emissions Scenarios, Chapter 4: An Overview of Scenarios / 4.2. SRES Scenario Taxonomy / Table 4-2: Overview of SRES scenario quantifications. (Available at: http://www.grida.no/publications/other/ipcc_sr/?src=/climate/ipcc/emission/091.htm#4.2.1.)

James LD, Burges SJ. 1982. Selection, calibration, and testing of hydrologic models. Pages 437-472 in C. T. Haan, H.P. Johnson, D.L. Brakensiek, editor. *Hydrologic Modeling of Small Watersheds*. American Society of Agricultural Engineers.

Jones JA, Post DA. 2004. Seasonal and successional streamflow response to forest cutting and regrowth in the northwest and eastern United States. *Water Resources Research* **40**, doi:10.1029/2003WR002952.

Jost GR, Moore D, Weiler M, Gluns DR, Alila Y. 2009. Use of distributed snow measurements to test and improve a snowmelt model for predicting the effect of forest clear-cutting. *Journal of Hydrology*, **376**: 94-106.

Kendall MG. 1975. Rank Correlation Methods. Griffin: London; 196.

Kerkez B, Glaser SD, Bales RC, Meadows MW. 2012. Design and performance of a wireless sensor network for catchment-scale snow and soil moisture measurements, *Water Resources Research* **48**, W09515, doi:10.1029/2011WR011214.

Kittredge J. 1953. Influence of forests on snow in the ponderosa-sugar pine-fir zone of the central Sierra Nevada. *Hilgardia* **22**: 1– 96.

Knutson TR, Delworth TL, Dixon KW, Held IM, Lu J, Ramaswamy V, Schwarzkopf MD, Stenchikov G, Stouffer RJ. 2006. Assessment of twentieth century regional surface temperature trends using the GFDL CM2 Coupled Models. *Journal of Climate* **10**: 1624–1651.

Kuraś P K, Alila Y, Weiler M. 2012. Forest harvesting effects on the magnitude and frequency of peak flows can increase with return period. *Water Resources Research* **48** doi: 10.1029/2011WR010705.

Laramie RL, Schaake JCJ. 1972. Simulation of the continuous snowmelt process, report, Massachusetts Institute of Technology, Cambridge, 167.

Lettenmaier DP, Wood EF, Wallis JR. 1994. Hydro-climatological trends in the continental United States, 1948–88. *Journal of Climate* **7**:586–607.

Leung LR, Wigmosta MS. 1999. Potential climate change impacts on mountain watersheds in the Pacific Northwest. *Journal of American Water Resources Association* **35**: 1463-1471.

Leung LR, Qian Y, Bian X, Washington WM, Han J, Roads JO. 2004. Mid-Century Ensemble Regional Climate Change Scenarios for the Western United States. *Climatic Change* **62**(1-3):75-113.

Link T, Marks D, Hardy J. 2004. A deterministic method to characterize sub-canopy radiation environments. *Hydrological Processes* **18**(18): 3583-3594.

Link T, Marks D. 1999a. Distributed simulation of snowcover mass and energy balance in a boreal forest. *Hydrological Processes* **13**: 2439-2452.

Link T, Marks D. 1999b. Point simulation of seasonal snowcover dynamics beneath boreal forest canopies. *Journal of Geophysical Research* **104**: 27 841–27 858.

Loheide S PII, Lundquist JD. 2009. Snowmelt-induced diel fluxes through the hyporheic zone. *Water Resources Research* **45** doi:10.1029/2008WR007329.

Loheide S PII, Deitchman RS, Cooper DJ, Wolf EC, Hammersmark CT, Lundquist JD. 2009. Hydroecology of impacted wet meadows in the Sierra Nevada and Cascade Ranges, CA. *Hydrogeology Journal* **17**: 229–246, doi: 10.1007/s10040-008-0380-4.

Lopez-Moreno JI, Latron J. 2008. Influence of forest canopy on snow distribution in a temperate mountain range. *Hydrological Processes* **22**(1): 117–126.

Lowry C, Deems J, Loheide S PII, Lundquist JD. 2010. Linking snowmelt derived recharge and groundwater flow in a high elevation meadow system, Sierra Nevada Mountains, California. *Hydrological Processes* **24**: 2821-2833.

Lowry C, Loheide S PII, Moore C, Lundquist JD, 2011. Groundwater controls on vegetation composition and patterning in mountain meadows, *Water Resources Research* **47** W00J11, doi:10.1029/2010WR010086.

Lundquist JD, Cayan DR, Dettinger MD. 2003. Meteorology and hydrology in Yosemite National Park: A sensor network application. In Information Processing in Sensor Networks, F. Zhao and L. Guibas (eds.): IPSN 2003, LNCS 2634, 518-528.

Lundquist JD, Cayan D, Dettinger M. 2004. Spring onset in the Sierra Nevada: When is snowmelt independent of elevation? *Journal of Hydrometeorology* **5**: 325-340.

Lundquist J D, Cayan DR. 2007. Surface temperature patterns in complex terrain: daily variations and long-term change in the central Sierra Nevada, California. *Journal of Geophysical Research* **112**, D11124, doi:10.1029/2006JD007561.

Lundquist JD, Lott F. 2008. Using inexpensive temperature sensors to monitor the duration and heterogeneity of snow-covered areas in complex terrain. *Water Resources Research*, special issue on Measurement Methods **44**, W00D16, doi:10.1029/2008WR007035.

Lundquist JD, Neiman PJ, Martner B, White AB, Gattas DJ, Ralph F. M. 2008. Rain versus Snow in the Sierra Nevada, California: Comparing radar and surface observations of melting level. *Journal of Hydrometeorology* **9**: 194-211.

Lundquist JD, Loheide SP. 2011. How evaporative water losses vary between wet and dry water years as a function of elevation in the Sierra Nevada, California and critical factors for modeling. *Water Resources Research* **47**, W00H09, doi:10.1029/2010WR010050.

Mann HB, Whitney DR. 1947. On a test of whether one of two random variables is stochastically larger than the other. *Annals of Mathematical Statistics* **18**(1): 50–60.

Mann HB. 1945. Non-parametric tests against trend. *Econometrica* v. 13, p. 245–259.
Maraun D, Wetterhall F, Ireson AM, Chandler RE, Kendon EJ, Widmann M, Brienen S, Rust HW, Sauter T, Thermeßl M, Venema VKC, Chun KP, Goodess CM, Jones RG, Onof C, Vrac M, Thiele-Eich I. 2010. Precipitation downscaling under climate change: Recent developments to bridge the gap between dynamical models and the end user. *Reviews of Geophysics* **48**, RG3003, doi:8755-1209/10/2009RG000314.

Maurer EP. 2007. Uncertainty in hydrologic impacts of climate change in the Sierra Nevada, California, under two emission scenarios. *Climatic Change* **82**:309–325.

Meehl G A, Washington WM, Wigley TML, Arblaster JM, Dai A. 2003. Solar and greenhouse gas forcing and climate response in the twentieth century. *Journal of Climate* **16**: 426–444.

Minder JR, Mote PW, Lundquist JD. 2010. Surface temperature lapse rates over complex terrain: Lessons from the Cascade Mountains, *Journal of Geophysical Research* **115**: D14122, doi:10.1029/2009JD013493.

Moriasi DN, Arnold JG, Van Liew M W, Bingner RL, Harmel RD, Veith TL. 2007. Model Evaluation Guidelines for Systematic Quantification of Accuracy in Watershed Simulations. *Transactions of the ASABE* **50** (3), 885–900.

Murray CD, Buttle JM. 2003. Impacts of clearcut harvesting on snow accumulation and melt in a northern hardwood forest. *Journal of Hydrology* **271**:197-212.

Nash JE, Sutcliffe JV. 1970. River flow forecasting through conceptual models part I – A discussion of principles. *Journal of Hydrology* **10** (3): 282–290.

Null SE, Viers JH, Mount JF. 2010. Hydrologic Response and Watershed Sensitivity to Climate Warming in California's Sierra Nevada. *PLoS ONE*, **5**, e9932.
doi:10.1371/journal.pone.0009932

Pomeroy JW, Marks D, Link T, Ellis C, Hardy J, Rowlands A, Granger R. 2009. The impact of coniferous forest temperature on incoming longwave radiation to melting snow. *Hydrological Processes* **23**: 2513–2525 doi:10.1002/hyp. 7325.

Rantz SE et al. 1982. Measurement and computation of streamflow: Volume 1. Measurement of stage and discharge, U.S. Geological Survey Water-Supply Paper 2175, U.S. Dept. of the Interior, Washington, D. C.; 284.

Regonda S, Rajagopalan B, Clark M, Pitlick J. 2005. Seasonal cycle shifts in hydroclimatology over the Western US. *Journal of Climate* **18**: 372-384.

Rice R, Bales RC, Painter TH, Dozier J. 2011. Snow water equivalent along elevation gradients in the Merced and Tuolumne River basins of the Sierra Nevada. *Water Resources Research* **47**, W08515, doi:10.1029/2010WR009278.

Robinson M, Cognard-Plancq AL, Cosandey, C David J, Durand P, Fuhrer HW, Hall R, Hendriques MO, Marc V, McCarthy R, McDonnell M, Martin C, Nisbet T, O'Dea PO, Rodgers M, Zollner A. 2003. Studies of the impact of forests on peak flows and baseflows: a European perspective. *Forest Ecology and Management* **186**: 85-97.

Running S, Nemani R, Hungerford R. 1987. Extrapolation of synoptic meteorological data in mountainous terrain and its use for simulating forest evapotranspiration and photosynthesis. *Canadian Journal of Forest Research* **17**: 472-483.

Safeeq M, Fares A. 2011. Hydrologic response of a Hawaiian watershed to future climate change scenarios. *Hydrological Process* doi: 10.1002/hyp.8328.

Schnorbus MA, Alila Y. 2004a. Forest harvesting impacts on the peak flow regime in the Columbia Mountains of southeastern British Columbia: An investigation using long-term numerical modeling. *Water Resources Research* **40**, doi:10.1029/2003WR002918.

Schnorbus MA, Alila Y. 2004b. Generation of an Hourly Meteorological Time Series for an Alpine basin in British Columbia for use in numerical hydrologic modeling. *Journal of Hydrometeorology* **5**:862–888.

Sen PK. 1968. Estimates of the regression coefficient based on Kendall's tau. *Journal of the American Statistical Association*. **63**:1379-1389.

Sicart JE, Pomeroy JW, Essery RLH, Hardy J, Link T, Marks D. 2004. A sensitivity study of daytime net radiation during snowmelt to forest canopy and atmospheric conditions. *Journal of Hydrometeorology* **5**: 774–784.

Stewart I, Cayan DR, Dettinger MD. 2005. Changes towards earlier streamflow timing across western North America. *Journal of Climate* **18**: 1136–1155.

Strasser U, Warscher M, Liston GE. 2011: Modeling Snow–Canopy Processes on an Idealized Mountain. *Journal of Hydrometeorology* **12**: 663–677, doi: 10.1175/2011JHM1344.1.

Shuttleworth J. 1992. Evaporation. Chapter 4 of the Handbook of Hydrology, D. Maidment, Ed., McGraw-Hill, Inc., New York.

Storck P, 2000. Trees, snow and flooding. An investigation of forest canopy effects on snow accumulation and melt at the plot and watershed scales in the Pacific Northwest. In: Water Resources Series, Technical Report 161. University of Washington, Seattle, WA; 176 .

Storck P, Lettenmaier DP, Bolton SM. 2002. Measurement of snow interception and canopy effects on snow accumulation and melt in a mountainous maritime climate, Oregon, United States. *Water Resources Research* **38**: 1-16.

Stouffer et al. 2006. GFDL's CM2 global coupled climate models – Part 4: Idealized climate response. *Journal of Climate* **19**: 723–740.

Tague C, Seaby A, Hope A. 2008. Modeling the eco-hydrologic response of a Mediterranean type ecosystem to the combined impacts of projected climate change and altered fire frequencies. *Climatic Change* **93**:137-155 DOI: 10.1007/s10584-008-9497-7.

U.S. Department of Agriculture, Natural Resources Conservation Service. 2006. Soil Survey Geographic (SSURGO) database for Yosemite National Park, California, ca790. Available at: <http://SoilDataMart.nrcs.usda.gov/>

Teng J, Vaze J, Chiew FHS, Wang B, Jean-Michel Perraud J-M. 2012. Estimating the relative uncertainties sourced from GCMs and hydrological models in modelling climate change impact on runoff. *Journal of Hydrometeorology* **13**: 122–139 doi: 10.1175/JHM-D-11-058.1.

Theil H. 1950a. A rank-invariant method of linear and polynomial regression analysis, I. *Nederlands Akad. Wetensch. Proc.* 53:386–392.

Theil H. 1950b. A rank-invariant method of linear and polynomial regression analysis, II. *Nederlands Akad. Wetensch. Proc.* 53: 521–525.

Theil H. 1950c. A rank-invariant method of linear and polynomial regression analysis, III. *Nederlands Akad. Wetensch. Proc.* 53: 1397–1412.

Thyer M, Beckers J, Spittlehouse D, Alila Y, Winkler R. 2004. Diagnosing a distributed hydrologic model for two high-elevation forested catchments based on detailed stand- and basin-scale data. *Water Resources Research* **40**, 1. doi:10.1029/2003WR002414.

Veatch W, Brooks PD, Gustafson JR, Molotch NP. 2009. Quantifying the effects of forest canopy cover on net snow accumulation at a continental, mid-latitude site. *Ecohydrology* **2**: 115-128.

Waichler SR, Wigmosta MS. 2003. Development of hourly meteorological values from daily data and significance to hydrological modeling at H. J. Andrews Experimental Forest. *Journal of Hydrometeorology* **4**: 251-263.

Washington WM, Weatherly J W, Meehl G A, Semtner AJ, Bettge T W, Craig A P, Strand W.G, Arblaster J, Wayland VB, James R, Zhang Y. 2000. Parallel climate model (PCM) control and transient simulations. *Climate Dynamics* **16**: 755–774.

Whitaker A, Alila Y, Beckers J. 2002. Evaluating peak flow sensitivity to clear-cutting in different elevation bands of a snowmelt dominated mountainous catchment. *Water Resources Research* **38**(9): 1172, doi:10.1029/2001WR000514.

Wigley, TML. 2009. The effect of changing climate on the frequency of absolute extreme events. *Climatic Change* **97**:67–76, DOI 10.1007/s10584-009-9654-7.

Wigmosta MS, Nijssen B, Storck P, Lettenmaier, DP. 2002. The distributed hydrology soil vegetation model. In: Singh, V.P., Frevert, D.K. (Eds.), *Mathematical Models of Small Watershed Hydrology and Applications*, Water Resource Publications, Littleton, CO; 7–42.

Wigmosta MS, Vail LW, Lettenmaier DP. 1994. A distributed hydrology-vegetation model for complex terrain. *Water Resources Research* **30**: 1665-1679.

Wilcoxon F. (1945). Individual comparisons by ranking methods. *Biometrics Bulletin* **1**(6): 80–83.

Wiley MW, Palmer RN. 2008. Estimating the impacts and uncertainty of climate change on a municipal water supply system. *Journal of Water Resources Planning and Management* **134**: 239-246, DOI: 10.1061/(ASCE)0733-9496(2008)134:3(239).

Winkler RD. 2011. Changes in snow accumulation and ablation after a fire in south-central British Columbia. *Streamline Watershed Management Bulletin* **14**: 1–7.

Winkler RD, Spittlehouse DL, Golding DL. 2005. Measured differences in snow accumulation and melt among clearcut, juvenile, and mature forests in Southern British Columbia. *Hydrological Processes* **9**:51-62.

Yue S, Hashino M. 2003. Temperature trends in Japan: 1900–1996. *Theoretical and Applied Climatology* **75**:15–27.

Yue S, Pilon P, Phinney B, Cavadias G. 2002. The influence of autocorrelation on the ability to detect trend in hydrological series. *Hydrological Processes* **16**(9): 1807–1829, DOI: 10.1002/hyp.1095.

Zhao Q, Liu Z, Ye B, Qin Y, Wei Z, Fang S. 2009. A snowmelt runoff forecasting model coupling WRF and DHSVM. *Hydrology and Earth System Sciences* **13**: 1897–1906.

Appendix 5A

5A-1. Description of snowpack energy balance

The snow pack energy balance equation and its components are described below following Wigmosta *et al.*, 1994. The snowpack energy balance equation implemented in DHSVM is based on the formulation:

$$c_s SWE \frac{dT_s}{dt} = R_{ns} + Q_s + Q_l + Q_p + Q_m \quad (A1)$$

where c_s is the ice specific heat, SWE is the snowpack water equivalent, T_s is the temperature of the snow surface, t is time, R_{ns} is the net radiation, Q_s is the sensible heat, Q_l is the gained latent heat from condensation or lost to sublimation, Q_p is the advected heat to the snowpack from rainfall, and Q_m is the internal latent heat gained from refreezing of liquid water for T_s below 0°C or lost by melting for T_s above 0°C. Equation A1 is solved through a finite difference scheme. If T_s is equal to 0°C during the computational timestep, Q_m is the melt energy calculated as:

$$Q_m = R_{ns} + Q_s + Q_l + Q_p + c_s SWE \cdot T_s' \quad (A2)$$

where T_s^t is the snowpack temperature during the timestep t .

Net radiation R_{ns} is composed of the net shortwave radiation R_{ss} and the net longwave radiation R_{ls} :

$$R_{ns} = R_{ss} + R_{ls} . \quad (A3)$$

The amount of shortwave radiation R_{ss} at the snow surface is estimated based on the total amount of incident solar radiation R_s and the filtering effects from the canopy as:

$$R_{ss} = R_s (1 - \alpha_s) (\tau_o F + (1 - F)), \quad (A4)$$

where α_s is the snow reflection coefficient (albedo), F is the forest fractional cover, and τ_o is the fraction of R_s transmitted by the overstory canopy, calculated based on a form of Beer's law as:

$$\tau_o = \exp(-kLAI_o), \quad (A5)$$

where k is canopy attenuation coefficient and LAI_o is the overstory leaf area index. In the absence of site specific albedo data, the curves modeling albedo in the Tuolumne area were parameterized identically for both barren and forested areas. Separate decay functions were used for below and above freezing conditions, driven by the simulated surface temperature T_{ss} , with albedo decreasing more rapidly during melting, based on the equations proposed by Laramie and Schaake (1972):

$$\text{Forest Subfreezing:} \quad \alpha_s = \alpha_0 * 0.92^{(d/s)^{0.58}}, \quad \text{minimum } 0.7, T_{ss} < 0^\circ\text{C} \quad (A6)$$

$$\text{Forest Melting:} \quad \alpha_s = \alpha_0 * 0.87^{(d/s)^{0.46}}, \quad \text{minimum } 0.5, T_{ss} > 0^\circ\text{C} \quad (A7)$$

where α_0 is set to 0.85, the albedo of fresh snow, d is the number of days since the last snowfall and, s is the number of time steps per day.

The net longwave radiation R_{ls} is estimated as:

$$R_{ls} = L_o F + (L_d (1 - F)) - L_s \quad (A8)$$

in which L_d is incoming longwave radiation, L_o is the upward overstory longwave radiation flux, and L_s is the upward longwave radiation from the snow surface. Both L_o and L_s are given by similar expressions of the form:

$$L_o = \sigma(T_o + 273)^4 \quad \text{and} \quad L_s = \sigma(T_s + 273)^4 \quad (A9)$$

in which T_o is the overstory temperature and σ is the Stefan-Boltzman constant.

The sensible heat flux Q_s is estimated as:

$$Q_s = \frac{\rho c_p (T_a - T_s)}{r_{as}} \quad (\text{A10})$$

where ρ is the density of air, c_p is the specific heat of air, T_a is the air temperature and r_{as} is the surface resistance corrected for atmospheric stability and vegetation effects. The latent heat term Q_e in the energy balance equation is given by:

$$Q_e = \frac{\lambda_i \rho \left(\frac{0.622}{P_a} \right) (e(T_a) - e_s(T_s))}{r_{as}}, \quad (\text{A11})$$

in which λ_i either represents the latent heat of vaporization during melting conditions, or the latent heat of fusion during freezing conditions, P_a is the atmospheric pressure, and e and e_s are the vapor pressures at T_a and T_s , respectively. Finally, the internal latent heat gained from melting or refreezing for snow surface temperatures different than 0°C is calculated as:

$$Q_m = \lambda_i \rho_w M, \quad (\text{A12})$$

where M is the depth of snowmelt (negative flux), or the volume of refrozen liquid water (positive flux).

DHSVM code, additional documentation and pre-and post processing tools are available to download at:

<http://www.hydro.washington.edu/Lettenmaier/Models/DHSVM/index.shtml>

5A-2. DHSVM model setup and sensitivity tests

Radiation attenuation by the canopy was sensitive to representing the timing of streamflow. Parameterizations of the albedo curves, also part of the shortwave radiation model (Eq. A6, A7) were found in other studies to influence the modeled SWE under the forest (Thyer, *et al.*, 2004, Jost *et al.*, 2009, Bewley *et al.*, 2010). However, albedo observations under the forest canopy were not available in the Tuolumne basin, therefore model default albedo functions were used in model simulations (Eq. A6, A7). The remaining final DHSVM calibration parameters are listed in Table 1.A1.

Table 5.A1. DHSVM parameters used for the upper Tuolumne area, Sierra Nevada.

Forest parameters	Value	References
Overstory vegetation height (m)	13.6	R1
Understory vegetation height (m)	0.5	R1
Overstory fractional coverage (%)	80	R1
Understory fractional coverage (%)	80	R1
Overstory leaf area index, LAI (-)	5.0	R1
Understory leaf area index, LAI (-)	3.0	R1
Radiation attenuation	0.3	R2
Maximum snow interception capacity (m SWE)	0.02	R2
Snow interception efficiency (-)	0.6	R3
Mass release drip ratio	0.4	R3
Minimum melt needed for mass release (m SWE)	0.002	R3
Snow mass release/drip ratio (-)	0.4	R3
LAI multiplier for rain (m)	0.0001	R4
LAI multiplier for snow (m)	0.005	R5
Aerodynamic attenuation coefficient	2.0	R4
Maximum stomatal resistance (sm^{-1}) overstory	5000	R6
Maximum stomatal resistance (sm^{-1}) understory	3000	R6
Minimum stomatal resistance (sm^{-1}) overstory	650	R6
Minimum stomatal resistance (sm^{-1}) understory	200	R6
Vapor pressure deficit causing stomatal closure overstory	4000	R2
Vapor pressure deficit causing stomatal closure understory	4000	R2
Moisture threshold below which transpiration is restricted	0.33	R4
Moisture threshold below which transpiration is restricted	0.13	R4
Albedo	0.2	R6
Overstory root fractions in soil layers 1,2,and 3	0.2; 0.4;	R6
Understory root fractions in soil layers 1,2,and 3	0.4; 0.6;	R6
Soil parameters		
<i>Sand</i> Lateral saturated hydraulic conductivity K_{lat} ($\text{m}\cdot\text{s}^{-1}$), porosity	8.2e-5; 0.43	R7
<i>Loamy Sand</i> Lateral saturated hydraulic conductivity K_{lat} ($\text{m}\cdot\text{s}^{-1}$), porosity	4.05e-5; 0.42	R7
<i>Sandy Loam,</i> Lateral saturated hydraulic conductivity K_{lat} ($\text{m}\cdot\text{s}^{-1}$), porosity	1.3e-5; 0.4	R7
<i>Bedrock</i> Lateral saturated hydraulic conductivity K_{lat} ($\text{m}\cdot\text{s}^{-1}$), porosity	1.0e-8; 0.4	R7
Other parameters		
Snow roughness (m)	0.01	R8
Minimum air temperature for snow ($^{\circ}\text{C}$)	3.0	R9
Minimum air temperature for rain($^{\circ}\text{C}$)	0.0	R9

References listed are: R1: NPS vegetation survey data; R2: Thyer *et al.*, 2004; R3: Storck, 2000; R4: Waichler *et al.*, 2003, R5: Bewley *et al.*, 2010, R6: Zhao *et al.*, 2009, R7: Ranges provided in Carsel and Parrish, 1988, based on USDA soil classifications (USDA NRCS 2006), R8: Andreadis *et al.* 2009; R9: Lundquist *et al.*, 2008.

Daily climate data were disaggregated into 3-hourly values using the existing pre-processing tools accompanying DHSVM, in which few adjustments were made specific to this project. Within these algorithms the following assumptions were included. Precipitation was distributed uniformly throughout the day. Diurnal temperature variations were established based on the daily extremes from the climate data and the site location for estimating the approximate times of the day when these extremes are likely to occur. The daily minimum and maximum temperatures were then interpolated for 3-hourly variations using hermite polynomials. The minimum relative humidity was assumed to occur at the minimum air temperature, which was taken equal to the dew point temperature. Diurnal relative humidity fluctuations were then established based on the ratios of vapor pressures at a given temperature during the day and the vapor pressure at the minimum temperature based on a model by Running *et al.* (1987). The 3-hourly solar radiation series was generated using an algorithm proposed by Bristow and Campbell (1984) that was calibrated to best match the hourly rates recorded at Dana Meadows during the 2003-2009 period. Incoming longwave radiation was generated using the Idso (1981) method. For each day of the year, the 3-hourly wind speed values were assumed to be equal to the daily average wind speed recorded at Dana Meadows during the 2003-2009 period.

We assessed the uncertainty of the most sensitive forest parameters and their effects on model response when temperature increases. These additional tests were considered because direct measurements of snow under the forest were not available for the 2003-2009 calibration period, and therefore direct comparisons of the simulated and observed SWE under the forest were not possible. However, the forest effects at the basin scale were explicitly taken into account through distributed modeling and canopy parameterization, as described in Section 3.1, and through model calibration on the streamflow data as the model integrated response. Alila and Beckers (2001) identified the most sensitive forest parameters for snow accumulation and melt in DHSVM as the fractional cover, leaf area index, LAI, radiation attenuation k , and wind (aerodynamic) attenuation a .

During preliminary runs, we tested k , LAI and a for the historic 2003-2009 meteorology. The base parameters were $k = 0.3$, LAI = 5.0, and $a = 2.0$, respectively established during calibration (Appendix 5A, Table 1.A1). These values were varied sequentially from $k = 0.1$ to $k = 0.5$ (for k), LAI = 3.0 to LAI = 7.0 (for LAI), and $a = 1.0$ to $a = 3.0$ (for a), while maintaining all the remaining parameters constant. These tested parameters influenced the simulated SWE more significantly during the melt season than during the accumulation season, with patterns of SWE sensitivity similar to those shown in Figure 4 in Alila and Beckers, 2001. Fractional cover was not part of these preliminary tests, as its

sensitivity was previously considered within the vegetation scenarios in the climate change model runs (Table 5.2). Because SWE during the melt period was most sensitive to the radiation attenuation k , we chose this parameter to further illustrate the uncertainty in forest parameterization in the historic T and historic T + 3°C temperature scenarios. The calibration k was set to 0.3, corresponding to a value of τ_o , the fraction of incoming solar radiation R_s transmitted by the canopy (Eq. A5, Appendix 5A), of 0.22. The k value was subsequently ranged from 0.1 ($\tau_o = 0.60$) to 0.5 ($\tau_o = 0.08$), the same levels of sensitivity used in Alila and Beckers, 2001 (scenarios 1-4, Table 1.A2).

Table 5.A2. DHSVM scenarios for radiation attenuation sensitivity tests.

Scenario	Vegetation cover	Scenario assumptions
1	Distributed forest	$k = 0.1$ ($\tau_o = 0.60$), historic T
2	Distributed forest	$k = 0.5$ ($\tau_o = 0.08$), historic T
3	Distributed forest	$k = 0.1$ ($\tau_o = 0.60$), historic T+ 3°C
4	Distributed forest	$k = 0.5$ ($\tau_o = 0.08$), historic T+ 3°C

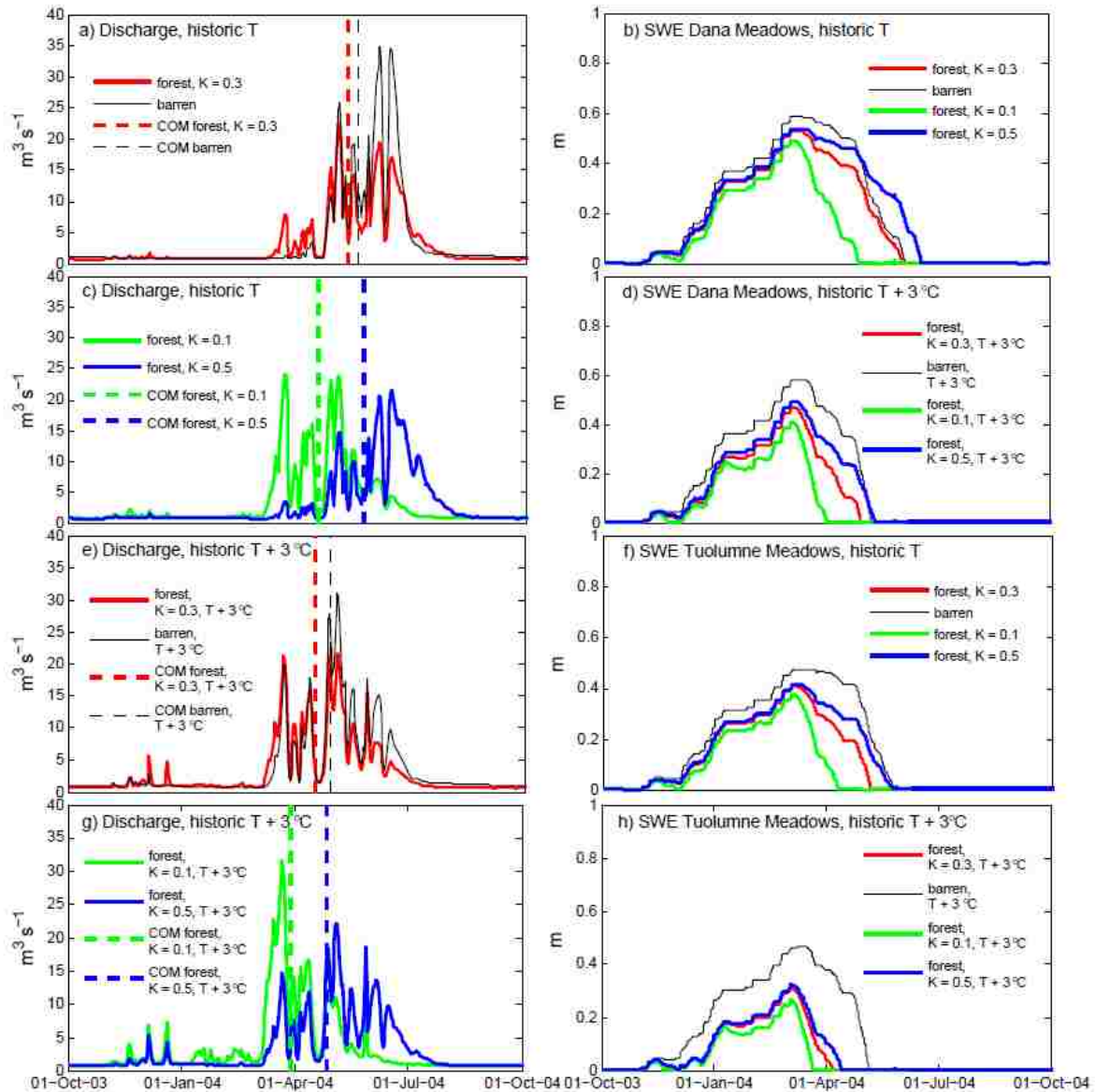


Figure 5.A1. a), c), e), g) Simulated daily hydrographs assuming historic and increased air temperatures for barren scenario and for uniform forest scenario with variable radiation attenuation parameter k ; b), d), f), h) SWE levels for the same scenarios at Dana Meadows and Tuolumne Meadows locations. Vertical lines identify COM for each hydrograph. All plots are shown for water year 2004.

The results from this sensitivity analysis are illustrated in Figure 5.A1b, d, f, h that show the simulated SWE at Dana Meadows (Figure 5.A1b, d) and Tuolumne Meadows (Figure 5.A1f, h) as a result of varying k , the radiation attenuation coefficient, corresponding to fractions transmitted of 0.60 ($k = 0.1$), 0.22 ($k = 0.3$, calibration value) and 0.08 ($k = 0.5$) for the two temperature scenarios. Examination of Figure 5.A1b, d, f, h leads to two observations: i) the snowpack under the forest melted earlier in the increased temperature scenario than the snowpack on bare ground even considering the relatively

large uncertainty in shortwave radiation parameterization (Figure 5.A1d, h), and ii) the sensitivity of simulated SWE to k during the melting season decreases when temperature increases (Figure 5.A1b, d, f, h). This effect is more apparent at the lower elevation snow pillow site, Tuolumne Meadows than at the higher elevation site, Dana Meadows (Figure 5.A1d, h). The variations in k were also reflected in the simulated hydrograph (Figure 5.A1a, c, e, g). Assuming $k = 0.3$ (calibration value), in the historic T scenario, the forest COM occurred 9 days earlier than the barren COM (Figure 5.A1a). This difference increased to 26 days for $k = 0.1$, while for $k = 0.5$, the forest COM occurred 12 days later than the barren COM (Figure 5.A1a, c). In the increased temperature scenario forest COM occurred earlier than barren COM by 32 days ($k = 0.1$), 14 days ($k = 0.3$) and 3 days ($k = 0.5$), respectively. Figure 5.A2 shows a snow covered landscape in the spring of 2011 in the Sierra Nevada near the Tuolumne area (Lat: $38^{\circ}48'56''$, Long: $120^{\circ}06'35''$). The snow under the forest has largely disappeared while snow remains in the barren areas.



Figure 5.A2. Google Earth 6.2.image (June 14, 2011) approximately 124.2 km from the Tuolumne Meadows in the Sierra Nevada centered at $38^{\circ}48'56''$ N Lat and $120^{\circ}06'35''$ W Long and 2158 m elevation, showing snow lasting longer in the barren areas than under the forest. Available through: <http://www.google.com/earth/index.html> [Accessed June 2012].

CURRICULUM VITAE

EDUCATION:

PhD, Civil and Environmental Engineering *Water Resources, Hydrology and Environmental Fluid Mechanics*, University of Washington, Seattle WA – final exam passed Autumn quarter 2012. Dissertation title: *Evaluating reference evapotranspiration and the effects of climate change and soil parameterization within distributed hydrologic models*. Advisor: Dr. Stephen J. Burges.

M.S.E, Civil and Environmental Engineering, University of Washington, Seattle WA, 2004.

M.S., Hydropower and Environmental Engineering, University POLITEHNICA of Bucharest, Romania, 1997.

B.S., Hydropower and Environmental Engineering, University POLITEHNICA of Bucharest, Romania, 1996.

PROFESSIONAL EXPERIENCE:

2006 - present Doctoral Candidate, Department of Civil and Environmental Engineering, University of Washington, Seattle.

2004 - 2006 Environmental Engineer, Washington State Department of Ecology.

2002 - 2004 Research assistant, Department of Civil and Environmental Engineering, University of Washington, Seattle.

1997 - 2000 Research /teaching assistant, University POLITEHNICA of Bucharest, Romania.

PUBLICATIONS:

Scientific journals:

Cristea, N.C., Kampf, S.K., Burges S.J., (2012). Linear models for estimating annual and growing season reference evapotranspiration using averages of weather variables, International Journal of Climatology, DOI: 10.1002/joc.3430

Cristea, N.C., Kampf, S.K., Burges S.J., (2012). Revised coefficients for Priestley-Taylor and Makkink-Hansen equations for estimating daily reference evapotranspiration, Journal of Hydrologic Engineering (ASCE). doi:10.1061/(ASCE)HE.1943-5584.0000679.

Mirus, B.B., Loague, K., Cristea, N.C., Burges S.J., and Kampf S.K. (2011). A synthetic hydrologic-response dataset. *Hydrological Processes*, DOI:10.1002/hyp.8185

Cristea, N. C. and S. J. Burges (2010). An assessment of the current and future thermal regimes of three streams located in the Wenatchee River basin, Washington State: some implications for regional river basin systems, *Climatic Change*, 102(3), 493-520, DOI:10.1007/s10584-009-9700-5

Cristea, N. C. and S. J. Burges (2009). Use of Thermal Infrared Imagery to Complement Monitoring and Modeling of Spatial Stream Temperatures, *Journal of Hydrologic Engineering (ASCE)*, 14(10), 1080-1090, DOI: 10.1061/(ASCE)HE.1943-5584.0000072.

In review:

Cristea, N.C., Lundquist, J.D., Loheide II, S.P., Lowry C.S., Moore C. E. submitted to *Hydrological Processes*. Modeling how vegetation cover affects climate change impacts on streamflow timing and magnitude in the upper Tuolumne Basin, Sierra Nevada

Feld, S., Cristea N.C., Lundquist, J.D., submitted to *Water Resources Research*. Representing atmospheric moisture content along mountain slopes: Examination using distributed sensors in the Sierra Nevada, California

Washington State Department of Ecology publications:

Hood S., Cristea, N.C., Stohr A (2011). Whatcom, Squalicum, and Padden Creeks Temperature Total Maximum Daily Load: Water Quality Improvement Report, Washington State Department of Ecology, Olympia, Washington, Publication Number 07-03-028 <https://fortress.wa.gov/ecy/publications/publications/1110019.pdf>.

Cristea, N.C., and Janisch, J. (2007). Modeling the effects of riparian buffer width on effective shade and stream temperature, Washington State Department of Ecology, Olympia, Washington, Publication Number 07-03-028 <https://fortress.wa.gov/ecy/publications/publications/0703028.pdf> .

Kardouni, J., and Cristea, N.C. (2006). Quality Assurance Project Plan for Snoqualmie River Temperature Total Maximum Daily Load Study. Washington State Department of Ecology, Olympia, Washington, Publication Number 06-03-106 <https://fortress.wa.gov/ecy/publications/publications/0603106.pdf> .

Cristea, N.C., and Pelletier, G. (2005). Wenatchee River Temperature Total Maximum Daily Load Study. Olympia, Washington, Publication Number 05-03-011 <https://fortress.wa.gov/ecy/publications/publications/0503011.pdf> .

SCHOLARSHIPS:

Travel support from the University of Washington Department of Civil and Environmental Engineering to present at the American Geophysical Union meeting, San Francisco, December 2011

Travel support from the University of Washington Department of Civil and Environmental Engineering to present at the American Geophysical Union meeting, San Francisco, December 2010

Egtvedt fellowship, University of Washington, Seattle (3 mo, 2009)

European Commission ERASMUS scholarship (Institut National des Sciences Appliquées de Lyon, France, 3 mo, 1999)

European Commission ERASMUS scholarship (Politecnico di Torino, Italy, 6 mo, 1998)

European Commission TEMPUS scholarship (Vrije Universiteit Brussel, Belgium, 4mo, 1997)

Governmental scholarship to support undergraduate studies (1991-1996)

CONFERENCE ABSTRACTS:

Cristea N. C., and Burges, S. J., (2004). Wenatchee River, Washington, Water Temperature Modeling and Assessment Using Remotely Sensed Thermal Infrared and Instream Recorded Data. Eos. Trans. AGU 85(47), Fall Meet. Suppl., Abstract H13C-0449.

Cristea, N.C., Kampf S.K., Mirus B.B., Loague K., Burges S.J. (2007). Developing a framework for testing distributed hydrologic models at the hillslope scale. Eos Trans. AGU, Fall Meet. Suppl., Abstract H21A-0170.

Cristea, N.C., Kampf S.K., Mirus B.B., Loague K., Burges S.J. (2008). Developing a framework for testing distributed hydrologic models at the hillslope scale – examples of test model runs for event based and long term simulations. Eos Trans. AGU, Fall Meet. Suppl., Abstract H11C-0765.

Cristea, N.C., Kampf S.K., Mirus B.B., Loague K., Burges S.J. (2009). Distributed hydrologic model testing at the catchment scale using a hypothetical reality data set. Eos Trans. AGU, Fall Meeting Supplement, Abstract H33F-0953.

Cristea, N.C., Kampf S.K., Mirus B.B., Loague K., Burges S.J. (2010). Effects of soil parameterization on distributed hydrologic response: Testing a distributed hydrologic

model using a hypothetical reality dataset. *Eos Trans. AGU*, Fall Meeting Supplement, Abstract H41F-1131.

Cristea, N.C., Kampf S.K., Burges S.J. (2011). Revised coefficients for Priestley-Taylor and Makkink-Hansen equations for estimating daily reference evapotranspiration. Eos Trans. AGU, Fall Meeting Supplement, Abstract H33A-1280.

Lowry, C.S., Loheide II, S.P., Lundquist, J.D., *Cristea, N.C., Moore, C.E. (2012). High Elevation Groundwater Dependent Ecosystems: Modeling ecohydrology to quantifying historical and restoration scenarios. International Association of Hydrologists Congress, Niagra Falls, Ontario, Canada, Abstract 573.*